Aus der Neurologischen Universitätsklinik Tübingen
Abteilung Neurologie mit interdisziplinärem Schwerpunkt
Neuroonkologie

Targeting the glioma associated microenvironment in experimental glioma

Inaugural-Dissertation
zur Erlangung des Doktorgrades
der Medizin

der Medizinischen Fakultät
der Eberhard Karls Universität
zu Tübingen

vorgelegt von

Becker, Hannes Maximilian

2022

Dekan:	Professor Dr. B. Pichler
1. Berichterstatter:	Professorin Dr. Dr. G. Tabatabai
2. Berichterstatter:	Professorin Dr. J. Skokowa, Ph.D
3. Berichterstatter:	Professorin Dr. K. Lamszus

Tag der Disputation: 01.07.2022

Dedication

I dedicate this work to my parents, Elisabeth and Siegfried Becker, and my uncle Wilhelm Glöckler, who have always been by my side, encouraged me, and who paved my academic path.

Table of contents

List of tables

List of figures

List of abbreviations

°C	Celsius
µg	Microgramm
^{18}-FDG	18F-2-fluoro-2-deoxy-D-glucose
^{18}-FET	O-(2-[18F]-fluoroethyl)-L-tyrosine
5-ALA	5-aminolevulinic acid
ADC	Apparent diffusion coefficient
ALSP	Adult-onset leukoencephalopathy with axonal spheroids and pigmented glia
ALSV	Avian leucosis and sarcoma virus
APCs	Antigen presenting cells
ATRX	Alpha Thalassemia/Mental Retardation Syndrome X-Linked
BBB	Blood-brain-barrier
bFGF	basic fibroblast growth factor
bp	Base pairs
BSA	Bovine serum albumin
bw	Bodyweight
CAR	Chimeric Antigen Receptor
CBTRUS	Central Brain Tumor Registry of the United States
CD	Cluster of differentiation
CFP	Cyan fluorescent protein
CNS	Central nervous system
CO_2	Carbon dioxide
CSF1R	Colony stimulating factor 1 receptor

CT	Computed tomography
CTLA4	Cytotoxic T-lymphocyte-associated protein 4
DAPI	4’,6-diamidino-2-phenylindole
DMEM	Dulbecco’s Modified Eagle Medium
DMSO	Dimethylsulfoxide
DNA	Deoxyribonucleic acid
DPBS	Dulbecco’s phosphate buffered saline
dpi	Days post implantation
DWI	Diffusion weighted imaging
EANO	European Association of Neuro-Oncology
E.coli	Escherichia coli
ECM	Extracellular matrix
EGFR	Epidermal growth factor receptor
FBS	Fetal bovine serum
FISH	Fluorescence in situ hybridization
FITC	Fluorescein Isothiocyanate
FLAIR	Fluid-attenuated inversion recovery
FOV	Field of view
FP	Forward primer
GAMs	Glioma-associated macrophages
GEMs	Genetically engineered models
GFAP	Glial fibrillary acidic protein
h	Hour

H&E	Haematoxylin and Eosin
H_20	Water
ICC	Immunocytochemistry
IDH R132	Isocitrate dehydrogenase R132
IgG	Immunoglobulin G
IGF1R	Insulin-like growth factor 1 receptor
IHC	Immunohistochemistry
IL	Interleukin
IP	Intraperitoneal Injection
irAEs	Immune related adverse events
kb	Kilobases
kbp	kilo base pairs
KPS	Karnofsky Performance Score
M	Molar
mBq	Megabecquerel
MCP-1	Monocyte chemoattractant protein- 1
m-CSF	macrophage-colony stimulating factor 1
mg	Milligram
MGMT	O(6)-methylguanine-DNA methyltransferase
MHC	Major histocompatibility complex
min	Minute
ml	Mililiter
mM	Milimolar

MMP-2	Matrix metalloprotease- 2
MOI	Multiplicity of infection
MRI	Magnetic Resonance Imaging
mRNA	Messenger ribonucleic acid
NaCl	Sodium chloride
NF1+2	Neurofibromatosis 1 and 2
ng	Nanogram
NK cells	Natural killer cells
nM	Nanomolar
PBS	Phosphate buffered saline
PD1	Programmed cell death 1
PDGFB	Platelet-derived growth factor B
PD-L1	Programmed cell death 1 ligand 1
PDM	Patient derived microtumour
PDOX	Patient-derived orthotopic xeno-craft
PECAM-1	Platelet endothelial cell adhesion molecule 1
PEI	Polyethylenimine
PET	Positron-emission tomography
PFA	Paraformaldehyde
PLL	Poly-L-lysine hydrobromide
Prim	Primary
PTP ζ	Protein tyrosine phosphatase ζ
qPCR	Real-time quantitative polymerase chain reaction

RCAS/TVA	Replication-competent avian sarcoma-leukosis virus long terminal repeat with splice acceptor/ tumour virus A
Recurr	Recurrent
RNA	Ribonucleic acid
ROI	Region of Interest
RP	Reverse primer
rpm	Rounds per minute
RT	Room Temperature
SC	Subcutaneous Injection
sec	Second
TAM	Tumour-associated macrophage
TCR	T cell receptor
TGF-ß	Transforming growth factor-ß
TILs	Tumour infiltrating lymphocytes
TMA	Tissue microarray
TME	Tumour microenvironment
TNF α	Tumour necrosis factor α
TU	Transduction unit
V	Volt
VEGF	Vascular endothelial growth factor
YFP	Yellow fluorescent protein
µl	Microliter
µm	Micrometer
µM	Micromolar

USA	United states of America
WHO	World Health Organization

1 Introduction

Tumours of the central nervous system (CNS) consist of various intra- or extra-axial located tumour entities with variable degrees of malignancy. The composition of the group of CNS tumours is highly heterogeneous concerning incidence, morbidity and mortality as well as biological origin and presentation.[1-4] This group encompasses slow growing extra-axial located types such as meningioma as well as highly malignant intra-axial tumours such as the glioblastoma.[1, 3]

According to the Central Brain Tumor Registry of the United States (CBTRUS) Statistical Report of 2018 CNS tumours are the most common cancer type of children (age 0-14 years) with an annual incidence rate of 5.65 per 100 000 inhabitants.[3] In general, CNS tumours show stable presence in all age groups with a high ratio of mortality versus incidence per 100 000 inhabitants.[3]

The following paragraphs describe the characteristic histological and clinical presentation of gliomas, mainly focusing on the glioblastoma subtype and its microenvironment.

1.1 Gliomas

1.1.1 Epidemiology

With 81 % of all malignant primary CNS tumours, gliomas are the most frequent primary, intra-axially located malignant CNS tumour entity.[3] The group of gliomas includes glioblastoma, anaplastic and diffuse astrocytoma, oligodendroglioma, other astrocytic tumours like the pilocytic astrocytoma and the group of ependymoma.[1, 4-6] With 56.6 % the majority of gliomas are glioblastoma with an incidence rate of 3.21 per 100 000 population.[3] In the group of CNS tumours glioblastoma is the third most frequent subtype and counts for 14.7 % of all tumours. 61.2 % of glioma have a supra-tentorial location and are found nearly equally in the frontal (26.4 %) and temporal lobe (20.4 %). Only a minority of glioma are found in regions like the brainstem (4.3 %) or the cerebellum (4.7 %) with its respective clinical representation.[3] The entity shows

increased incidence with age and is mainly diagnosed in elderly patients (75-84 years).[3] Epidemiology studies in the United States of America (USA) show variable incidence based on gender and ethnic origin.[3, 7] Males have a 1.58 times higher risk for glioblastoma than females whereas the tumour is 1.93 times more frequent in people with white skin colour than in people with black skin colour.[3, 7]

According to the CBTRUS Statistical Report of 2018 only 5.6 % of patients survive the first five years after initial diagnosis with slightly better prognosis for patients in younger age-groups. Even in clinical trials with multimodal therapy regimes and selected clinical trial population the median overall survival is in the range of approximately 1.5 years.[8-12] These statistics emphasize the necessity of novel treatment options and the search for novel targets for curing glioblastoma as a nowadays incurable tumour disease.

1.1.2 Gliomagenesis and Risk factors

For the understanding of the tumour entity possible risk factors must be evaluated, as well as the origin of tumour genesis should be studied.

Based on the current state of knowledge, many gliomas develop because of spontaneously acquired genetic alterations, the complete mechanism of gliomagenesis is currently not well understood and many different hypotheses are discussed in the scientific world. The currently favoured model of gliomagenesis starts with a distinct population of stem-like cells which according to Lee et al. are located in subventricular areas.[5, 13] There are data based on animal experiments which support that this cell population which contain well-known driver mutations might be neural stem cells which might collect further somatic mutation in a favourable environmental niche before finally initiate tumourigenesis.[5, 14]

However, there are well-known rare family cancer syndromes like Neurofibromatosis 1 and 2 (NF1 and NF2), Tuberous sclerosis or the Li-Fraumeni Syndrome (p53 gem-line mutation) which show high risk for gliomagenesis and distinct genetic patterns, for instance changes in the *IDH1* or *ATRX* gene which are also known as prognostic markers (see 1.1.3.3 and 1.1.4).[5, 15] As Molinaro et al. describes in his review about molecular and genetic epidemiology of glioma,

more and more genetic risk factors were found in 25 different genetically independent localisation during the last decade which might also play a role in relative risk stratification.[5, 15, 16]

The only confirmed non-genetic exogenous risk factor for glioma is radiation exposure of the brain either through therapeutic radiation or computed tomography (CT) scan in particular during childhood.[17, 18]

1.1.3 Diagnosis

Understanding of the current state of glioma treatment and its development includes several levels of knowledge. Starting by the clinical way to diagnosis which includes clinical examination, risk stratification and several imaging modalities carve out a distinct tumoural behaviour pattern which is finally completed by histological diagnosis referring to a histological classification which reflects tumour biology. The comprehensibility of the diagnostic pattern is fundamental to further evaluate novel tumour associated targets.

1.1.3.1 Clinical presentation

Initial reason for starting the neurological diagnostic algorithm is mainly the description of a novel neurological deficit or symptom. Symptom development and dynamics often give first hints about the malignancy and progression behaviour of potential CNS tumours. High-grad glioma show frequently rapid development of focal neurological symptoms as for instance progressive sensomotoric deficits in a time span of weeks. Whereas low-grade glioma or extra-axially located tumours like meningioma tend to show milder symptom development including slow progression over years.[19] Further questioning concerning risk factors (exogenous and family history) can provide further information concerning possible tumour identity.

As the systematic review of IJzerman-Korevaar et al. shows the symptoms with the highest prevalence during diagnostic phase are cognitive deficits (36 %), seizures (34.7 %), headache (30.5 %), dizziness (23 %) and motor deficits (20.1 %).[20] Moreover, patients mostly present secondary symptoms due to intracranial mass effect, like headache, vomiting and worsening of consciousness.[19]

Visible neurological deficits usually give evidence of the topographical localisation of the lesion. Clinical presentation of glioma including symptom prevalence and subjective burden of symptoms typically changes during disease progression and during or due to therapy. As an example symptoms such as drowsiness, fatigue or aphasia are at the forefront of the patients' medical condition in the terminal stage of the disease.[20] For evaluation neurocognitive worsening tools like the "Mini-Mental-State Test"[21] or the Karnofsky Performance Score (KPS)[22] which gives evidence over the activity of the patient, are easy accessible and important for following clinical development of the patient.

1.1.3.2 Clinical examination and brain imaging algorithm

Besides the explained evaluation of clinical disease presentation brain imaging is one key part of the diagnostic workflow. Due to the European Association of Neuro-Oncology (EANO) guidelines for the diagnosis of adult gliomas, "Magnetic Resonance Imaging (MRI) is the standard method for the detection of glioma".[19, 23] MRI should include T1 3D sequence of at least 2 planes with and without Gadolinium as contrast agent for evaluating contrast agent enhancement of the tumour.[24] Contrast enhancement reveals blood-brain-barrier (BBB) leakage. BBB leakage goes hand in hand with tumour neovascularisation which show strong association with increased glioma malignancy.[24, 25] Moreover ancillary sequences should include fluid attenuation inversion recovery (FLAIR) a T2 sequence which suppress the water signal of the cerebral fluid and offer better visualization of the vasogenic tumour oedema as well as tumour infiltration especially in regions near the cortex or the ventricles which is also interesting in regards of treatment response analysis.[24] Normal T2 sequence is often used for diagnosis of low-grade glioma with strong T2 signal and without contrast agent up-take. Additionally, diffusion weighted imaging (DWI) which offers high sensitivity of microscopic water motion between cells, and the apparent diffusion coefficient (ADC), give evidence of relatively restricted diffusion areas. ADC values inversely correlate with tumour cell density.[24, 26] Besides MRI which gives evidence about anatomical tumour localisation, functional imaging like positron emission tomography (PET) can help to visualize metabolic active

hotspots with high proliferation and membrane turnover.[27] Tracer accumulation patterns help to distinguish different tumour grades, facilitate the biopsy and surgical planning as well as can serve as a prognostic marker during the course of disease.[27, 28] Due to EANO recommendations for PET imaging, amino acid tracers like O-(2-[18F]-fluoroethyl)-L-tyrosine (^{18}F-FET) show in this regard better sensitivity and accuracy as tracers of the glucose metabolism like 18F-2-fluoro-2-deoxy-D-glucose (^{18}F-FDG) which have generally high uptake in brain tissue and show weak glioma specificity and bad signal discrimination.[27, 29]

1.1.3.3 Histological classification of glioma

Definite tumour diagnosis can only be reached by histology acquired by stereotactic biopsy or during maximal safe tumour resection. Until 2016, the World Health Organization (WHO) guidelines for the classification of malignant gliomas consisted of sole histological -morphological differentiations of glioma subtypes.[30] Tumours were divided into four different grades, WHO grade I to IV with ascending malignancy and poor prognosis. However, morphological features and cellular origin as distinguishing features showed high prognosis variation and interobserver variability.[5, 31] With the novelization 2016, the WHO classification integrates histological tumour grade and tissue-based molecular parameters which finally better represent the biological tumour behaviour and show improved patient prognosis assessment.[1, 5, 19]

As Figure 1 shows the diagnosis depends on histological morphology and mainly two well-described molecular biomarkers, the isocitrate dehydrogenase R132 (IDH R132) and the 1p/19q codeletion. Another important role plays the therapeutic prognostic marker O(6)-methylguanine-DNA methyltransferase (MGMT) promoter methylation. Malignant high-grade glioma of WHO grade three and four can be divided into five distinct subtypes.

Histological morphology of malignant gliomas include increase of cellularity, nuclear atypia and increased mitotic activity.[2] Glioblastoma also include central necrosis areas, high neovascularisation and palisade-like arranged tumour cells. Moreover, tumour samples show infiltrative growing patterns with invasive cells inside normal brain tissue regions. [1, 2, 4] Majority of diagnosed high grade

glioma reveal an astrocytic origin und cellular presentation in histological analysis.[1, 5] A subset of tumours present an oligodendrocytic origin which includes histological features like perinuclear halos or branching blood vessels (chicken-wire pattern)[2] which are associated with better prognosis (Table 1: 17.5y) and an IDH-132R mutation.[5] .

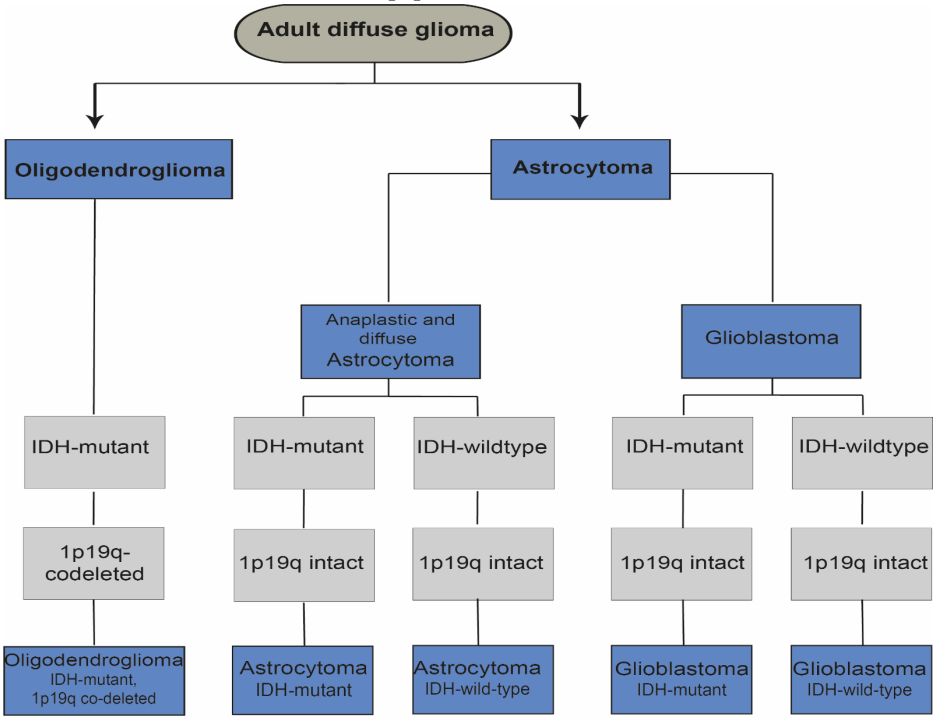

Figure 1: Molecular glioma subtypes according to WHO classification 2016.
Adapted from Louis et al. and Molinaro et al.

The IDH gene codes for an enzyme which normally is key part of the Krebs cycle and converts isocitrate to α-ketoglutarate and $NAD(P)^+$ to NAD(P)H. IDH1 and 2 encode for the enzyme which is located in the cytosol or the mitochondria and also plays a role in the cellular protection against oxidative stress.[32] The most occurring heterozygous missense mutation of arginine to histidine (R132H) leads to a change in the isocitrate binding side. This mutation inactivates the enzyme and enables the enzyme to the production of 2-hydroxyglutarat which might be an oncogenic metabolite.[4, 32] However, IDH132R is highly present in low-grade glioma (70-80%) and is associated with increased promotor methylation in human glioblastoma with more favourable prognosis .[33] As Table 1 shows IDH mutations are associated with younger age at diagnosis, better prognosis and higher chemotherapy sensibility (MGMT methylation) but only represent a small

proportion of annual high grade glioma diagnosis.[5] As a consequence, sequencing of IDH1 and 2 is an essential part of molecular diagnosis.[1]

Table 1: Characteristics of molecular subtypes.
Classification according to the WHO classification 2016. Table adapted from Molinaro et al.

Characteristic	Oligodendroglioma IDH-mutant and 1p19q co-deleted	*Astrocytoma IDH-mutant*	*Astrocytoma IDH-wild type*	*GB IDH-mutant*	*GB IDH-wildtype*
MGMT promotor methylation (%)	≈65-100	≈85	55	≈90	≈40
Median age at diagnosis (year)	44	36	52	38	59
Median overall survival(years)	17.5	9.3	1.9	3.6	1.2
Proportion of 2019 diagnoses (%)	5	12	5	7	71

For distinction between astrocytoma and oligodendroglioma analysis of the gene section 1p/19q is relevant. If fluorescence in situ hybridization (FISH) shows losses of 1p and 19q (1p/19q codeletion) in combination with a mutation in the IDH1 or 2 genes in tumour tissue the diagnosis of an oligodendroglia tumour can be made. As briefly described in the paragraph concerning IDH mutations and shown in Table 1, oligodendrogliomas have a lower tumour grade and more favourable prognosis. [1, 5, 34] Other frequent genetic alterations for oligodendroglioma are mutations in the telomerase regions, like loss of ATRX(Alpha Thalassemia/Mental Retardation Syndrome X-Linked) or mutations which encode for the telomerase reverse transcriptase (TERT).[1, 5, 35]

Another prognostic marker is the epigenetically silencing of the MGMT-gene which is located on chromosome 10.[36] The gene encodes for a DNA-repair protein which is consumed during the DNA repair mechanism. MGMT also repairs alkylating agents induced-DNA lesions, as a consequence high level of MGMT support less chemotherapeutic sensibility.[36] [37] Therefore pyrosequencing for

MGMT hypermethylation for primary and recurrent diagnosis is essential to evaluate chemotherapy options especially in the group of elderly patients.[9, 36, 38]

Most often diagnosed tumour type is the IDH-wildtype glioblastoma, which is associated with older age by diagnosis, worst prognosis and unfavourable occurrence of MGMT hypermethylation.

Besides the mentioned mutations the novel WHO Classification 2016 includes more and more genetic alterations which might define novel tumour subtypes with various disease prognosis.[39] Another well-known example are gain-of-function mutations in the histone H3 gene which is essential for the diagnosis of diffuse midline gliomas. This seventh and newest glioblastoma group is characterised by diffuse growing behaviour in the brain midline region, occurs in a young patient subset and shows poor prognosis despite of primarily histological characteristics.[5, 40]

In addition, with the introduction of the WHO classification in 2016, the intention of a constantly implicating tumour classification was born. During the last years practical recommendations through the cIMPACT-NOW[1][41] workgroup were established and novel biomarkers like the $BRAF^{V600E}$ mutation for H-wildtype/H3-wildtype diffuse gliomas were integrated into the tumour tissue analysis.[42] Besides the clinical used WHO classification there are novel approaches to cluster glioblastoma depending on their somatic genomic alterations. Therefore Brennan et al. and Verhaak et al. performed genomic, transcriptomic, proteomic and methylation status characterisation of over 500 glioblastoma tissue samples and linked their findings to the clinical data of the analysed patients' tissue.[43-45] Finally their examination led to a gene-expression-based molecular classification of glioblastoma which includes a multiparametric landscape of frequent genomic alterations, its cellular origins and prediction of treatment responses.[43] Classification consists of the Classical, Mesenchymal, Proneural and Neural subtypes. The Classical subtype showed combination of amplification of Chromosome 9 together with loss of Chromosome 10 also *EGFR* amplifications are very frequently observed.[43] Mesenchymal glioblastoma show

[1] the Consortium to Inform Molecular and Practical Approaches to CNS Tumor Taxonomy

deletion in the region of the NF1 gene in combination with higher activation of mesenchymal/astrocytic markers and necrosis factors.[43] Proneural tumours characteristically showed genetic alterations in the *PDGFRA* gene, point mutations in the IDH1 gene and overall high expression of oligodendrocyctic signature genes.[43] Neural tumours showed expression of neuron markers (NEFL) and were comparable to normal brain tissue.[43] Genetic based glioblastoma classification gives a comprehensive overview over the somatic mutations in glioblastoma and also helps to better define which preclinical evaluated drugs might be in particular useful in specific tumour subtypes. Moreover, frequently used glioma cell lines and mouse models can be better described by using the glioma classification of Brennan/Verhaak et al.[43, 44, 46] Based on the genomic findings and better understanding of the methylation status in human glioblastoma, a novel DNA methylation-based classification system, consisting of 7 distinct glioblastoma wildtype groups, created by Capper et al. and its implication into routine diagnostic by a free online classifier tool are currently evaluated and extensively tested.[39]

In 2021 a novel EANO-guideline has been published.[23] The evidence-based guideline implemented the on-going diagnostic cIMPACT-NOW updates inside a novel diagnostic and treatment algorithm of human glioma.[23] For example, “biological” WHO grade 4 glioma are introduced as a novel, independent entity based on their distinct mutation profile.[23] Moreover, the guidelines give evidence about newest results of large treatment studies as for example the CATNON Trial which shows improved overall survival in IDH-mutant astrocytoma (WHO grade 3) after radiotherapy followed by concomitant temozolomide chemotherapy.[23, 47]

1.1.4 Therapy strategies

According to the EANO guideline on the diagnosis of adult gliomas, standard of care therapy for glioblastoma consists of maximal safe tumour resection and concomitant, adjuvant chemotherapy with temozolomide and radiotherapy.[10, 19, 23]

Surgical results can be improved by the use of multimodal imaging modalities, like 5-aminolevulinic acid (5-ALA) tissue visualization.[48] Aim of surgery should

be maximal safe resection with improvement and protection of neurological functions.[19] At the moment concomitant, adjuvant temozolomide and radiotherapy, also known as the “Stupp protocol” show better results as mono chemo- or radiotherapy.[10, 36, 38] In the group of elder patients (age over 70) MGMT promotor status decides over therapy modality. MGMT hypermethylation should be treated with concomitant, adjuvant temozolomide and radiotherapy, whereas patients with lack of MGMT methylation should receive radiotherapy alone. [19, 36] Therapeutic monitoring should consist of MRI scans and clinical examination in three months intervals after treatment start or surgery. If there are signs for tumour progression earlier imaging after four to six weeks is possible. Further imaging modalities like FET-PET or Perfusion MRI are useful tools for reevaluation between progression and treatment associated pseudo-progression which often occurs in the first three months after treatment initiation.[19, 24, 27]

Despite of a highly discussed study which used tumour-treating fields as additional intervention, no therapeutic agents have shown an overall survival benefit in comparison to standard of care therapy.[12, 49] In recurrent situation another surgery, reradiation or the use of alkylating chemotherapies like lomustine a nitrosourea compound are frequently performed.[19, 49, 50] Additionally the anti-vascular endothelial growth factor (anti-VEGF)antibody bevacizumab has shown improved progression-free survival times after first diagnosis and after relapse but without influence concerning the overall patients’ survival. However, the antibody has an approval in several countries for recurrent situations and might be helpful in cases with large, symptomatic and steroid-resistant tumours.[11, 51]

Due to the limited pharmacological options for treating glioblastoma multiple study approaches are currently ongoing. In the past, multiple approaches of molecular targeted therapies have failed due to insufficient pharmacological delivery over the blood-brain barrier or systemically occurring critical side effects. [19, 49]

Cancer immunotherapy approaches, which has revolutionized cancer treatment in tumours with high mutational burden like high grade melanoma are currently evaluated in glioblastoma, too.[52] Unfortunately, targeting of Programmed cell

death 1 ligand 1 (PD-L1) in glioblastoma hasn't shown improvement of survival in a randomized phase 3 study (Checkmate 143) in recurrent glioblastoma.[53, 54]

Besides classic chemotherapeutic agents and immune checkpoint inhibition other available, possible treatment candidates are eagerly evaluated. Intrinsic glioma targets like tyrosine kinase receptors (EGFR or mTor), cell cycle or apoptosis regulating pathways (p53 or TERT) might be promising approaches to prevent tumour growth and disease progression.[49] Conducted clinical trials showed two major problems. On the one hand used drugs often showed inactivity in the cerebral milieu because of incapability of overcoming the blood-brain barrier, on the other hand the used agents showed huge systemic side effects or the tumours showed unstable target expression due to therapy.[49, 55]

Another currently studied approach is the target of microenvironmental targets and its containing cellular structures. In this context novel treatment options like immune checkpoint inhibition, Chimeric Antigen Receptor-(CAR) T-cell or personalized tumour neoantigen vaccination are promising techniques for tackling known problems of glioma treatment approaches.[49, 56, 57] Despite of novel treatment approaches and several ongoing clinical trials, novel stable treatment targets and potent inhibitors are urgently needed for securing possible treatment successes and finally improve patients' outcomes sustainably.

1.2 Glioma microenvironment

If we look deeper into gliomagenesis the question arises how glioma cells interact with its environment and how the tumour can establish a pro-tumourgenic environment to further expand its mass. The understanding of the tumour microenvironment (TME) and its key players might help for a better understanding of tumour formation and might support the finding of novel therapeutic targets. The following paragraphs outline the basic microenvironmental landscape and focus on the targeted molecular structures of the performed study: the colony stimulating factor 1 receptor (CSF1R) and the programmed death cell receptor 1 (PD1). Furthermore, it provides a short description of the principles of immunotherapy and its application in the field of neuro-oncology.

At the end of the 20th century it was shown that there are strong connections between inflammatory processes caused by infectious disease and the occurrence and course of disease of several cancer types.[58] For example complete immunosuppression through infectious disease like AIDS caused by the HI virus leads to both AIDS-related cancers (for instance the Kaposi sarcoma) and unrelated cancer types of various localisations.[58, 59] In contrast, long lasting inflammatory processes like liver cirrhosis are strongly linked to high cancer incidence, like the hepatocellular carcinoma.[58, 60] These two opposite findings support the conclusion that the interaction between on the one hand tissue-related host or tumour cells and on the other hand stromal and immune cells which are located in the surrounding microenvironment is essential for tissue or tumour development and condition.[58, 61] The bi-directional interaction between tumour cells and tissue-specific cells represents a highly variable, tissue homeostasis disrupting communication which is highly flexible during the course of tumour genesis and progression.[58] The term tumour microenvironment, short TME, thus describes the crosstalk between tumour cells and surrounding host cells. The TME as a subject of cancer research and as a potential target for novel tumour treating therapies is currently eagerly studied and evaluated.

The TME consists of various innate and adaptive immune cell types, stromal cells, the surrounding extracellular matrix and complex networks of blood and lymphatic vessels which surrounds and interacts with the mass of tumour

cells.[62] Tumour cells can stimulate surrounding and immigrated cells by the use of chemoattractant substances like CSF1 or MCP1. In a second step tumour cells can re-educate surrounding host-cells to change their phenotype for releasing pro-tumourgenic factors like Il6 or EGF themselves.[58, 61-63]

The two most frequent occurring and most studied immune cell types in diverse tumour entities are macrophages/microglia and lymphoid cells, more specific T cells.[62] Tumour cells can release several different cytokines which attract macrophages and lead to macrophage infiltration into the tumour tissue as visible in Figure 2. In general, macrophages play a key role in inflammation, tissue homeostasis and tissue repair.[64] They are capable of phagocytosis of cellular compartments, cancer cells or microbes.[64] Macrophage development start in the bone marrow, followed by circulating in the blood as monocytes, finally they infiltrate a distinct tissue type by chemotaxis and become resident as tissue specific macrophages like osteoclasts in the bone or Kupffer cells in the liver.[58, 63, 65] Their most relevant feature is their high functional plasticity.[62] Macrophages and microglia are very sensitive to external stimuli, like hypoxia, necrosis, cytokines, chemokines, metabolites and physical stimuli.[58, 61, 62] As a consequence, they can quickly change their phenotype, also called polarization in this regard and can react on the changing condition of their environment.[63] They are capable of phagocytosis and can release several cytokines which influence cellular and stromal composition of their environment.[63] In cancer diseases accumulation of macrophages which have been attracted by the tumour and release pro-tumourgenic factors is associated with poor prognosis and higher malignancy in several solid tumour entities.[66] Moreover, several studies in breast cancer and gliomas showed that tumour-associated macrophages (TAMs) can support tumour infiltration and migration by the use of the signalling CSF1R/CSF1 and EGF/EGFR-axis.[67, 68]

The TME in the brain also called the glioma-associated microenvironment has some characteristic differences in comparison to the TME of other tumours. The brain itself was long described as an immune privileged organ. Inflammatory processes in the healthy brain are very rare and are strongly linked to neurodegenerative processes.[58] Moreover, inflammation and resulting tissue

swelling is highly dangerous in the brain because of the lack of space and the risk of brain herniation.[61] Consequently, there are several cellular and structural means which prevent inflammatory processes in the CNS. Primarily, the BBB blocks over 98% of molecules and also prevents the infiltration of circulating bone-marrow derived immune cells.[61] Over a long period of time it seemed like the CNS does not show any lymphatic vascularity which supported the hypothesis that the brain is strongly protected from the systemic immune system and inflammatory processes. Due to the findings of Louveau et al. in 2015, the CNS has a highly complex network of lymphatic drainage mainly located in the meninges which enables T cell circulation and is connected to the deep cervical lymph nodes.[69] Another difference is the composition of the extracellular matrix (ECM). In the brain the ECM is highly immunosuppressive and supports the stability of the BBB. The ECM consists of neurons, astrocytes and the resident immune cells called microglia.[61, 63] Resident microglia show comparable characteristics to bone marrow-derived macrophages. However, they have a different cellular origin. Microglia progenitor cells develop in the embryonic yolk sac which is part of the neuroepithelium and migrate into the brain during brain development, whereas macrophages continuously develop out of mononuclear cell populations in the bone marrow.[63] Microglia show cellular longevity with slow local proliferation and build a stable cell population in the CNS with a characteristic presentation of surface markers.[61, 63]

Microglia and peripheral attracted macrophages play a key role in the glioma-associated microenvironment. Several studies show that over 30% of cellular glioma mass is formed by TAMs consisting of both cellular populations.[63, 70] Moreover, histologic studies including TAM marker CD68 showed that increasing numbers of macrophages in glioma tumour tissue showed increased malignity and reduced progression-free survival.[71] Additionally, Simmons et al. shows that even in low grad gliomas like the often occurring pilocytic astrocytoma have significant increased microglial markers in comparison to normal brain tissue (15-30% vs. 10-15%).[72] Under physiologic conditions macrophages and microglia have a distinct but hardly distinguishable surface signature. Over a long period of time both populations were differentiated by CD45 expression. Microglia normally

express low levels of CD45 with strong levels of CD11b whereas peripheric infiltrating macrophages express high levels of CD45.[63] Despite of studies which support that greater proportion of TAMs in glioblastoma are bone-marrow-derived macrophages, the differentiation of both cellular populations by FACS or IHC in particular in the TME are discussed controversially.[73] Inside the TME the phenotypes of macrophages and microglia change due to external tumoural stimuli, consequently cellular origin tracking becomes even more complicated without genetic lineage tracking.[61]

Characterising the phenotype and its consequences for promoting glioma invasiveness and growth might give evidence about potential target points for re-education of macrophages by pharmaceutical intervention.

In general, macrophage polarization *in vitro* was classified in 2 clustered polarization states, M1 and M2. Macrophages are stimulated *in vitro* towards M1 status by addition of toll-like receptor 4 ligands or interferon-y.[74] This phenotype shows proinflammatory characteristics and mostly anti-tumourgenic characteristics which is supported by a study of Zeiner et al. which shows better survival of high-grade gliomas which express CD74, a potent marker of M1 polarization.[63, 75] M2 polarization *in vitro* occurs after stimulation with Interleukin (IL)-4, 10 and 13.[74] M2 polarization and its subgroups are more often found in several tumour types and is associated with tumour promoting factors.[63, 76, 77] For example *in vivo* work of Pyonteck et al. shows that culturing microglia with macrophage-colony stimulating factor 1 (m-CSF1) leads to M2 polarization as well as inhibition of colony-stimulating factor 1 receptor (CSF1R) re-educate macrophages and shifts gene expression backwards to an more anti-tumourgenic M1 polarization status.[77] Novel approaches like the work of Szulzewsky et al. which try to cluster RNA expression profiles of glioma-associated macrophages (GAMs) show that GAMs express both M1 and M2 specific genes as well as over 100 specific genes which are only enriched in GAMs.[78] This work highlights the fact that bipolar classification of macrophages phenotypes is only very limited useable in *in vivo* studies and specific markers for characterizing GAMs phenotypes might be helpful to evaluate composition of the TME.

As Figure 2 shows cross-talk between TAMs/GAMs and glioma cells is highly active. Initially, glioma cells secrete several chemoattractants which lead to recruitment of resident microglia and peripheral bone marrow-derived macrophages. Chemoattractant substances are the monocyte chemoattractant protein-1 (MCP-1), SDF-1or ATP.[63] Glioma cells secrete GM-CSF1 and CSF1 which lead to macrophages recruitment and increases invasiveness of gliomas.[63] For instance Coniglio et al. show that inhibition of CSF1R *in vivo* lead to decrease of GAM numbers as well as decrease of glioma invasiveness which highlights the important role of the CSF1/CSF1R axis. [67]

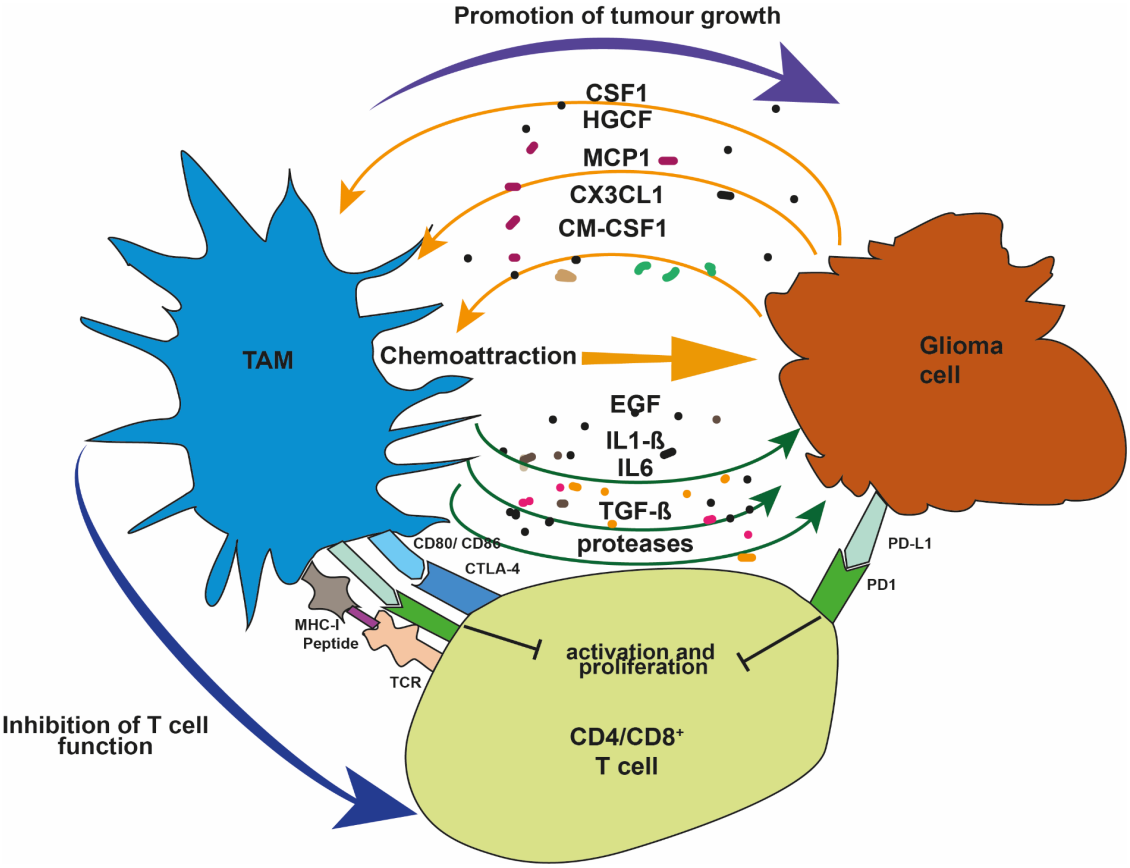

Figure 2:Interaction inside the glioma-associated microenvironment
Adapted from Quail et al. 2017 and Hambardzyumyan 2016.

In this context epidermal growth factor 1 (EGF) released by GAMs and its binding at the EGF receptor (EGFR), frequently expressed by glioma cells, promote higher tumour invasiveness and cell motility due to primarily CSF1 release by glioma cells.[67] Recent studies showed that glioma cells with stem cell characteristics which most often are located in the subventricular niche might

have an even stronger effect on GAMs attraction by use of periostin.[63, 79] Besides EGF, TAMs release several other cytokines due to external stimuli which change the TME and support tumour genesis.[67] In comparison to peripherical circulating macrophages, TAMs and GAMs release less numbers of proinflammatory cytokines. Moreover, they show reduced capacity of activating T cells caused by reduced expression of T -cell interacting cofactors like CD40 or CD80 which is illuminated in comprehensive FACS analysis performed by Hussein et al.[61, 80]

GAMs show several ways how they support tumour growth. One eagerly studied cytokine in this regard is the microglial release of transforming growth factor ß (TGF-ß). As closely reviewed by Hambardzyumyan et al. TGF-ß is released by GAMs and lead to increased expression of matrix metalloprotease-2 (MMP-2) by glioma cells. The proenzyme of MMP-2 is then cleaved and activated by membrane-bound metalloprotease (MT1-MMP) which is translated by GAMs. Interestingly, glioma cells boost MT1-MMP expression by several stimuli like versican a proteoglycan. Activation of MMP-2 leads to strong degradation of the ECM, consequently invasiveness and migration of glioma cells is increased.[63] This exemplary cross-talk highlights the close cooperation and well-orchestrated interaction between tumour cells and tissue-specific immune cells inside the TME. Besides promoting glioma invasion and migration, GAMs also release several factors which support tumour vascularisation by increasing secretion of vascular endothelial growth factor (VEGF) and infiltration of peripheral macrophages by weakening the BBB by supporting higher numbers of metalloproteinases and disrupting vessel integrity and function.[63] Moreover, they can secret pro-inflammatory molecules, like Interleukin-1ß, CXCL10 or tumour necrosis factor α (TNF α) which enhances tumour growth.[63, 81]

Besides GAMs, lymphoid immune cells consisting of T, B and natural killer (NK) cells whose development primarily take place in the bone marrow or the thymus, might be a promising therapeutic target inside the TME.[61] T cells can be distinguished through different surface markers. All T cells express CD3. T helper cells (T_H cells) which play the key role in the recognition of antigens and induce immune response by release of several cytokines which attract cytolytic active

immune cells like macrophages or NK cells, express CD4 and present antigens by major histocompatibility complex II (MHC II). Cytotoxic T cells (T_C cells) which can be mostly distinguished through CD8 expression interact with endogenous cells by binding of the T cell receptor (TCR) with the major histocompatibility complex I (MHC I).[64] If the subset of antigens presented by MHC I changes due to infection or tumoural proliferation, T_C cells can induce apoptosis and promote the presentation of cellular antigens of the nearest cells.[82] As Figure 2 shows affinity of interaction between $CD4^+$ or $CD8^+$ T cells and MHC expressing cells depends on several expressed cofactors which build the “immunological synapse”. There are factors which either improve affinity or act as “immunological breaks”.[64] A very important axis for the interaction between antigen presenting cells (APCs) and all $CD4^+$ or $CD8^+$ cells is expression of CD80/86 also known as proteins of the B7 family and CD28.[64] CD80/86-CD28 axis is strongly inhibited by so called “immune checkpoints”. Immune checkpoints are receptor interactions which weaken APC or tumour cell/ T cell interaction. Well studied molecules which act as immune checkpoints are cytotoxic T-lymphocyte-associated protein 4 (CTLA4) PD1, mucin-domain containing-3 protein (TIM3) or lymphocyte-activation gene 3 (LAG3).[49, 64] Physiologically activated immune checkpoints prevent hyperinflammation and serve as negative feedback loops in acute infection states.[58, 83] However, tumour cells often express and promote high numbers of molecules which act as immune checkpoints as described above on their surfaces by autocrine signalling pathways.[61, 64] Thus, tumours with high expression of immune checkpoint molecules can escape T cell recognition and promote T cell dysfunction also known as T cell exhaustion by release of immunosuppressive acting cytokines as the earlier described cytokine TGF-ß.[83] T cell exhaustion can be defined as the inability of T cells to react to activation stimuli due to insistently elevated expression of inhibitory receptors. As Berghoff et al. shows by immune histochemistry, PD1 and tumour infiltrating lymphocytes (TILs) are present in a large cohort of glioblastoma.[84] Therefore, inhibition of the PD1/PD-L1 axis in combination with re-education of TAMs might be an interesting approach to reprogram the glioma-associated microenvironment.

1.2.1 Colony-Stimulating Factor-1 (CSF1R)

Key factor for macrophage/microglia survival and differentiation inside the glioma-associated microenvironment is CSF1R[61, 63]. CSF1R is a receptor tyrosine kinase and primarily expressed on myeloid cells and neural lineage cells.[85] CSF1 and interleukin-34(IL-34) act as ligands of CSF1R.[85] Both glycoproteins share specific α-helical secondary peptide structures and bind to overlapping regions of the CSF1R binding site. CSF1 exclusively binds CSF1R. However, IL-34 also interacts with receptor protein tyrosine phosphatase ζ (PTP-ζ) which is mainly expressed on neuronal progenitor and myeloid cells. [85, 86] Inside the brain, CSF1R plays several roles. Primarily, CSF1R is essential for neuronal development. CSF1R is required for both microglial and neuronal cell development and is essential for maintenance of microglial cell population.[85] Besides, CSF1 and IL-34 is primarily secreted by neurons depending on cerebral localisation. Moreover, CSF1R is upregulated after neuronal damage and supports survival of damaged neurons.[85] As a consequence of its functions, CSF1R loss of function mutations lead to a dominantly inherited form of dementia also known as adult-onset leukoencephalopathy with axonal spheroids and pigmented glia (ALSP).[85] Leading symptoms are frequent epileptic seizures and loss of motoric functions.[85] Besides the mentioned CSF1R/CSF1 signalling inside the TME, upregulation of CSF1R plays an important role in neurodegenerative disease. For instance, CSF1R is upregulated in the Alzheimer disease and attracts microglia and plays a key role in plaque formation. *In vivo* studies showed that inhibition of CSF1R in a Alzheimer mouse model led to improved neurological and behavioural performance.[87]

As closely described, CSF1R is highly expressed on TAMs. *In vivo* studies by Pyonteck et al in which CSF1R was inhibited by a small molecule kinase inhibitor (BLZ945) showed improved survival and reduced tumour size.[77] However, TAMs were not depleted but showed signs for phenotypic switch by increased transcription of M2 relevant genes.[77] Besides these findings other studies showed similar findings with other inhibitors. Overall, inhibition of CSF1R can be achieved through 3 main ways. First, CSF1R ligand binding can be blocked by epitope binding of respective therapeutic antibodies. Secondly, dimerization of

the transmembrane domains can be blocked by an antibody (RG7155) as closely shown by a study of Ries et al.[88] Lastly, small molecule inhibitors penetrate through the membrane and block the CSF1R function as a tyrosine kinase.[89]
These shown inhibitory possibilities are also used in clinical trials of several tumour types. Most promising results showed a Phase I trial with RG7155 in diffuse-type giant cell tumour a rare tumour disease with CSF1R overexpression. CSF1R inhibition led to significant reduction of $CSF1R^+$ macrophages and clinical responses. *In vivo* studies of CSF1R targeting in gliomas led to a clinical phase II trial in recurrent glioblastoma with the small molecule inhibitor PLX3397. PLX3397 showed well tolerance and consistent crossing of the BBB.[90] However, treatment showed no efficacy which underlines the importance of testing novel combination therapy regimes including CSF1R inhibition.[90]

1.2.2 Programmed-Death Cell Receptor 1 (PD1)

The PD1/PD-L1 axis is one of the most studied immunological escape mechanisms of tumour cells. As mentioned above, PD1/PD-L1 are immunological breaks for the interaction between host cells and T cells. PD1 is a transmembrane protein with the length of 288 amino acids.[91] PD1 consists of 3 main motives. First motive is the presentation of a signal sequence and the immunoglobulin variable region. Second is a consistent transmembrane domain, followed by the third motive a cytoplasmic tail.[91] PD1 is mainly expressed on T cells. Lower PD1 levels are found on B cells, monocytes and APCs like Langerhans' cells, too.[91] PD1 interacts with 2 ligands, PD-L1 and 2, which are both members of the protein B7 family. PD-L1 is physiologically expressed in low levels on APCs. Moreover, diverse human host cells express PD-L1 like endothelial cells and immune privileged tissues like eye and placenta.[91] PD-L2 expression on dendritic cells and macrophages depends on proinflammatory stimuli mainly located in alveolar tissue.[91] Upregulation of PD1 is naturally induced after T cell activation caused by TCR-MHCI/ II binding for regulation of immune responses and to prevent autoimmunity.
Upregulation of inhibitory cofactors of T cell binding including PD-L1 is found in several cancer types and was discovered as potential treatment target. Tumour boosts upregulation by secretion of cytokines and escape T cell recognition.

Targeting of coinhibitory factors was the beginning of the area of tumour immunotherapy which was rewarded with a Nobel prize for James Allison and Tasuku Honjo in 2018. [91] First clinical application was the treatment of advanced melanoma by targeting with an anti-CTLA4 antibody called Ipilimumab.[92] Survival benefits were improved by combining anti-CTLA treatment with anti-PD1 targeting in multicentre study by Wolchok et al.[52] The promising results led to multiple studies in diverse cancer types, including non-small cell lung cancer and renal cell carcinoma. Initially, studies were conducted in tumour diseases that are characterized by a high mutational burden.[46] These tumours present a high number of somatic mutations, which lead to a high presentation of antigens that could be recognized by T cells as foreign to the body. [46, 91] Due to Vogelstein et al. and comprehensive analysis by Brennan et al. glioblastoma show variable subsets of somatic mutations and antigen fragments, too. [44, 46] Therefore anti-PD1 therapy regimes were tested in a large cohort of recurrent glioblastoma in a phase III study (checkmate 143). However, the monotherapy arm with anti-PD1 monotherapy had to be closed and did not reach the primary endpoint.[53, 54] Unfortunately, the CheckMate-548 trial which tested anti-PD1 treatment in newly diagnosed glioblastoma equally could not reach primary endpoint and the PD1 arm had to be closed at the end of 2020, too[93]. However, testing novel therapeutic approaches including anti-PD1 treatment are eagerly studied. As an example, Cloughesy et al. could show in a small cohort of resectable glioblastoma that neoadjuvant treatment with Pembrolizumab (anti-PD1) improved survival and led to decrease of PD1 expression whereas T cell associated genes were upregulated.[94]
Consequently potential combination therapy partners for anti-PD1 approaches might improve overall immune therapeutic efficiency.

1.3 Characteristics of distinct glioma mouse models.

In the field of preclinical *in vivo* glioma research, several mouse models are available. The fundamental understanding of major functions of these models and mapping them including their advantages and limitations is necessary for several reasons. First, choosing the suitable model in context of the scientific question is the basis for answering the scientific questions. Secondly, interpretation of results

acquired by mouse models always reflect the strengths and limitations of the used system and therefore should be considered during the interpretation process.

In general, several findings of molecular mechanisms of tumour development were found in *in vitro* studies. For the complex crosstalk of tumour cells and its TME, xenograft mouse models can be useful tools. Xenograft models offer several opportunities to fully observe invasiveness, angiogenesis and systemic growing behaviour of tumour diseases. For a glioma model there are several facts to consider. A glioma model should show histological similarities including cellular heterogeneity of human gliomas. Moreover, tumours should have similar genetic background and should be grown orthotopically to reflect intraparenchymal invasiveness including interaction to resident host cells. In this regard the model should include complete immunocompetence.[95] Considering technical aspects, xenograft models should offer technical reproducibility which include high rates of tumour formation after implantation and practical handling of cellular components or plasmids.[95]

Available Glioma mouse models can be divided into 4 categories: chemical induced long term tumour cell lines and spontaneous developed tumour cells which have been isolated. Tumour induction is achieved by intracranial cell implantation. On the other hand, humanized mice in combination with primary patient derived glioma cell lines and genetically engineered models (GEMs) are novel tools for study gliomagenesis. [95, 96]

Every categorized mouse model has its advantages and disadvantages. Chemical induced gliomas are often established using alkylating substances like nitrosoureas.[95] Alkylates lead to various unspecific genetic alterations and somatic mutations which cause strong heterogeneity of different chemical induced models. One advantage is the easy and well-studied orthotopic implantation of chemical induced gliomas. Moreover, the established cell lines are mostly discovered in the 1980s and as a consequence very closely studied.[95, 96] Disadvantage is the development process which mainly depend on teratogenic effects which does not reflect *in vivo* gliomagenesis.[95] The most common glioma model in this category is the GL261 cell line which was induced by methylcholanthrene by Ausman et al. and implanted into C57BL/6 mice in the

1990s.[97] GL261 cells harbour several mutations often occurring in glioblastoma including mutations of p53 suppressor genes. Moreover, high MHC I levels enables the cell line for immunotherapeutic experiments.[95, 96] GL261 forms tumours *in vivo* which show histologic similarities to human glioblastoma including cellular pleomorphisms and angiogenesis.[96]

Cell lines from spontaneous developed glioma are common xenograft models, too. In the 20th century Sampson et al. isolated several spontaneous gliomas in the VM/Dk mouse stain and established the cell line SMA560 which shows high levels of astrocytic marker GFAP in combination with low S100 expression and mimics typical features of an anaplastic glioma.[96, 98] Moreover, MHC I is stably present on SMA560 cells which enables tumour cells to interact with T cells.[98] Moreover SMA560 cells secret high levels of TGF-ß which is as described in 1.2 essential for the establishment of an immunosuppressive TME.[61] Unfortunately, there are several studies which indicate that spontaneous emerging glioma cell lines isolated from mice or patient's often change their characteristics if they are split several times, therefore low passage numbers are necessary for performing reproductive animal experiments.[99] Overall, spontaneously emerging tumours better reflect the nature of gliomas and their development than chemical induced glioma cell lines.[95, 96] Consequently, spontaneous induced models which are immunocompetent, syngeneic and can be orthotopic implanted offer multifaceted research applications like immunotherapeutic drug testing.[95, 96]

Besides spontaneous and chemical induced gliomas it is possible to implant fresh isolated patient-derived glioma cells in immunocompromised mice.[100] These models are called patient-derived orthotopic xenografts (PDOX).[100] Primary cells form spheres *in vitro* in the presence of growth factors like epidermal growth factor (EGF), basic fibroblast growth factor (bFGF) and insulin.[95] PDOX models best represent the heterogenous glioma biology. However, patient-derived cells frequently show slow growing behaviour and generally require optimal conditions for expansion and maintenance. Additionally, rates for successfully isolated glioma cells are very heterogeneously.[95] Unfortunately approaches for studying interaction between PDOX and the immune system are very limited and difficult

due to the long establishment process of humanized mice.[100] Humanized mice are mice which show the patient-derived immune signature which is established either by haematopoietic progenitor cell implantation of the respective patient or by molecular biologic means which genetically modify the MHC signature of the mice.[100] Consequently, more practical workflows for establishing humanized mice are urgently needed. Despite of described problems, PDOX are essential models for gliomagenesis and offer several possible applications for drug testing, particularly in zebrafish models.[100] The forth group are genetically engineered models (GEMs) using several diverse delivery systems. In contrast to the other 3 approaches, GEMs do not depend on implantation of a huge number of tumour cells which interact with the organism.[95] Tumour initiation in GEMs is initiated by the organism itself and does not necessarily need a cerebral trauma as a starting point of tumour initiation.[56, 95, 96] GEMs can be developed by using transgenic mice which either include gain of function by overexpression of specific genes or knock-out genes.[95] They can be conceived by germline modification or somatic gene transfer systems.[95]

1.3.1 The RCAS/TVA system as an example for GEMs in glioma research

A somatic gene delivery system called replication-competent avian sarcoma-leukosis virus long terminal repeat with splice acceptor (RCAS) /tumour virus A (TVA) is one of the most frequently used GEMs in glioma research and was used in the following study, too. This retroviral delivery system is able to transfer gene sizes with 2.6 kilobases (kb) contained in an RCAS virus into somatic cells presenting the TVA receptor.[101] As Figure 3 shows plasmid coding for the RCASBP, a retroviral avian leucosis and sarcoma virus (ALSV) contains the *ALSV subgroup 1 envelope*, which enables the virus in combination with the genes *gag* and *pol* to infect cells in a TVA-dependent manner.[101] Virus production takes place in embryonic chicken fibroblast cells called DF-1.[101] DF-1 cells which express the TVA- receptor offer stable virus formation and multiplication *in vitro*.[101] The RCAS/TVA system is available with several driver mutations which induce tumour formation. In our case we used an RCAS virus containing Platelet-derived growth factor B (PDGFB) amplification in combination with a genetically modified mouse with lack of the cell cycle regulator INK4a-ARF

in their genetic background (129S.Tg(NES-TVA)-Ink4a-/-).[102] Both alterations are frequently found in glioblastomas and ensure reproducible tumour formation of high grade gliomas of an proneural subtype as shown by Hambardzumyan et al.[95, 102, 103] However, the used genetic background including deficiency of tumour suppressor genes Ink4/-ARF lead to sarcomas and lymphomas in the animal strain starting around the age of 30 weeks.[104]Besides the described oncogenes there are many other combinations of oncogenes including mutations of the RCAS-gen and PTEN-deletions as detailed reviewed by Stylli et al, available. [95]The XFM mouse strain includes a *Cre/loxP system* which provides expression of the TVA-receptor only in GFAP positive cells as established by Dai et al.[105]For consistent virus production and due to the lack of envelope stability, implantation of DF-1 cells transfected by RCAS viruses is necessary for tumour initiation.[101]

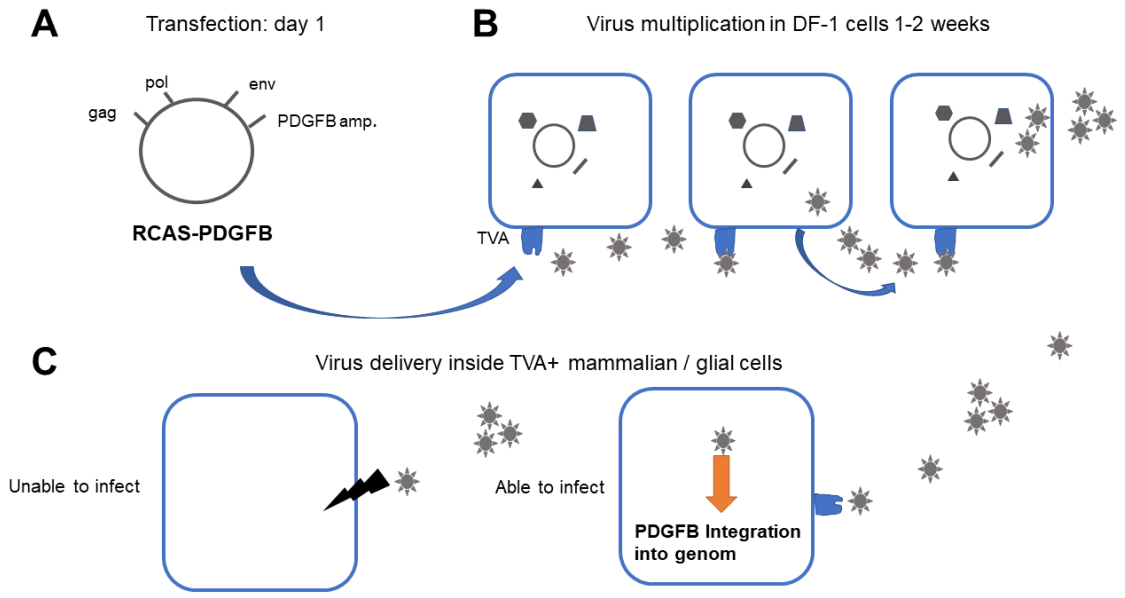

Figure 3: Systematic overview about RCAS/TVA function.
(A): Schematic construction of RCAS-PDGFB plasmid, including PDGFB amplification and sections coding for gag, pol and env. (B) After transfection virus (grey stars) multiplication takes place in DF-1 cells. Plasmid can enter using the TVA receptor. Retrovirus multiplication leads to infection of adjacent cells. (C) Virus producing cells are implanted into mammalian animals. Virus can enter cells which express TVA receptors and can deliver target gene (PDGFB) into mammalian cells. Modified and adapted from von Werder et al.

All in all, the used GEM model using the RCAS/TVA system offers tumours which show signature characteristics of human glioblastoma, reflecting natural course

of disease and are usable in several fields of scientific applications including testing of immunotherapies as shown for instance in the earlier cited study by Pyonteck et al.[77, 95]

1.4 Objective of this study

Despite of multimodal therapy regimes the media overall survival of patients with glioblastoma diagnosis is still very devastating and in the range of 1.5 years.[10, 11, 38] Therefore, novel therapeutic strategies are urgently needed and eagerly studied.[49]

Due to the resounding success in metastatic melanoma, immunotherapeutic approaches which target the interaction between tumour cells and their TME are being discussed and tested in a broad range of tumour entities. [52] Particularly the expectations in the field of brain tumour research were very high after first promising preclinical data have been published.[106] However, first clinical studies with anti-PD1 antibodies could not show an improvement in patients prognosis in a cohort of recurrent glioblastoma.[53, 54] As a consequence therapeutic targets inside the TME and respective inhibitors are eagerly sought and hotly discussed in the field of neuro oncology. The rational is to find possible combination partners for checkpoint-inhibitors like anti-PD1 agents to enhance their efficacy. [49]

In the following study the CSF1R/CSF1 axis has been chosen as a potential therapeutic target inside the glioma-associated microenvironment. CSF1R is mainly expressed on TAMs which are highly abundant in the glioma-associated microenvironment.[63] As described in 1.2.1, CSF1R plays an important role in the survival and differentiation of TAMs. Therefore, CSF1R might be a very promising targetable structure inside the TME as well as a potential combination partner of checkpoint inhibitors like anti-PD1 antibodies.[63, 71, 107]

Previous published immunohistochemical studies showed TILs infiltration and expression of TILs markers including presence of anti-PD1/PD-L1 in unmatched subsets of glioblastoma tissue samples.[84]

First objective of the following study was to assess the presence of CSF1R by immunohistochemistry in a patient cohort containing exclusively matched tissue samples after first diagnosis and after first relapse of disease. Particularly, the question if CSF1R expression depend on received therapy modality or differ in primary and recurrent tumour tissue seemed to be of special interest for defining the potential applicability of a CSF1R inhibition in clinical translation. Moreover,

analysed CSF1R expression pattern should be discussed and correlated with other histologic TMA and TILs markers in the same patient cohort.[108]

The next step was to inhibit CSF1R *in vivo* with a 2G2 antibody in the immunocompetent VM/Dk glioma mouse model using SMA560 cells. Furthermore, combination therapeutic strategies combining anti CSF-1R and anti-PD1 inhibition were performed.
Second study objective was to assess if the TME changes after targeting of CSF1R. Referring to earlier published studies with small-molecule inhibitors against CSF1R experimental hypothesis was that CSF1R inhibition and its combination with anti-PD1 leads to re-composition of the glioma-associated microenvironment. [77, 88] This was investigated by immunohistochemistry of post-treatment glioma mouse tissue focusing on T cell and TAM markers. Histologic analysis includes staining signal quantification.

Moreover, a widely used PDGFB-driven immunocompetent glioma model using the RCAS-TVA delivery system was established and characterized as part of this thesis [101, 102]. As explained in detail in 1.3, GEMs do not depend on orthotopically syngeneic tumour cell implantation; tumours are initiated by the mice themselves and better reflect tumour biology and course of disease.[95, 96] Therefore utility for immunotherapeutic preclinical studies was evaluated by multimodal imaging including T1 contrast enhanced MRI scans and FET-PET focusing on tumoural growth kinetics. Additionally, *ex vivo* IHC characterization of the TME was performed and compared with the VM/Dk glioma mouse model.

With the knowledge gained from the therapeutic studies in the VM/Dk mouse model and the characterization of the PDGFB-driven mouse model a second therapy study was performed. The experimental setup included mono- and combination therapeutic strategies of anti-CSF1R and anti-PD1 inhibition. Onset of neurological symptoms (Table 5) was defined as study endpoint. Experimental hypothesis was that combination strategies might lead to later onset of neurological symptoms.

As an experimental outlook for further *in vivo experiments*, fluorescence labelling of long-term glioma cell lines was performed. As extensively described in the

literature fluorescence labelling offers the possibility of *in vivo* bioluminescence imaging of tumour formation and growth. This might be helpful in upcoming preclinical *in vivo* studies with larger treatment cohorts testing a broader spectrum of combination therapeutic approaches.

In summary, the work described here aims to depict the presence of CSF1R inside the human glioma-associated microenvironment and evaluate CSF1R as a potential therapeutic target in combination with immune checkpoint inhibition of PD1 in two preclinical glioma mouse models.

2 Material and Methods

2.1 Materials

2.1.1 Chemicals, Kits and Cell Culture Media

Table 2: Chemicals, kits and cell culture media

DESCRIPTION	SUPPLIER
Antibiotics	
Ampicillin 100mg/ml	AppliChem GmbH, Darmstadt (DE)
Gentamycin 50mg/ml	Gibco, Thermo Fisher Scientific, Waltham (US)
Puromycin 1µg/µl	Sigma-Aldrich, Munich (DE)
Dyes	
6x Gel loading dye purple (no SDS)	NEB, Ipswich (US)
Trypan Blue Stain (0.4%)	Gibco, Thermo Fisher Scientific, Waltham (US)
Enzymes and Restriction buffers	
10x CutSmart® buffer	NEB, Ipswich (US)
BstBI	NEB, Ipswich (US)
EcoRI-HF	NEB, Ipswich (US)
NHeI	NEB, Ipswich (US)
Nuclease-Free Water	Thermo Fisher Scientific, Waltham (US)
SpHI-HF	NEB, Ipswich (US)
XbaI	NEB, Ipswich (US)
Gel electrophoresis and Bacterial work	
Gel-red nucleic acid gel strain	Biotium, Fremont (US)
LB Agar, Vegitone	Sigma-Aldrich, Munich (DE)
LB Broth, Vegitone	Sigma-Aldrich, Munich (DE)

LE agarose	Biozym Scientific, Hessisch Oldendorf (DE)
Purple 2-log DNA ladder	NEB,Ipswich (US)
S.O.C medium	Invitrogen, Thermo Fisher Scientific, Waltham (US)
TAE Buffer (50X)	AppliChem GmbH,Darmstadt (DE)

Immunohistochemistry and Animal work

Acetic acid (glacial)100%	Merck, Milipore, Burlington (US)
BLOXALL™ Endogenous Peroxidase and Alkaline Phosphatase Blocking Solution	Vector Laboratories, Burlingame (US)
Eosin G- solution 0,5% aqueous	Carl Roth, Karlsruhe (DE)
Ethanol absolute	AppliChem GmbH,Darmstadt (DE)
Fentadon® 50µg/ml for animal use	WDT, Garbsen (DE)
Gadovist® contrast agent 1,0 mmol/ml	Bayer Vital, Leverkusen (DE)
Isofluran CP® 1ml/ml	CP Pharma, Burgdorf (DE)
Ketamin 100mg/ml for animal use	WDT, Garbsen (DE)
Mayer's Haematoxylin Solution	Sigma Aldrich, Munich (DE)
Methanol	AppliChem GmbH,Darmstadt (DE)
Path® Coverquick 2000	VWR International, Darmstadt (DE)
Phosphate buffered saline 10x concentrate	Sigma-Aldrich, Munich (DE)
qPCR Mastermix Plus for SYBR GreenI	Roche Diagnostics, Basel (CH)
Rimadyl® Carprofen 50mg/ml Injectionsolution for cattle	CP Pharma, Burgdorf (DE)
Sedaxylan® 20mg/ml for animal use	WDT, Garbsen (DE)

Tissue-Tek®O.C.T™ Compound Containing 125ml	Sakura Finetek (US)
Triton X-100	Carl Roth, Karlsruhe (DE)
Tween®20	Merck, Milipore, Burlington (US)
Uvasol® 2-Methylbutane	Merck Millipore, Burlington (US)
VECTASTAIN® ABC Kit	Vector Laboratories, Burlingame (US)

Kits

PureYield™ Plasmid Maxiprep System	Promega, Madison (US)
PureYield™ Plasmid Miniprep System	Promega, Madison (US)
QIAquick® Gel Extraction Kit	Qiagen, Venlo (NL)
Wizard Genomic DNA Purification Kit	Promega, Madison (US)

Media, Supplements and Cell culture

2-Propanol for molecular use	AppliChem GmbH, Darmstadt (DE)
Accutase®	Sigma-Aldrich, Munich (DE)
Dimethylsulfoxide (DMSO)	AppliChem GmbH, Darmstadt (DE)
DMEM (1X) Dulbecco's Modified Eagle Medium	Gibco, Thermo Fisher Scientific, Waltham (US)
Heat inactivated fetal bovine serum (FBS)	Gibco, Thermo Fisher Scientific, Waltham (US)
Opti-MEM®(1x), Reduced Serum Media	Gibco, Thermo Fisher Scientific, Waltham (US)
Polyethylenimine (PEI) branched	Sigma-Aldrich, Munich (DE)
Poly-L-lysine hydrobromide (PLL)	Sigma-Aldrich, Munich (DE)
SuperFect® Transfection Reagent 1.2ml 3mg/ml	Qiagen, Venlo (NL)

2.1.2 Software

Table 3: Software

DESCRIPTION	SUPPLIER
Adobe Illustrator CS5	Adobe Systems Incorporated, San Jose (US)
Axiovision 4.9.1.0	Carl Zeiss Microscopy, Oberkochen (DE)
FlowJo® v10.0.7	FlowJo LLC, Ashland (US)
GraphPad Prism 5	GraphPad, La Jolla (US)
IBM SPSS 25 Statistics	IBM, Ehningen (DE)
Image Lab	Bio-Rad Laboratories GmbH, Munich (DE)
ImageJ Plugin: ImmunoRato1.0co	Wayne Rasband, national Institute of Health, Bethesda (US)
LightCycler®480 1.5	Idaho Technology Inc., Salt Lake City (US)
Mathlab 68	MathWorks, Natick (US)
NDP.view 2.7.25	Hamamatsu Phototonics
Paravision 5.0 MRI-imaging software	Bruker Biospin, Erlangen, (DE)
PMOD software	Pmod Technologies Ltd., Zurich (CH)

2.1.3 Consumables, Instruments and Appliances

Table 4: Consumables, instruments, and appliances

DESCRIPTION	SUPPLIER
Animal Work and IHC	
Bepanthen® Eye and nose ointment	Bayer Vital, Leverkusen (DE)
Bone Cutting Forceps	Fine Science Tools, Heidelberg (DE)
Coldlight source KL1500 LD	Leica Biosystems, Nussloch (DE)
Cordless Micro drill, 220V	Stoelting, Wood Dale (US)
Coverslips	R. Langenbrinck, Emmendingen (DE)

Disposable scalpel No.11	Pfm medical, Cologne (DE)
Hippocampel Spatula Tool	Fine Science Tools, Heidelberg (DE)
Hypodermic Needle Pro®, Needle with Needle Protection Device	Braun Melsungen AG, Melsungen (DE)
Injekt® 20ml Solo Syringe with Luer Cone	Braun Melsungen AG, Melsungen (DE)
Ismatec perfusion pump	Cole-Parmer, Wertheim (DE)
Malleus Bone Nippers	Fine Science Tools, Heidelberg (DE)
Manual Tissue Microarrayer MTA-1	Beecherinstruments Inc., Sun Prairie (US)
Med Comfort® PP-Visitor coat light green	AMPri, Winsen/Luhe (DE)
MoliNea®plus, Underpads	Hartmann, Heidenheim an der Brenz (DE)
Narrow Pattern Forceps	Fine Science Tools, Heidelberg (DE)
Quintessential Stereotaxic Injector	Stoelting, Wood Dale (US)
Russian Tissue Forceps	Fine Science Tools, Heidelberg (DE)
Sharp Fine Scissors Angled to Side	Fine Science Tools, Heidelberg (DE)
StainTry™ M920	Simport, Saint-Mathieu-de-Beloeil (CA)
Standard Earloop Face Mask	3M Germany, Neuss (DE)
Stereotactic Apparatus	Stoelting, Wood Dale (US)
SuperFrost®Plus Slide matt edge white	R. Langenbrinck, Emmendingen (DE)
TMA Parafinblock	Qiagen, Venlo (NL)
U-40 Insulin Syringe 1ml	BD Biosciences, Bedford (US)
Ventana BenchMark XT	Roche Diagnostics, Rotkreuz (CH)

General Laboratory Use

Aluminium foil	Carl Roth, Karlsruhe (DE)
Autoclave DX-65	Systec GmbH, Linden (DE)
Autoclave V-150	Systec GmbH, Linden (DE)

Bacterial incubator INFORS HT	Bottmingen/Basel (CH)
Bottles and flasks 100-600ml	Schott AG, Mainz (DE)
Cellstar® 15ml, 50ml tubes	Greiner Bio-one, Kremsmünster (A)
Cellstar® Cell Culture Flasks 25cm^2, 75cm^2, 150cm^2 and 1000 cm^2(4 layers)	Greiner Bio-one, Kremsmünster (A)
Chill 5 tube rack	Miltenyi Biotech GmBH, Bergisch Gladbach (DE)
Combitips advanced 0.1ml	Eppendorf, Mississauga (CA)
Costar® 2ml, 5ml, 10ml, 25ml, 50ml Stripette®	Corning Incoporated, Corning (US)
Cryo-babies© 1000 Pre-Cut Lables	Carl Roth, Karlsruhe (DE)
Descosept AF	Dr.Schuhmacher, Malchsfeld(DE)
Digital sight	Nikon Gmbh, Düsseldorf (DE)
Eclipse TS100 microscope	Nikon Gmbh, Düsseldorf (DE)
Eppendorf Easypipette	Eppendorf, Mississauga (CA)
Falcon Petri Dish 35x10mm	Corning Incoporated, Corning (US)
Filter tip 0.1-2.5µl, 2-200µl Biosphere®	Sarstedt, Nürnbrecht (DE)
Filtertip 0.5-10ml	Nerbe Plus, Winsen (DE)
Freezing Container	Thermo Fisher Scientific, Waltham (US)
Gel casting chamber	Neolab, Heidelberg (DE)
Gel tray	Neolab, Heidelberg (DE)
Hand piece counter "H 20"	Esska GmbH, Hamburg (DE)
Heraeus HeraSafe clean bench	Thermo Fisher Scientific, Waltham (US)
Incuwater-Clean™	AppliChem GmbH,Darmstadt (DE)
Kern ABJ balance	Kern, Balingen (DE)
Kern EMB 600-2 balance	Kern, Balingen (DE)
Light Cycler 480 qPCR machine	Roche Diagnostics, Rotkreuz (CH)
Liquid Blocker Super Pap Pen Mini	Daido Sangyo, Tokyo (JP)
MACs quant flow cytometer	Miltenyi Biotech GmBH, Bergisch Gladbach (DE)

Magnetic mixer IKA® RH basic 2	IKA, Staufen im Breisgau (DE)
Magnetic stir bar standard set	Neolab, Heidelberg (DE)
MicroAmp™ Fast 48-Well Reaction Plate (0.1ml)	Applied Biosystems, Foster City (US)
MicroAmp™ Fast 96-Well Reaction Plate (0.1ml)	Applied Biosystems, Foster city (US)
Nanodrop- 1000 Spectrophotometer	Thermo Fisher Scientific, Waltham (US)
Neubauer improved chamber for cell counting	Hecht-Assistant, Sondheim v.d. Rhön (DE)
Nitrile gloves, powder-free, M 7-8	Abena, Zörbig (DE)
OK. ® Microwave	Imtron GmbH, Ingoldstadt(DE)
Parafilm PM996	Cole-Parmer, Wertheim (DE)
Partion inserts, cardboard	Carl, Roth, Karlsruhe (DE)
Pasteur capillary pipettes 150mm	WU, Mainz (DE)
Peha-soft®nitrile GUARD, M 7-8	Hartmann, Heidenheim an der Brenz (DE)
Pipette Eppendorf research 0.1-2.5µl,0.5-10µl, 10-100µl, 20-200µl, 100-1000µl, 1-5ml	Eppendorf, Mississauga (US)
PowerEase 90W power supply	Life technologies, Thermo Fisher Scientific, Waltham (US)
PTC-200 Peltier Thermal cycler	MJ Research, Bio-Rad Laboratories GmbH, Munich (DE)
Sanyo CO_2 Incubator	Panasonic, Kadoma (JP)
Tabletop centrifuge, multifuge 1S-R Heraeus	Thermo Fisher Scientific, Waltham (US)
Thermomixer comfort heating block	Eppendorf, Mississauga (US)
Tubes 0.5ml, 1.5ml, 2ml	Sarstedt, Nürnbrecht (DE)
Vacuum pump VacuSafe	INTEGRA Biosciences GmbH, Biebertal (DE)

Vibramax 100	Heidolph Instruments GmbH&Co. KG, Schwabach (DE)
Vortexer	Phoenix instrument, Garbsen (DE)
Water bath 1083	GFL, Burgwedel (DE)

Imaging

Axioplan 2 Imaging System	Zeiss Microscopy, Oberkochen (DE)
Axiovert 200M	Zeiss Microscopy, Oberkochen (DE)
Bio-Rad ChemiDoc MP Imaging system	Bio-Rad Laboratories GmBh, Munich (DE)
Digital sight	Nikon Gmbh, Düsseldorf (DE)
Eclipse TS100 microscope	Nikon Gmbh, Düsseldorf (DE)
FET (0-(2-[^{18}F] Fluoroethyl)-L-tyrosine) PET Tracer	kindly provided by Werner Siemens Imaging Center, Department of Preclinical Imaging and Radiopharmacy, Eberhard Karls University of Tuebingen, Tuebingen, Germany
Graseby® Breathing pad	Smiths Medical, Minneapolis, (US)
Heating pad	Smiths Medical, Minneapolis (US)
Inveon small-animal PET scanner	Siemens Healthcare, Erlangen, Germany).
LSM 510 META	Zeiss Microscopy, Oberkochen (DE)
Mouse head 8 x 1 surface array coil	Bruker Biospin, Erlangen (DE)
MRI Biospec 7 Tesla	Bruker Biospin, Erlangen (DE)
MRI Radio-Gradient and Shimming Insert	Bruker Biospin, Erlangen (DE)
Nanozoomer® automated imaging scanner	Hamamatsu, Hamamatsu City (JP)

2.1.4 Buffers and Solutions

2.1.4.1 Buffers for Immunohistochemistry (IHC)

PBS-T

	1xPBS
0.1 % (v/v)	Tween 20

Co-Staining Permeabilization Buffer

	1xPBS-T
0.3 % (v/v)	Triton X-100

IHC Blocking Solution

	1x PBS-T
10% (v/v)	BSA

2.1.4.2 *In vivo* studies

Surgical Anaesthesia:

Fentanyl	(0,05 mg/kg KG)	
Midazolam	(5,00 mg/kg KG)	
Medetomidin	(0,50 mg/kg KG)	
Aqua	(0,10ml/10g KG)	Intraperitoneal Injection (IP)

Analgesic

Carprofen	(5,00ml/kg KG)	Subcutaneous Injection (SC)

Antidote

Atipamezol	(2,5 mg/kg KG)	
Flumazenil	(0,5 mg/kg KG)	
Naloxone	(10,0ml/kg KG)	SC Injection

Non-recovery anaesthesia

Ketamine	(120mg/kg KG)	
Xylazine	(10,0mg/kg KG)	IP Injection

2.1.5 Cell Culture Media

2.1.5.1 Cell culture media for maintenance, freezing and seeding

DMEM complete

For DF-1, HEK239 FT, HT1080 cells and glioma long-term cell lines (LN229, A171, GL261 and SMA560)

	DMEM
10% /v/v)	FBS
0.1% (v/v)	Gentamycin (50mg/ml)

Freezing media for all used cell lines

	FBS
10%(v/v)	DMSO
0.1%(v/v)	Gentamycin (50mg/ml)

2.1.5.2 Cell culture media for virus production

DMEM reduced

Serum- reduced media for HEK 239 FT

	DMEM
2%(v/v)	FBS
0.1%(v/v)	Gentamycin (50mg/ml)

Media for HEK 239 FT transfection

	OptiMEM
0.1% (v/v)	Gentamycin(50mg/ml)

2.1.6 Mouse Strains

Mouse strain	origin	International nomenclature	Supplier
VM/Dk **[109]**	wildtype	-	originally bought by Prof. Dr. Naumann (Hertie- Institut, Tuebingen /DE)
XFM**[102, 110]**	genetically modified	129S.Tg(NES-TVA)-Ink4a$^{-/-}$	kindly provided by Prof. Gronych, (DKFZ Heidelberg/ DE)

2.1.7 Cell Lines

Cell lines	Origin	Characteristics	Source
A-172**[111]**	human primary glioblastoma cell line	adherent cells	ATCC, Wesel (DE)
DF-1 **[112]**	chicken embryo fibroblasts cells	cultured at 39°C supports avian retroviruses replication	kindly provided by Prof. Gronych, (DKFZ Heidelberg/ DE)
GL261 **[113]**	chemical induced, mouse-derived glioma cell line	adherent cells	DMSZ, Wesel (DE)
HEK-293FT	human embryonic kidney	adherent cells	Thermo Fisher Scientific #R70007
HT 1080	human fibrosarcoma cell line	adherent cells	ATCC, Wesel (DE)
LN-229**[114]**	human glioblastoma long-term cell line	adherent cells	ATCC, Wesel (DE)

LNZ 308 **[115]**	human immortalized glioblastoma cell line	adherent cells	Kindly provided by Prof. Dr. Hegi (Centre Hospitalier Universitaire Vaudois,Lausanne /CH)
SMA 560 **[109]**	spontaneous murine mouse astrocytoma cell line	adherent cells	Kindly provided by Prof. Dr. Wick (Universitätsklinikum, Heidelberg/DE)

2.1.8 Bacteria and Viruses

2.1.8.1 Bacteria

E-coli Stem	***Usage***	***Company***
Stbl3	For transformation with plasmid-DNA	Invitrogen, Thermo Fisher Scientific, Waltham (US)

2.1.8.2 Viruses

Virus name	***Generation***	***Plasmids used for virus production***
PlJM1-CFP Lentivirus	3rd generation	PLJM1-CFP, pMDLg/pRRE, pMD2.G and pRSV-Rev
PlJM1-YFP Lentivirus	3rd generation	PLJM1-YFP, pMDLg/pRRE, pMD2.G and pRSV-Rev

2.1.9 Plasmidvectors

Vector	***Characteristics***	***Source***
pMDLg/pRRE	Lentiviral packaging plasmid containing Pol and Gag	Addgene (#12251) self-cultivated
pMD2.G	VSV-G envelope expressing plasmid	Addgene (#12259) self-cultivated
pRSV-Rev	Lentiviral packaging plasmid	Addgene (#12253) self-cultivated

Puc19	high copy transformation control plasmid with Lac promotor	Sigma-Aldrich, Munich (DE)
pcDNA3-CFP	Plasmid containing CFP	Addgene (#13030)
pLJM1-EGFP	Plasmid containing GFP	Addgene (#19319)
pSYFP-C1	Plasmid containing YFP	Addgene (#22878)
RCAS-PDGFB	Plasmid containing driver mutation PDGFB amplification	kindly provided by Prof. Gronych, (DKFZ Heidelberg/ DE)
RCAS-GFP	Plasmid containing GFP transfection control	kindly provided by Prof. Gronych, (DKFZ Heidelberg/ DE)

2.1.10 Antibodies

2.1.10.1 Primary Antibodies for IHC on mouse tissue

Antibody	***Identification***	***Dilution and fixation***	***Company***
Anti-CD11b	Rabbit monoclonal, IgG	1:100 on 4%PFA fixed tissue	Abcam #ab133357
Anti-CD163	Rabbit monoclonal, IgG	1:200 on 4%PFA fixed tissue	Abcam #ab182422
Anti-CD19	Rabbit monoclonal, IgG2a	1:100 on acetone fixed tissue	Abcam #ab25232
Anti-CD20	Rabbit polyclonal IgG	1:200 on 4%PFA fixed tissue	Thermo-Fisher #PA5-16701
Anti-CD204	Rat monoclonal, IgG2b	1:250 on 4%PFA fixed tissue	Thermo-Fisher #MA5-16492
Anti-CD3	Rabbit monoclonal, IgG	1:100 on acetone fixed tissue	Abcam #ab16669

Anti-CD31	Rat monoclonal, IgG2a	1:50 on acetone fixed tissue	BD-Biosciences #550274
Anti-CD4	Rabbit monoclonal, IgG	1:200 on acetone fixed tissue	Abcam #ab183685
Anti-CD45R (B220)	Rat monoclonal, IgG2a	1:200 on acetone fixed tissue	abcam #ab64100
Anti-CD8,	Rat monoclonal, IgG	1:80 on acetone fixed tissue	Abcam #ab22378
Anti-GFAP	Rabbit monoclonal	1:500 on 4%PFA fixed tissue	abcam #ab7260
Anti-Ki67	Rabbit monoclonal, IgG	1:400 on acetone fixed tissue	Abcam #ab16667
Anti-NCRI	Rabbit polyclonal, IgG	1:200 on 4%PFA fixed tissue	Abcam #ab214468
Anti-PD1	Rabbit polyclonal IgG	1:400 on 4%PFA fixed tissue	ProSic #4065
Anti-PD-L1	Rabbit polyclonal IgG	1:100 on 4%PFA fixed tissue	ProSic #4059
Iba1	Rabbit monoclonal IgG2a	1:1000 on 4%PFA fixed tissue	Wako #019-19741

2.1.10.2 Primary Antibodies for IHC in human tissue

Name	***Identification***	***Dilution***	***Company***
Anti-CSF1R clone 29	mouse monoclonal IgG	1:5000	Roche Diagnostics 25352

2.1.10.3 Secondary Antibodies for IHC in mouse tissue

Name	***Identification***	***Dilution***	***Company***
Anti- Rabbit 1,5mg/ml	goat biotinylated IgG	1:400	Vector/Linaris BA-1100

Anti-Rat 0,5mg/ml	goat biotinylated IgG	1:400	Vector/Linaris BA-9401
Anti-Mouse 1,5mg/ml	goat biotinylated IgG	1:400	Vector/Linaris BA-9200

2.1.10.4 Treatment Antibodies

Name	***Application volume***	***Company***
Anti-CSF1R clone 2G2 **[88]**	30mg/kg	kindly provided by Roche Diagnostics, Penzberg (DE)
MOPC-21 IgG1 Anti-CSF1R control	30mg/kg	Bio X Cell, West Lebanon (US)
C1.18.4 IgG2a Anti-PD1 control	10mg/kg	Bio X Cell, West Lebanon (US)
Anti-PD1 clone RPM1.14	10mg/kg	kindly provided by Roche Diagnostics, Penzberg(CH)

2.1.10.5 qPCR primers

Primer	***Concentration stock***	***Sequence***
ALB **[116]**	1µM	FP: GCGCCTTATCCGGTAACTATC RP: CTACATACCTCGCTCTGCTAATC
WPRE**[116]**	1µM	FP: GTCCTTTCCATGGCTGCTC RP: CCGAAGGGACGTAGCAGA

2.2 Methods

2.2.1 Cell Culture

2.2.1.1 Cell Splitting

The cell lines used in this study are listed in table 2.1.7. All the cell lines were cultured in Dulbecco's Modified Eagle's Medium (DMEM) complete (see 2.1.5.1) and maintained at 37 °C or 39 °C for DF-1 cells with 5 % CO_2 atmosphere. Cells were passaged, when they reached 70-80% confluence, the medium was discarded, and cells were washed with 1x Phosphate Buffer Saline (PBS) before addition of Accutase. Pre-warmed DMEM complete was added to the cell suspension to neutralise the Accutase. Suspension was then centrifuged at 1200 rpm for 5 minutes (min). The cell pellet was re-suspended in complete DMEM and an aliquot (1:8 – 1:20) was transferred to a fresh flask.

2.2.1.2 Cell Freezing

Accutase-detached cells were centrifuged at 1200 rpm for 5 min. The cell pellet was re-suspended in fresh cooled freezing medium comprising 5 % Dimethyl Sulfoxide (DMSO) in Fetal Bovine Serum (FBS) or 10 % DMSO in DMEM complete. The cells were aliquoted in cryogenic vials, then placed in a cryofreezing container lined with isopropanol and placed at -80 °C. The tubes with cells were transferred to -150 °C for long-term storage.

2.2.1.3 Cell Seeding

To determine the number of cells an improved Neubauer cell counting chamber was used. First, cells were twice washed with PBS, detached by Accutase and resuspended in 10 ml DMEM complete. 10 microliter (µl) of the suspension was mixed with 10 µl of 0.4 % trypan blue solution and pipetted carefully between the coverslip and the used chamber. Non-stained cells with intact cell membrane were count randomly in the four big squares of the chamber under 10x magnification of the microscope.

To calculate the cell density following formula was used:

$$cell\ density = \frac{counted\ number\ of\ cells}{number\ of\ squares} * dilution\ factor * 10^4$$

Needed volume of cell suspension is calculated from the earlier calculated cell density, which indicates cell number per ml, and the required cell number per flask. Calculated volume is added to the new flask and appropriate amount of DMEM complete was added.

2.2.1.4 DF-1 cell transfection

During the establishment process of the RCAS/TVA system, DF-1 cells were transfected with available RCAS/TVA plasmids.[101]

The day before transfection, DF-1 cells were plated 2.5x10^5 per T25 flask and cultured with DMEM complete containing 1% of non-essential amino acids at 39°C. Next day 2.5 µg of RCAS-PDGFB or RCAS-GFP plasmid were dissolved in 150 µl of DMEM without FBS and antibiotics. The solution was mixed and 25 µl of Superfect Transfection Reagent was added. The samples were incubated at room temperature (RT) for 7min. While the complex formation has taken place, the medium was removed from the flasks and the cells were washed once with PBS. 4ml of fresh DMEM complete was added to each flask. Next, 1ml of DMEM complete was added to the reaction tube, mixed and transferred to the T25 flask. Cells were incubated for 3 hours (h) at 39°C in DMEM complete including the transfection complexes. Transfected cells were washed twice with DMEM and cultured with DMEM complete.

Transfection was controlled by fluorescence microscopy beginning at day 5 post transfection measuring the GFP expression of the RCAS-GFAP plasmid. Control pictures of the GFP expression were taken with the colour camera of the Axiovert 200M imaging system. Photos were further processed with ImageJ.

2.2.2 Tissue Microarray (TMA)

2.2.2.1 Collective Description

Retrospectively used tissue samples were recruited within ethics proposal 077/2016BO2 which has been approved by the Ethics Committee of the

University of Tuebingen. Tissue samples belong to 72 patients with histologically confirmed $IDH_{wildtype}$ glioblastoma, WHO Grad IV glioma [1] and at least one tumour progression after chirurgical resection. The patients were treated with either Stupp-Protocol (radiotherapy and adjuvant temozolomide therapy after surgery) [10] or radiotherapy alone. Further inclusion criterium was appropriate amount of formalin-fixed, paraffin-embedded tissue for the microarray construction and representative Haematoxylin and Eosin (H&E) staining. During the construction process the included patient cases were checked for available tissue samples using the neuropathology internal diagnostic software. Available formalin-fixed, paraffinized tissue blocks and their matching H&E control staining were taken out of the internal tissue biobank. The representative tumour areas which showed clear characteristics of a glioblastoma, were marked on the H&E section and compared with the present tissue blocks. Next, the available and checked tissue blocks were applied on a grid format always using 2 cores from selected regions. Due to missing residual tissue the number of finally used tissue cores decreased to overall 128 cores from the cohort treated with Stupp-Protocol and 46 cores from the cohort treated with radiotherapy alone (see Figure 5).

After defining the punching pattern and its grid format, the TMA blocks were manually created with a manual tissue microarrayer. Therefore, an empty paraffin core was taken out of the acceptor block using repetitively a stylet with a diameter of 0.6 mm. Subsequently, a tissue core was taken out from the marked tumour area using a stylet and transferred to the acceptor block. Fixed 5 mm distances were kept between the single rows and tissue punches. After completion of the transfer process, the finished TMA blocks were heated up for 3min and the surface was pressed on by a glass plate. TMAs were left overnight on the bench for cooling down, next, control sections were cut and immunohistochemical stainings were conducted as shown in paragraph 2.2.2.2.

2.2.2.2 Tissue microarray staining

For evaluating changes of immunologic markers, IHCs were performed for CSF1R, CTLA-4, PD1, PD-L1 and CD204(MSR1). For the staining, a Ventana BenchMark® autostainer was used. The staining protocol and antibody for the

CSF1R staining were kindly provided by Roche diagnostics, Penzberg (DE).[88] CTLA-4 antibody was chosen, referring on Rahman et al.[117], PD1 and PD-L1 clones were used as in the routine laboratory of the clinical pathology and CD204 was chosen referring to Ek et al.[118] Antibody dilutions for antibody not provided by Roche diagnostics were established by trying different dilutions with and without amplifier on 12 sections of control tissue with a known high expression of the respective marker. For the CSF1R staining the control staining was performed on human tonsil tissue using the paracortex as reference tissue referring to the findings of Sereno et al.[119],PD1 and PD-L1 clones were tested on tonsil tissue, too.

Slides for CSF1R staining were processed by the autostainer starting with 20 min baking step, followed by several cell conditioning steps to improve antibody binding. Next, slides were treated with peroxidase inhibitor before the primary antibody (dilution see 2.1.10.2) was added, followed by 32 min incubation time. Next, slides were treated with H_20_2 and OV amplifier for better antibody signalling, followed by 8 min incubation time. Furthermore, OV AMP multimer was applied to sections and incubated for 12 min. Slides were counterstained with haematoxylin and incubated for 8 min. Finally, one drop of bluing reagent was added on slides and slides were incubated for 4 min.

Stained TMA sections were digitalized by using an automated imaging scanner exposure setting. From each stained core, 4 pictures (Tiff format) were acquired using the 20x magnification. Taken pictures were further processed and staining was quantified by using ImageJ and its included Plugin *Immunoratio* [120]. Plugin settings were kept the same, applied to pictures, and result pictures were saved. Acquired expression levels were ranked as measurement units: “Dab/nuclear area count” [%]. Additionally, absolute area counts were divided into four intervals: Next, an established immunoreactive score (IRS) was calculated.[121, 122] IRS consists of interval-based quantification scores (score 0-4, as outlined above) multiplied by semi-quantitatively raised intensity scores. Intensity scores were defined as 0 (absent staining), 1 (weak), 2 (moderate) and 3 (strong). Results were statistically processed by using SPSS 25.

2.2.3 Intracranial Tumour Cell Implantation

All animal experiments and included procedures are approved by the Institute of Animal Welfare and the Veterinary Office at the University of Tuebingen and the Regierungspraesidium Tübingen. Experiments of the VM/Dk strain using SMA560 cells ran under licence number N14/15. Experiment and animal numbers using the RCAS/TVA system in XFM mice were registered under animal licence number N8/15 for characterising the model and N6/18 for the treatment experiment.

Cells 80-90% confluent, were detached by using Accutase, counted, washed twice with PBS, centrifugated and resuspended in 2,5 or 2 µl PBS. To establish intracranial tumours in mice, a total of $5x10^4$ DF1/RCAS-PDGFB cells (2,5 µl) or $5x10^3$ SMA560 cells (2 µl) (see 2.1.5) were injected. The cells were kept on ice during the surgery.

Mice were anesthetized by IP injection of anaesthetic combined fentanyl, midazolam and medetomidine (see 2.1.3.2), then they received a single dose of carprofen SC. Eye ointment was applied to maintain adequate moisture during the surgery. A toe pinch for testing the intertidal reflex was used to confirm the mouse unconsciousness. Next, the head was shaved. Using a sterile scalpel, a 1 cm long sagittal incision was performed. The skull surface was exposed and cleaned. Bregma, intersection of the sutura coronalis and sagitalis serves as the 0 point for cell implantation, the drill was used to puncture the skull- 1,5-2 mm lateral and 1 mm anterior from the bregma. A Hamilton syringe was loaded with the desired number of suspended cells and placed with the help of a stereotactic frame in the created hole (3mm deep). The needle was left in place for 1 min. 1 µl of cell suspension per min was injected and the syringe was left inside the brain for 2 more min after injection. Afterwards the needle was removed. The skull hole was filled with bone wax and the scalp was closed with 3 to 4 single button stitches. Naloxone (see 2.1.4.2) as an antidote for fentanyl was injected subcutaneously.

Mice were monitored post-operatively and were kept on heating mats until they became ambulant and retained normal activity. Typically, the recovery time was around 15 min.

2.2.4 Animal Maintenance

Animals were monitored regularly during animal experiments. Inconspicuous animals were checked from day 2 post surgery every 48 h. Check-up consists of weighing and scoring of neurological abilities and general physiological conditions. If animals became conspicuous, they have been checked at least once per day.

Treatments were performed starting either 7 days post implantation (dpi) or 10dpi. First, body weight was checked, and body weight depended amount of antibody was injected with a 300µl syringe alternatingly in the lower right or left abdominal quadrant.

2.2.4.1 Scoring

Animal scoring were generally executed every second day. It consists of in Table 5 shown parameters, including measurement of bodyweight referring to Langford et al.[123] Scores and bodyweight were written down and were kept accessible for veterinarians and responsible animal care takers.

Table 5: Endpoints of animal experiment

Parameter	Phenotype	Score
Weight loss (A)	0 %	0
	10-14%	1
	maximum 15%	**2**
	maximum 20%	3
General appearance (B)	Clean skin and orifices, no pain	0
	Slight eye or nose discharge, slight pain	1
	Sticky eyes, moderate pain	**2**
	Cramps, dehydration, strong pain	3

Behaviour and posture (C)	Normal spontaneous-explorative behaviour, normal posture	0
	Reduced spontaneous-explorative behaviour, slightly hunched back	1
	Strongly reduced spontaneous-explorative behaviour, moderately hunched back	**2**
	Total inactivity, strongly hunched back	3
Neurological symptoms (Lose of balance and grid, paralysis of paws) (D)	None	0
	Slight loss-of-balance, occasionally missed steps, slight paralysis	1
	Moderate loss-of-balance, every third step missed, moderate paralysis	**2**
	Strong loss-of-balance, total inactivity, strong paralysis	3

In general, animals which reached either 3xScore 1+ 1x Score 2 or 2x Score 2 or a weight loss of 15%, were taken out of the running experiment and sacrificed.

2.2.4.2 Statistics

Survival experiments were statistically analysed by using primarily a Log-rank (Mantel-Cox) test for general significant symptom-free survival differences testing between different treatment groups. Next, the post hoc Tuckey-Kramer test referring to the recommendations of the biostatistical survey was used for examining singular significant symptom-free survival differences between experimental groups. Significance was defined as 5% significance level divided by the number of performed tests.

2.2.5 Animal Brain Perfusion

To investigate the immunological features of the induced and treated brain tumours in the used mouse strains, the animals were perfused [124], and the mouse brains were collected afterwards.

First, the animal was anesthetized with a single IP injection of saline, containing ketamine and sedaxylan (see 2.1.4.2). Afterwards the mouse was put back in the cage. Neuronal intertidal reflex response was checked with forceps. After no response, a 5-6 cm lateral incision through the integument and abdominal wall just beneath the rib cage was performed. The liver was carefully separated from the diaphragm and the ligamentum teres hepatis was cut. A small incision into the diaphragm was made using the curved, blunt scissors. The diaphragm incision was continued along the entire length of the rib cage to expose the pleural cavity. A perfusion needle connected to a syringe was passed through the heart apex into the left ventricle, then the animal was perfused with cold PBS for 3 min. When the liver turned white due to the perfusion by PBS the aorta abdominalis and the vena cava inferior were cut.

2.2.6 Brain Preparation and Freezing

The head was removed from the dead animal with a malleus none nippers, then the scalp was opened with sharp fine scissors over the sagittal sutura, folded to the side, exposing the skull bone and the transition from medulla oblongata to spinal cord. The os frontale was broken through with a bone cutting forceps. Next, the skull bone was pierced along the sutura sagittalis beginning by the medulla oblongata with side-angled scissors. The halves of the skull now laid loosely on the brain, they were lifted with a narrow pattern forceps from the skull and luxated to the side. Finally, the exposed brain was lifted from the bone with a hippocampal spatula and was snapped frozen in Methyl-Butane on dry ice for 5 min. Snapped frozen brains were removed with a Russian Tissue Forceps. The snapped frozen brains were then embedded in TissueTec® and stored at -80°C.

2.2.7 MRI and PET Imaging

To examine tumour development in the RCAS/TVA model, MRI and Positron-emission tomography (PET) measurements were performed (see 3.3.1).

2.2.7.1 MRI Measurements

To perform the measurements, mice were anesthetized with a mixture of Isoflurane (2 %) vaporized in normal air. After initial application of Isoflurane, a catheter was placed in the tail vein of the mice and fixed with glue. Isoflurane was reduced to 1.5 % during measurements. Their body temperature was maintained at 37±0.5°C by using a heating pad. Breathing was controlled by a breathing pad which measured breath excursion and respiratory frequency. MRI measurements were performed with a 7 Tesla MRI Biospec®, using the Paravision 5.0 imaging software. Imaging quality was improved by a radio insert for better shimming and a head surface array coil for mice. As shown in Figure 4 mice were placed on a modified MRI animal bed.

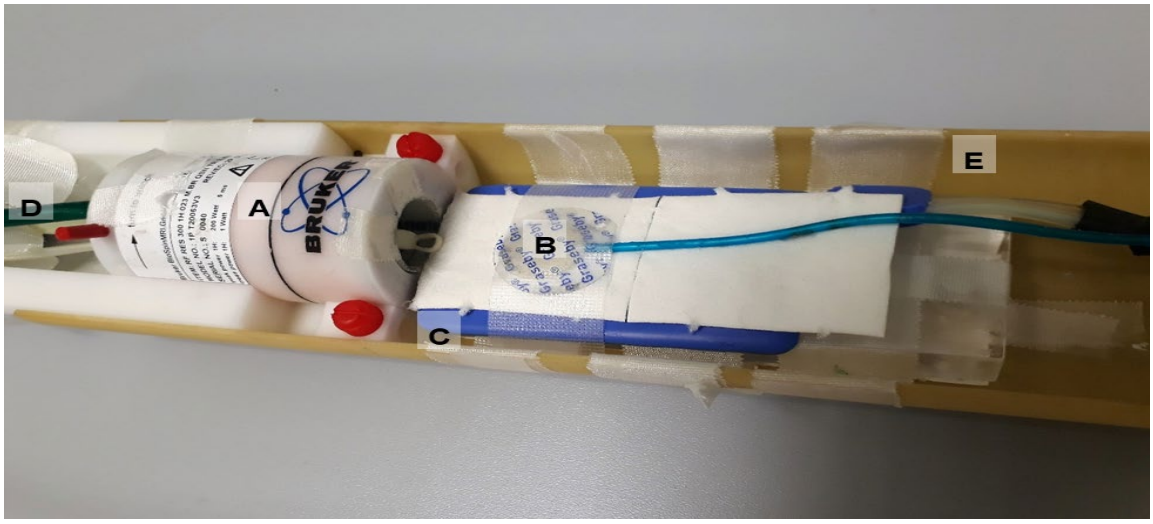

Figure 4: MRI measurement setup
A: Head surface array coil for mice, B: Breathing pad, C: Water based Heating Pad, D: Connection to Isoflurane source, E: Animal MRI bed

The brain of measured mouse was first placed in the centre of the field of view (FOV) by performing a localizer sequence. A shimming protocol was acquired to calibrate possible field inhomogeneities and improve image quality for the Echo-Planar Imaging (EPI) acquisitions. As described in Table 6: Technical Information about executed MRI sequences, different sequences were performed.

Table 6: Technical Information about executed MRI sequences

Sequence name	Characteristics	Repetition time (TR) [ms]	Echo time (ET) [ms]	Slice thickness (ST) [mm]	Field of view (FOV) [mm]
Localizer	Establishing of FOV	40	2	1	50x50
Shimming	Calibration for EPI sequence	2500	3	58	58x58
T2_TurboRARE trans	brain anatomy sequence transversal	2500.4	11	0.2	25.6x25.6
T2_TurboRARE	brain anatomy	2500	11	0.7	20x20
DTI[2]_EPI_seg_30dir _2Seg_2Avg_ 8Bvalues_Insert	Diffusion sequence for BBB[3] disorders	703.2	0.72	0.2	24x24
T1_Flash before application of Gadolinium	3 sequences with different number of flip angles [2,9,27]	10	1.347	7.98	25.74x25.74
DCE[4]_Flash	Measurement of T1 changes after Gadolinium injection	30	1	1	24x30
T1_Flash after Gadolinium application	3 sequences with different number of flip angles [2,9,27]	10	1.347	7.98	25.74x25.74

Furthermore, contrast-enhancing sequences were performed by using 0.1 ml per kg bodyweight of Gadolinium as a contrast agent. Therefore, 4 units of gadolinium dissolved in sodium chloride (NaCl) were injected through the placed catheter. 56sec after injection T1-weighted sequences were started and measured

[2] Diffusion Tensor Imaging
[3] Blood-Brain-Barrier
[4] Dynamic Contrast Enhanced

possible contrast agent uptake in mice brain. After finalization of the imaging measurement, animals were disconnected from the isoflurane source and monitored till they regained consciousness and became ambulant.

2.2.7.2 MRI Image Analysis

MRI row data were clustered with MATLAB. Next, clustered sequences and its calculated T1 and B0 maps were co-registered by using the PMOD software. Therefore, anatomical MRI brain templates were used to co-register the acquired MRI data and to allow a consistent co-alignment of all used sequences.

To determine the tumour volume for each time point, Region of Interest (ROI) was manually drawn around contrast enhancing tumour areas in the co-registered *T1_flash 27a Post C* sequences. Whole brain volume was estimated by manually drawn VOIs, too. Drawn ROIs were exported from the PMOD software and further processed by using GraphPad Prism 5 and Excel.

2.2.7.3 PET Measurements

In the same session after MRI, a dosage of roughly 11 Megabecquerel (mBq) of 0-(2-[^{18}F] Fluoroethyl)-L-tyrosine (FET), a radiolabelled amino acid analogue[125, 126], was injected into the animals intravenously. PET sequence consisted of a 45min emission and 15min transmission acquisition using a ^{57}Co source.[127].

As described for MRI (see 2.2.7.1), PET Data were clustered with MATLAB, co-registered with the PMOD software, matched to acquired MRI-data and further processed by our cooperation partner of the Werner Siemens Imaging Centre.

2.2.8 H&E Staining

The cut fresh-frozen tissue sections were removed from the -80°C freezer and were left on the bench for 10 min. The sections were fixed in cold acetone and ethanol for 10 min and washed two times for 5 min in PBS.
The slices were incubated in haematoxylin for 10min under the hood.

They were washed under running tap water for 5min. Then, they were tipped in 0.5% Eosin for 2 min. Afterwards the slides were washed under running tap waters for 2 min. Next, slides were dehydrated by an alcohol gradient beginning with 10 min in 70% ethanol, followed by 30 sec in 90% ethanol, 60 sec in 100%

ethanol and three times in xylene for 5 min. The sections were mounted with Coverquick mounting medium and coverslips. Slides were left overnight under the hood to dry.

2.2.9 Immunohistochemistry (IHC) Staining

First, the cut sections were removed from the -20°C freezer and were left on the bench for 10 min. Depending on the used primary antibody the samples were either fixed in cold acetone followed by ethanol for 10 min each or with 4% Paraformaldehyde (PFA) for 15 min. The sections were washed in PBS for two times 5 min. Next, the endogenous peroxidase, pseudoperoxidase and alkaline phosphatase of the sections were inactivated by the incubation in BLOXALL™ solution for 10min. Again, sections were washed with PBS for 5 min. Afterwards the sections are blocked for 60 min with 10% BSA diluted in PBS-Tween 0.3% Next, the respective primary antibody in the tested dilution (see 2.1.10.1) was diluted in 2% BSA in PBS-Tween 0.06% and was put on the sections for 48 h at 5°C.

48 h afterwards the sections were washed three times for 5 min in PBS. Depending on the primary antibody used, the appropriate biotinylated secondary antibody has been diluted in 2% BSA PBS-Tween 0.05% at room temperature and was put on the slides (see 2.1.10.3). During the incubation time the Vectastatin Elite ABC Reagent which acts as a signal amplifier of the secondary antibody, had to be prepared by adding 2 drops of reagent A and B to 5 ml of PBS containing 0.1%Tween 20, were immediately mixed and left on the bench for 30min before use. The slides were washed four times for 5 min with PBS. Then the ABC reagent was put on the slides for 30 min at room temperature, washed again for 5 min in PBS subsequently. Then the slides were treated with a peroxidase substrate, in this case the Vector Nova Red, for 5 min at room temperature which has been prepared before by adding 3 drops of reagent 1, 2 drops of reagent 2, 2 drops of reagent 3 and 2 drops of hydrogen peroxidase solution to 5 ml of dH_20. Subsequently, the slides were washed for 2 min with distilled water which stops the reaction between the amplifier and peroxidase substrate.

Finally, the slides were incubated with haematoxylin for 45 sec at room

temperature and washed under running tap water for 2 min. Next, the slides were dehydrated by an alcohol ladder beginning with 2 min in 70% ethanol, followed by 2 min in 90% ethanol, two times 2 min in 100% ethanol and three times in xylene for 5 min. The sections were mounted with Coverquick mounting medium and coverslips and are left overnight under the hood to dry.

2.2.10 IHC Co-Staining

As earlier described slides were warmed up, fixed with PFA and washed (see 2.2.9). Fluorescent slides were permeabilized with PBS-T (see 2.1.4.1) for 5min and were washed 3 times with PBS for 5 min. Next, slides were blocked with 10% BSA diluted in PBS-T for 60 min at room temperature. Slides were incubated overnight at 4°C with primary antibody (see 2.1.10.1) diluted in 1% BSA PBS-T. Sections were washed 3 times in PBS for 5 min and were incubated with fluorescent or not fluorescent secondary antibody (see 2.1.10.2+3) for 60 min at room temperature. For non-fluorescent co- staining, slides were processed as mentioned in 2.2.9 without counterstaining with haematoxylin. Both fluorescent and non-fluorescent staining were again permeabilized with PBS-T/ washed with PBS. Nonfluorescent samples were blocked with 10% goat serum diluted in PBS 0.3% Tween 20, whereas fluorescent samples were again blocked with 10%.BSA PBS-T. Next, second primary antibody diluted in 1% goat serum/BSA PBS-T was put on the slides for 24 h at 4°C. Slides were washed again with PBS and secondary antibodies diluted in 1% goat serum/BSA PBS-T was put on slides for 60 min. Non-fluorescent samples were further processed as mentioned in 2.2.9. Fluorescent samples were washed with PBS and were fixed again with 4% PFA in PBS-T washed again in PBS and mounted with fluorescent specific mounting medium. All slides were left light protected under the hood for drying.

2.2.11 IHC Analysis and Quantification

All stained tissue samples were analysed with an Axiovert Zeiss microscope. Pictures were taken by connected microscope camera with fix exposure settings. All pictures were saved in TIFF-format and further processed with ImageJ.

Counting was performed with a threshold-based Image J script. Therefore, taken pictures with 10x magnification were background corrected and

colours separated. Pictures were further split by the red-green-blue-violet system (RGB). Stabile threshold limits (0-180) were set to detect positive-stained cells. Generated pictures were further converted to binary data pictures. Positive cells were automatically counted depended on their size, using stable size frames based on manually performed calibration measurements of cell sections. Counts were measured as counts per picture and counts per positive stained area of the picture.

Raw results were statistically analysed with SPSS 25 and GraphPad Prism 5. One-way ANOVA test followed by Tukey's multiple comparison test was used.

2.2.12 Plasmid Development and Production

Labelling of glioma long-term cell lines for further studies was performed with plasmids containing CFP and YFP. Plasmids were cloned and modified.

2.2.12.1 Restriction Digestion

The required backbone and the insert were firstly isolated from their plasmids. 20µl reaction mixes contained:

2 µl	CutSmart Buffer
1,5 µl	restriction enzyme I (used enzymes see 2.1.1)
1,5 µl	restriction enzyme II
2-4 µg	plasmid
13-15 µl	nuclease-free water

Next, samples were incubated for 1 h at 37°C. Next, 1 µl of alkaline phosphatase was added and incubated at 30 min at 37°C. The restriction enzymes were inactivated with a heat shock of 65°C for 5 min. Correct cleavage was controlled by gel electrophoresis. Therefore, 24 µl of digested DNA was mixed with 4 µl of loading dye and were separated on a 1 % agarose gel for 20 min at 500 mA. Possible contamination was controlled by a water control. For estimation of fragment size 1kilobase (kb) DNA ladder was used and visualized with a ChemiDoc® imaging system.

Bands of the correct size for backbone or insert were then cut out of the gel under UV-light. DNA was extracted out of gel pieces with the *Qiagen Gel Extraction kit*. The gel pieces were weighed. According to its weight same amount of QG buffer

was added, vortexed every 2 to 3 min and was incubated for 10 min at 50°C. 1 volume proportion of Iso-Propanol was added, the solution was centrifuged for 1 min in a *QIAquick* spin column. The gained filtrate was discarded and the DNA on top of the filter was eluted by adding 30 µl of elution buffer. Spinning tubes were incubated for 1 min and centrifuged for 1 min. Gained filtrate contained extracted DNA. DNA amount and its purity were measured in ng/µl by using UV-Vis spectrophotometer.

2.2.12.2 Phosphorylation and Annealing of Oligos

For production of CFP containing plasmids we had to adjust backbone sticky ends to vector sticky ends by annealing of oligos.

Therefore, following reaction mix with a volume of 50 µl was used:

1 µl	forward primer
1 µl	reverse primer
5 µl	T4 ligase buffer (10 times)
43 µl	nuclease-free water

Reaction mix was incubated for 10 min at 85°C and cooled down at room temperature for 60 min.

2.2.12.3 Ligation

Amplified oligos/ inserts were connected to the used vector backbone in a ratio of 1:20 and 1:40.

Following reaction with a volume of 20 µl mix was used:

3 µl	vector/backbone
3 µl/ 6 µl	oligos/ insert (1:20 /1:40)
2 µl	Quick ligase Buffer (2 times)
1 µl	Quick ligase
11 µl/ 8 µl	nuclease-free water

Control consisted of same mix without insert. All samples were incubated for 1h at room temperature, followed by incubation on ice for 20 min. All samples were checked with control digestion followed by gel electrophoresis.

2.2.12.4 Transformation

For the amplification of packaging and fluorescence labelled plasmids, up to 100 ng of respective plasmid was added to 25 µl bacterial competent cells and incubated on ice. Next, cell plasmid mixture was heat-shocked at 42°C for 45 sec and afterwards incubated on ice for 2 min. 150 µl of prewarmed SOC media was added to bacterial culture and then incubated on a shaker for 1 h at 37°C. For selection of positive transformants, 80 µl and 100 µl of the transformed bacterial culture was spread by quadrant streak method on a pre-warmed LB-agar plate containing 100 µg/ml ampicillin and incubated overnight at 37°C. As a transformation control, we used the pUC19 plasmid in a ratio of 1µl plasmid to 25 µl of bacterial competent cells.

Colony forming agar plates were selected and further expanded. For this, one colony was picked and was incubated in 3 ml to 500 ml LB medium overnight. *Qiagen Plasmid Mini Kit* for self-modified plasmids and the Maxi kit for packaging plasmids were used for plasmid isolation and plasmid DNA purification of packaging and vector plasmids.

500 ml of checked transformants bacterial culture in LB medium were incubated by 37°C overnight. In the next morning, they were centrifuged at 3500 g for 25 min and 4°C. Next, cell pellet was thoroughly resuspended by the supplied precipitation buffer which starts the alkaline based cell lysis process. Solution was mixed with the supplied lysis buffer and was shaken heavily till blue colour reaction occurred. Mixture was incubated 5 min at room temperature. 10 ml of prewarmed neutralization buffer was added, was shaken heavily till colourless colour occurred and was incubated on ice for 20min. Cell debris were spun down with 3500 g for 10 min. The supernatant was filtered through a silica gel-based filter which bind the DNA. The bound DNA was washed twice with 20 ml of supplied QC buffer. The washed DNA was then eluted with 15 ml of supplied QF buffer. By mixing with 10,5 ml of isopropanol DNA was precipitated and centrifuged for 30 min. Spun down pellet was washed with 5 ml ethanol 70%, supernatant was discarded. Next, the pellet was again centrifuged for 10min and then air dried for 40 min after carefully discarding the supernatant. Air-dried pellet was carefully dissolved in TE-buffer and was left overnight in the fridge. Finally,

DNA content and its purity in ng/µL was determined by UV-Vis spectrophotometer.

After DNA isolation of modified plasmids, expanded number of plasmids were checked by control digestion (see 2.1.9), followed by gel electrophoresis.

2.2.13 Lentivirus Production

2.2.13.1 Virus Production

Lentiviruses containing CFP or YFP were produced by transfecting HEK-293 FT cells with packing plasmids (see 2.1.9) and cloned plasmids (see 2.2.12). Therefore,$1.5x10^6$ HEK 293 FT cells were seeded in T-175 flasks, in total 12 flasks, till they have gained 80-90% confluence. Cells were transfected 3 days post seeding in Opti-MEM using Polyethylenimine (PEI) reagent after 20 min incubation in room temperature. Cells were incubated for 4 h in transfection mixtures at 37°C with 5% CO_2. Medium was removed after 4 h and DMEM complete was added. Transfected cells were cultured for 96 h. Medium containing virus was harvested after 72 h and 96 h and was stored at 4°C. Collected medium was centrifuged at 4000 rpm for 10 min and then filtered through a 0.22 µm filter. Filtered medium was transferred to centrifuge tubes and ultra-centrifuged at 4°C, for 2 h at 23000 rpm. The supernatant was carefully decanted and 30 µl of DMEM was added to each tube and pipetted three times up and down. Tubes were covered with parafilm and incubated on ice for 1 h. Virus pellets were resuspended in early applied medium and stored as 30 µl aliquots in cryovials at -80°C.

For virus titre determination respective 10^5 HT-1080 cells were transduced with 1 µl, 2 µl and 4 µl of the concentrated virus on a 12 well plate.

On day 1, cells were seeded. 24 h later, cells were transfected and the cell number of one well was counted for later titre calculations. The 12-well plate was incubated for 96 h. After incubation time, medium was removed, cells were washed, carefully detached and washed again.

Next, the Genomic DNA was isolated by using *Wizard® Genomic DNA Purification Kit* (see 2.1.1). Therefore, 600 µl of Nuclei Lysis Solution were added, mixed well and were incubated for 30 min at 37°C followed by cooling down at

room temperature for 5 min. 200 µl of protein precipitation solution was added, vortexed for 20 sec and incubated on ice for 5 min. Samples were centrifuged for 4 min at 13000 rpm. Next, supernatant containing DNA was carefully removed and transferred to an Eppendorf tube. 600 µl of Isopropanol was added, mixed till a white DNA strand was visible and was spun down for 1min at 13000 rpm. The supernatant was removed, and DNA pellet was washed with adding 600 µl of 70% ethanol. The pellet was spun down again for 1 min at 13000rpm, supernatant was discarded, pellet was air-dried for 30 min. The air-dried pellet was rehydrated in 70 µl of DNA rehydration solution and was stored overnight at 4°C.

Amount of purified DNA and its purity was measured in ng/µl by using UV-Vis spectrophotometer. Measured DNA was adjusted to 5 ng/µl and was stored at -20°C.

2.2.13.2 Real-time quantitative PCR (qPCR)

Real-time quantitative PCR (qPCR) was performed by using ALB and WPRE primers to evaluate virus copy number and its titre. Every reaction mix had volume of 10 µl containing:

5 µl Sybr Green,
0.5 µl reverse primer (at a concentration of 5µM)
0.5 µl forward primer (at a concentration of 5µM)
4 µl DNA (20ng DNA per well)

Pipetting schema showed in Table 7 was used:

Table 7: 96 well-plate design for Virus titre evaluation

	1	2	3	4	5	6	7	8	9	10	11	12
A	Alb			Alb			Alb			Alb		
B	Alb			Alb			Alb			Alb		
C	Alb			Alb			Alb			Alb		
D	Virus				Water		empty wells			empty wells		
E	WPRE			WPRE			WPRE			WPRE		
F	WPRE			WPRE			WPRE			WPRE		
G	WPRE			WPRE			Virus			Virus		
H	Virus				Water		empty wells			empty wells		

In Table 8 showed qPCR protocol was used (LightCycler®):

Table 8: qPCR protocol for Virus titre evaluation

Step	Temperature [°C]	Acquisition Mode	Time	Ramp Rate (°C/sec)	Cycles
Pre-incubation	95	None	5 min	4.4	1
Amplification	95	None	10 sec	4.4	45x
	62	None	10 sec	2.2	
	72	Single	10 sec	4.4	
Melting Curves	95	None	5 sec	4.4	1
	65	None	1 min	2.2	1
	97	Continuous		0.11	1
Cooling	40	None	30 sec	2.2	1

qPCR results were evaluated by using the Light Cycler software.

To calculate the vector copy number:

$$Vector\ Copy\ number = \frac{mean\ concentration\ of\ WPRE}{mean\ concentration\ of\ Alb}\ x\ 2$$

Titre calculation was performed:

$$Titre\ \left(\frac{TU}{ml}\right) = \frac{Number\ of\ target\ cells\ seeded\ (\ day\ 2) x\ vector\ copy\ number}{Volume\ of\ Virus\ added\ (ml)}$$

2.2.13.3 Generation of stable transduced cells

The cell lines were plated 10^5 per well in a 12 well plate. The next day (50-70% confluence) the medium was removed.

MOI 50 (multiplicity of infection) was used:

$$MOI = \frac{50x\ cellnumber}{Virus\ titre}$$

12 well plates containing virus were incubated for 96 h. Three-days after transduction, cells were moved to 6 well plates, and incubated with DMEM medium containing 1 µl/ml of puromycin. Parental non-transduced cells were used as a control. The medium was replaced with fresh medium containing 1µl/ml of puromycin every 2 days for two weeks. Positive cells were expanded, frozen and kept at -80°C.

2.2.13.4 FACS as labelling control

Transfected cells were checked by fluorescence-activated cell sorting (FACS) using the MACs quant flow cytometer. 10^6 cells were resuspended in PBS and 1000 cells were analysed. Gating was performed manually, YFP labelled cells were detected via the fluorescein isothiocyanate (FITC) channel, CFP labelled cells were detected via the Vio® Blue channel. Acquired data were processed with FlowJO® 10.

3 Results

3.1 CSF1R expression in matched pair human tissue samples

3.1.1 Patient derived samples reveal high-grade glioma specific histologic features in H&E Staining

As described in 2.2.2 we investigated presence of CSF1R in matched pair human tissue samples of diagnosed $IDH_{wildtype}$ glioblastoma, WHO Grad IV, using tissue microarrays (TMA).[108]

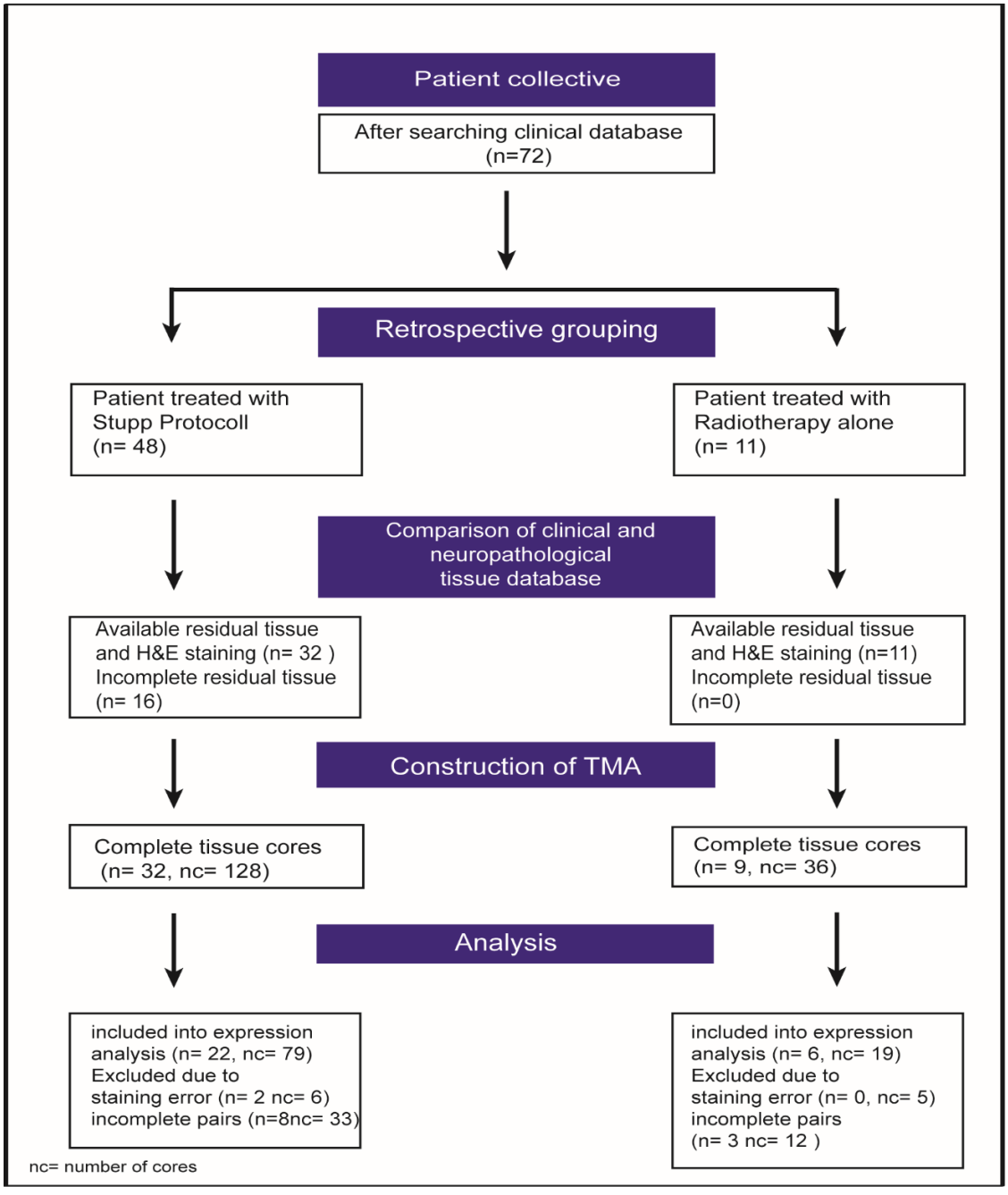

Figure 5: Flowchart of human tissue samples acquisition

The used tissue samples were grouped according to their therapy regimes, either Stupp-protocol or radiotherapy alone.[108]
As illustrated in Figure 5 the number of included tissue samples shows a decrease during TMA construction from overall 72 to 22 pairs treated with Stupp protocol and 6 pairs treated with radiotherapy alone which have been included into final analysis. Mainly, samples were excluded due to missing residual tissue. 13 pairs dropped out during punching process. Other reason for exclusion were processing errors (n=2), insufficient image quality or staining background which was rarely seen. [108]

Besides IHC staining for CSF1R, H&E staining of the constructed TMA were performed. As shown in Figure 6, representative areas of primary tumour samples and after first progression samples showed comparable histological features. First, high grade of neo vascularisation (examples marked with red circles in Figure 6), represented by high neoplastic vessel density and its abnormal configuration could be observed. Moreover, samples showed high density of small strongly haematoxylin/ basophilic stained tumour cells in primary and recurrent tissue (Figure 6A2b and B1b). Cells had polymorphic configuration of nuclei and a wide range of cell and nuclei size (see Figure 6 green circles). Next, increased number of mitotic figures could be observed (black arrows Figure 6). Another visible key feature were necrotic regions, highlighted by black stars in Figure 6. Described histological features were consistently found in both tissue types, primary and recurrent tumour samples, as well as in both treatment groups as visible in Figure 6.

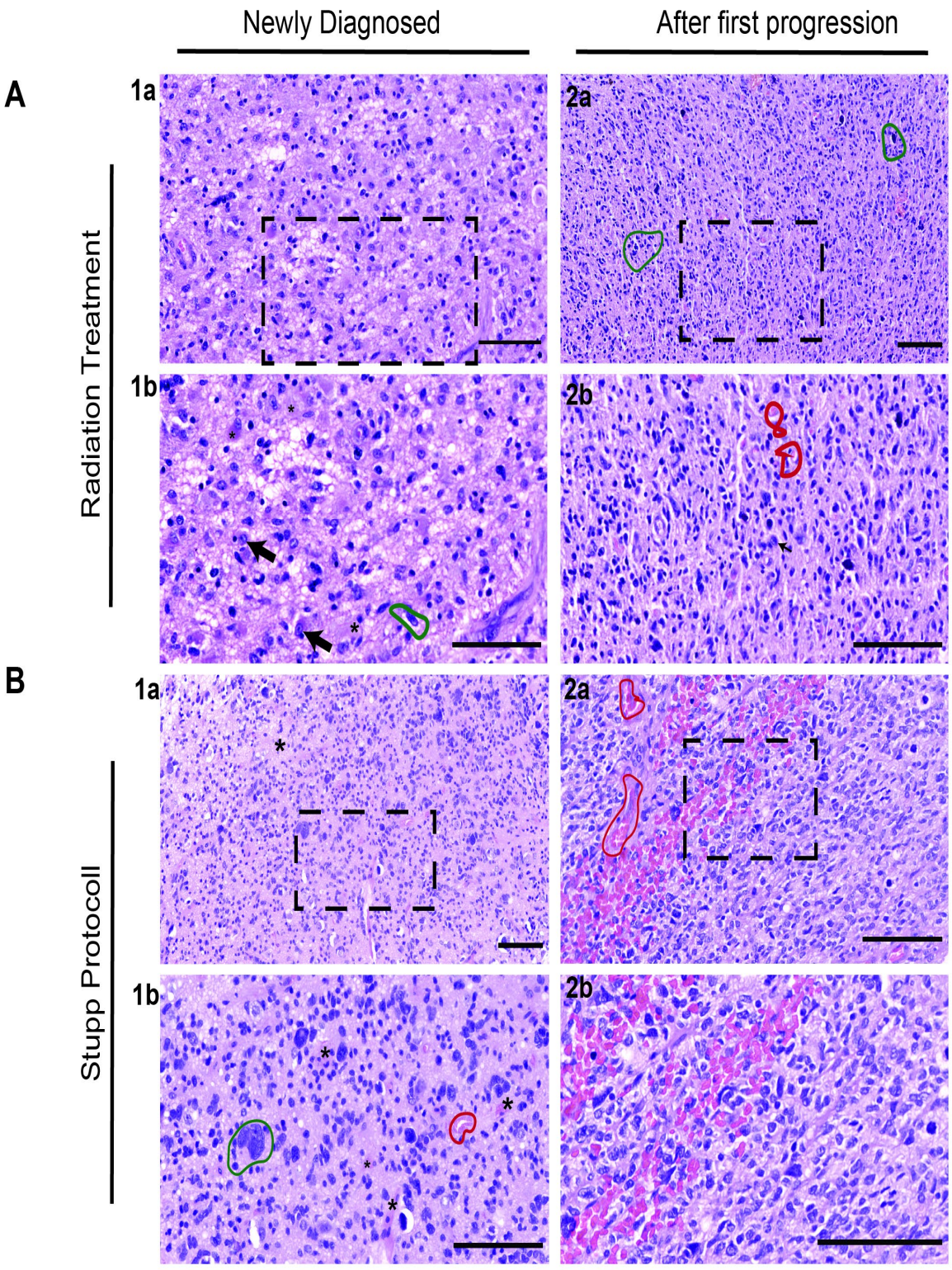

Figure 6: H&E staining of TMA.
Figure shows representative areas of 2 matched tissue pairs which either received radiation (A) or the Stupp protocol (B). Dotted frames depict the magnified area shown below. Red circles highlight some vessels, green circles polymorphic cellular configuration. Black stars highlight necrotic areas, black arrows indicate mitotic figures.
Pictures were either taken with 20x (1st and 3rd row) or 40x (2nd and 4th row) magnification. Scalebars 100 µm.

To evaluate the specificity and characteristics of the anti-CSF1R antibody, human tonsil lymphatic tissue samples were primarily stained with the antibody. High CSF1R expression on macrophages is well described in healthy human tonsil tissue in a study published by Moreno et al. Consequently, human tonsil tissue serves as a reference tissue for the later described CSF1R staining.

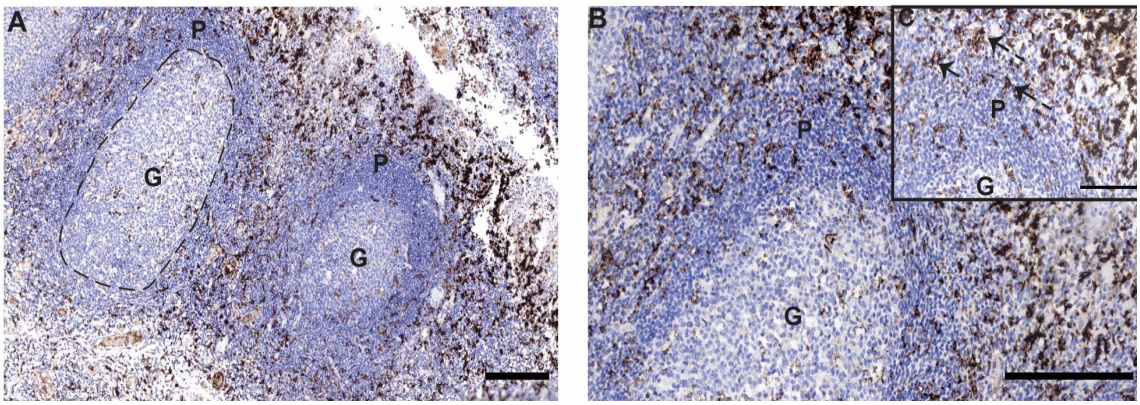

Figure 7: Representative CSF1R staining of human control lymphatic tonsil tissue.
Dotted circle in (A) represents germinal centre (G), adjacent the paracortex (P) is visible.
Black arrows in 7C highlight representative stained polymorphic convoluted cells.
Picture were taken with 10x(A) 20x(B) and 40x(C) magnification. Scale bars 100 µm(A+B)/ 50 µm.

As it is visible in Figure 7A-C, strong staining signals were mostly detected in the paracortical area of lymphatic tonsil tissue. Weaker signal was detected in the germinal centre of lymph nodes (see Figure 7A-B). Stained cells often showed polymorphic convoluted cytoplasmic margin and strong homogeneous, sharply defined DAB staining (see arrows in Figure 7C). Overall, stained cells showed high staining intensity. Not-stained cells showed consistently basophilic counter staining, cells of paracortex showed higher haematoxylin staining as cells of the germinal lymph node centre. These findings are consistent to the earlier mentioned publication of Moreno et al.[119]

As a next step, described tissue collection of glioblastoma matched pairs were stained with tested CSF1R antibody and compared resulting staining with previously stained control tissue (see 2.2.2.2). Stained tissue samples showed heterogeneous staining both tissue cores with strong, weak and absent staining signal were detected on all stained TMA blocks with its tissue cores. Overall, single stained cells showed similarity characteristics as in the control tissue. Interestingly, earlier described polymorphic convoluted cytoplasmic margin of

stained cells were less observed in tissue cores with very strong staining signals. Instead, more extensive, merging Dab-signal covered single tissue cores. In general, described staining signals showed high intensity. Representative merging Dab is shown in Figure 11. Unspecific staining signals were sometimes detected inside and around brain vessels, therefore respective areas were excluded from Dab signal quantification.

3.1.2 CSF1R Staining quantification shows presence of CSF1R in primary and recurrent tissue samples

For evaluating potential expression differences between primary and recurrent tissue samples or possible treatment dependent expression changes, CSF1R staining signals were quantified, as described in 2.2.2.2.

First, acquired CSF1R expression levels were validated concerning normal distribution. As shown in the value distribution histogram in Figure 8, samples were not normally distributed.

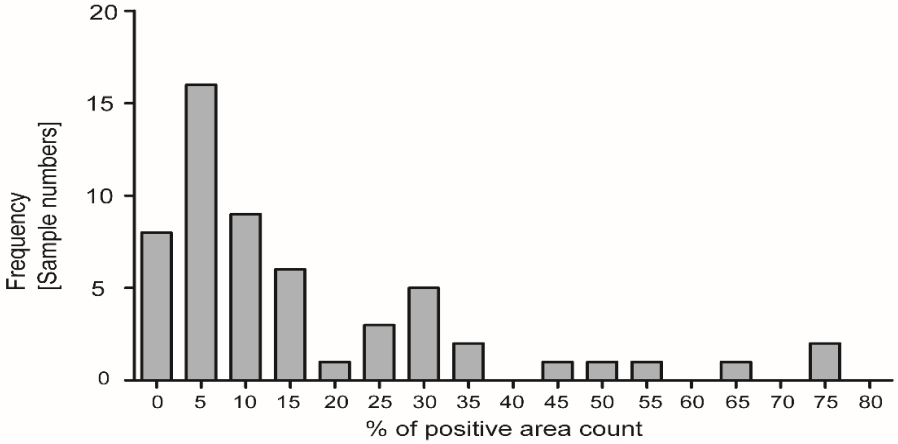

Figure 8: CSF1R value frequency and distribution of all included samples.
Samples of 56 tumours not clustered after tumour type or received treatment modality are shown. Median: 9,11 %, Mean: 16 ,28%, Minimum:0 %, Maximum: 75,875 %. D'Agostino's K-squared test for normal distribution ($p_{prim.}$ value: 0,0133; $p_{recurr.}$ value: 0,0111); significantly not normally distributed.

The general statistical values, which are illustrated in Figure 9A showed consistent expression of CSF1R in evaluated tissue subsets. Overall, mean CSF1R expression was 16,28%, median was 9,11% positive stained cell area count. Most samples showed different expression patterns of CSF1R which is illustrated by a minority of samples which showed no expression (see Figure 8)

and samples which showed maximum expression of over 65% positive stained cell area count (see histogram Figure 8).[108]

Tissue based analysis showed higher mean value of 18.98% positive stained cell area count in primary tissue than 14.10% in recurrent tissue samples (Median: 11.33% vs. 7.93%), differences were non-significant in the Mann-Whitney-U-test for unrelated set of samples.

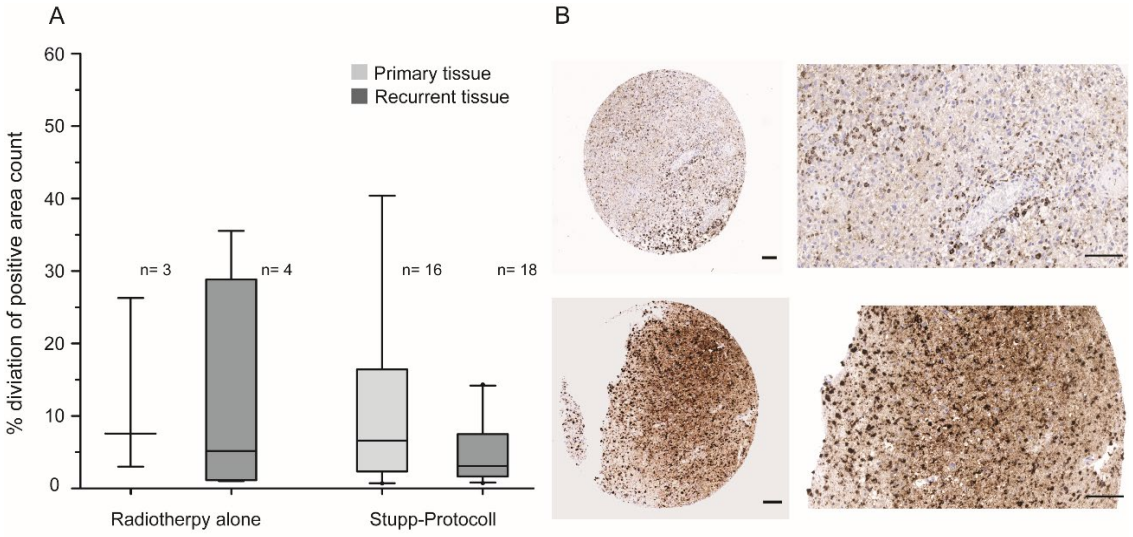

Figure 9: General statistical values and cohort heterogeneity.
A: Boxplot of expression deviation between treatment groups and tissue origin.
B: Example of intratissue heterogeneity after first diagnosis. Pictures were taken with 5x or 20x magnification. Scalebar 100 µm.

Sub-grouped-analysis based on treatment as indicated in box-plots in Figure 9 showed slightly higher expression in samples treated with radiotherapy alone against Stupp-protocol ($Mean_{Radio}$:19.81/ $Median_{Radio}$:11.70 vs. $Mean_{Stupp}$:15.43% / $Median_{Stupp}$:8.9%), again difference was not statistically significant in the Wilcoxon-Test for dependent samples. Next, CSF1R presence between either primary or recurrent samples which have received radiotherapy alone against primary and recurrent samples which have received standard of care therapy (Stupp protocol) were statistically compared. Comparison of primary tissue showed consistent and similar expression of CSF1R in both treatment groups. Inside the recurrent tissue groups, slightly higher expression in tissue collective which received radiotherapy treatment, which did not show statistically significance in the Mann-Whitney-U-test were observed. Moreover, expression inside the 2 different treatment groups was statistically tested. In the radiotherapy group, primary tissue showed the highest expression of CSF1R in all subgroups

($Mean_{radio\ prim.}$: 22,348%), observed decrease of expression in recurrent samples ($Mean_{radio\ recur.t}$: 16,445%) does not show statistical significance in the Wilcoxon-test. Our findings were consistent in the Stupp-protocol group. It could be observed again higher expression in primary tissue and small decrease towards the recurrent tissue which does not show statistical significance.[108]

For evaluation of staining heterogeneity, staining differences between tissue cores from same patients were further assessed. Qualitatively staining signals were not equally distributed over the tissue cores. Overall, heterogeneities of 71.43% of primary tissue samples and 78.57% of recurrent tissue samples could be evaluated. Interestingly, CSF1R expression inside primary tissue samples, differed in same cases very strongly as visualized in Figure 9B. Recurrent tissue samples in general seemed to have less heterogeneity, which was illustrated by a median difference between tissue cores of 3.1% in area staining percent in contrast to 6.087% in primary tissues. Subgroup analysis showed no differences or trends concerning heterogeneity between different treatment groups.

Besides absolute staining percentages results were grouped in semiquantitative expression groups visible in Table 9, referring to level frames of Moreno et al. (see 2.2.2.2), too.

Table 9: Semi-quantitative CSF1R expression measurement
Semi-quantitative frames refer to Moreno et al. Mean expression levels were calculated by semi-automated threshold based staining quantification [positive cell area count].

			No expression (<1%)*		Low (1-10%)*		Intermediate (10-25%)*		High (>25%)*	
Tissue type	N^0 tumor cases	Mean % Positive cell area count	N^0 cases	%	N^0 cases	%	N^0 cases	%	N^0 cases	%
Newly Diagnosed GB	6	22.348	1	16.7	2	33.33	1	16.7	2	33.3
Progressive GB	6	16.445	1	16.7	3	50	1	16.7	1	16.7
Total Treatment Group radiotherapy	12	19.397	2	16.7	5	41.7	2	16.7	3	25
Newly Diagnosed GB	22	19	1	4.5	10	45.5	4	18.2	7	31.8
Progressive GB	22	13	1	4.5	12	54.5	4	18.2	5	22.7
Total Treatment Group Stupp Protocol	44	16.261	2	4.5	22	50	8	18.2	12	27.3

Primarily, it is visible that over 25% of all samples showed high CSF1R expression, especially primary tissue samples seemed to have higher expression levels than recurrent samples (Table 9). Moreover, expression comparison comparing primary vs. recurrent tissue and differences between treatment groups were repeated. Semiquantitative grouping showed that earlier described higher expression in the radiotherapy treatment did not show up inside expression level analysis (see Table 9). Interestingly. both treatment groups showed even stronger similarities concerning expression level distribution than the absolute quantitative results as shown in Table 9.

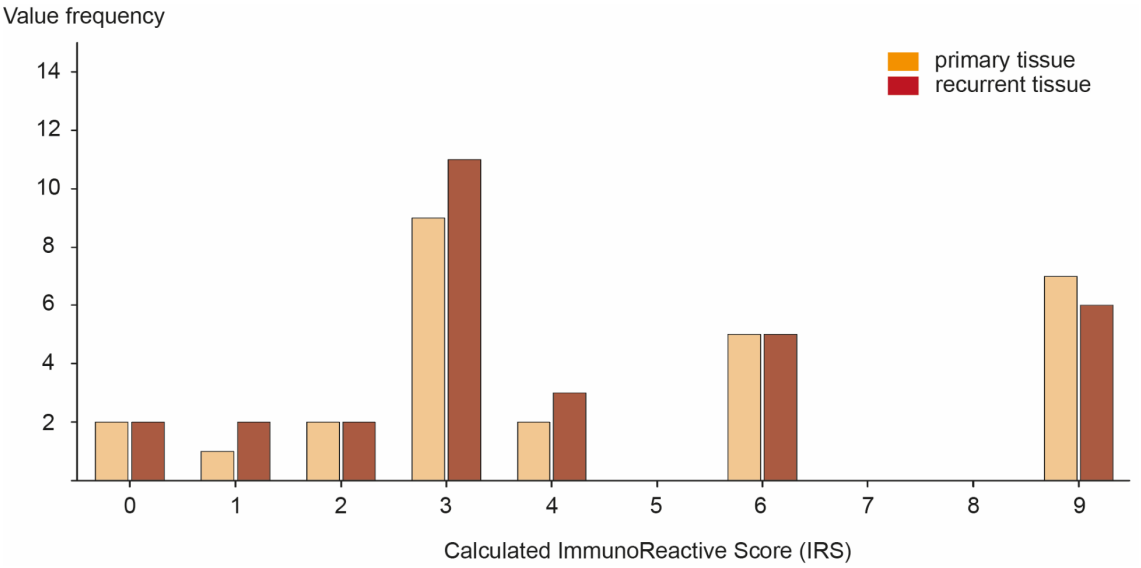

Figure 10: IRS frequency
IRS was defined as multiplication of interval-based expression scores with semi-quantitative intensity scores. Sample numbers are as indicated in Table 9. Image adapted from Przystal and Becker et al. [108]

To confirm CSF1R expression patterns, immunoreactive scores (IRS) which link staining intensity and frequency were calculated, too.[108, 121, 122] In general, CSF1R staining revealed high staining intensity scores. Mean IRS values for samples after first diagnosis were 4 versus 4.4 after first progression. As shown in Figure 10 IRS values confirm results shown in Table 9.[108]

As a next step, expression changes between primary and recurrent tissue of the same patient were compared. The term “expression change” was defined in 2 different ways either detection of at least ±5% change in positive cell area count or change of semi-quantitative expression level. As it is shown in the table of

Figure 11A, both quantitative and semiquantitative analysis show comparable results. Acquired values reveal that over 50% of all matched pairs show same CSF1R expression in primary and recurrent tissue samples. If expression differs between tissues more cases showed higher CSF1R expression in primary tissue samples than in recurrent tissue samples (range 25-31% of samples, see Figure 11). Moreover, referring to the semiquantitative results, over 40% of observed expression changes spanned over more than one expression level in both treatment groups. Figure 11B shows representative pictures examples of either stable expression or expression changes.[108]

All in all, the human tissue data set showed that CSF1R is present in both primary and recurrent tissue samples. Moreover, analysis reveal no statistical difference of CSF1R expression linked to received treatment or after first relapse of disease. Majority of stained tissue samples present potential intratumourally heterogeneity of CSF1R expression (see Figure 9). Alternative quantification approach using a well-established IRS confirms these findings (see Figure 10). Single case analysis showed that over 50% of cases have stable expression after first relapse (see Figure 11a) with tendency of revealing higher CSF1R expression after first diagnosis than after first relapse of disease.

Figure 11: Expression changes.
A: Table presents comparison of expression changes in quantitative and semi-quantitative data analysis. B: Representative pictures of cases which show either stable or unstable CSF1R expression during history of disease. Pictures were taken with 40x (main pictures) or 5x (whole tissue core) magnification. Scalebar 100 µm.

3.2 Targeting of CSF1R and PD1 in the VM/Dk mouse model

3.2.1 Animal experiment structure and setting

For evaluation of treatment dependent TME modification, animal studies were performed. For this, a syngeneic, immunocompetent murine glioma mouse model, called VM/Dk and SMA560 tumour cells was used.[96, 109, 128]

As Figure 12 shows, mice were rationed into 5 different treatment groups. Every group consisted of 5 animals. 2 of 5 groups where control groups for either anti-CSF1R (MOPC-21; IgG1) or anti-PD1 (C1.18.4; IgG2a) antibodies, 2 monotherapy regimes with either anti-PD1 (RMP1.14) or anti-CSF1R (2G2) antibodies. Last group was treated with a simultaneously performed combination therapy with anti-PD1 and anti-CSF1R antibodies (see 2.1.10.4).[108]

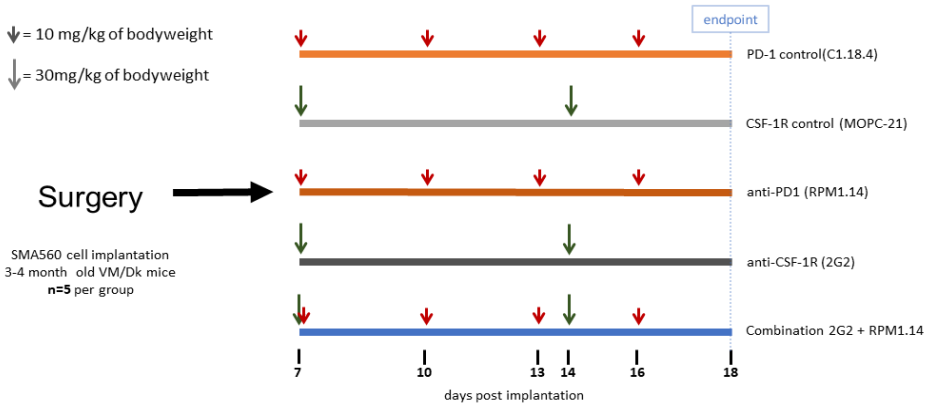

Figure 12: VM/DK- animal experiment schedule.
Treatment started 7 days post implantation (dpi). Animal experiment was closed at day 18dpi

As described above in 2.2.3, SMA560 cells were implanted intracranially. Animal scoring were executed as described in 2.2.4.1. Treatment started at day seven as visible in Figure 12 and as described in 2.2.4.

Mice of group anti-PD1[129] and its IgG2a control were treated every third day with a dose of 10mg per kg of bodyweight. Mice of group anti-CSF1R[88] and its IgG1 control were treated every seven days with a dose of 30 mg per kg of bodyweight (see Figure 12). Experiment was closed when the first animal of all groups fulfilled endpoint criteria as outlined in paragraph 2.2.4.1.

Overall, mice treated with anti-CSF1R or its control received 2 injections. Mice treated with Anti-PD-1 or respective control received 3 injections. Combination therapy group received 5 injections before reaching day 18.[108]

All animals were euthanized and 3 brains per groups were collected, perfused, frozen and further histologically processed as described in 2.2.5 and 2.2.6.

3.2.2 Evaluation of the tumour microenvironment with IHC

As described in 2.2.9 IHC were performed to observe possible treatment related changes of the TME and its containing immune cells. Therefore, collected brains were explanted and stored as fresh frozen tissue. Brains were cut axially and IHC were made. Stained sections were finally qualitatively and quantitatively examined and statistically evaluated as described in the preceded material and method part (2.2.9- 2.2.11).

3.2.2.1 IHC show glioblastoma like invasiveness but do not show treatment related changes in proliferation and angiogenesis.

For evaluation of possible treatment related changes in glioma-specific features like proliferation, cellular origin, angiogenesis and invasiveness was analysed. Therefore, stainings to detect proliferation marker Ki67, Glial fibrillary acidic protein (GFAP) and platelet endothelial cell adhesion molecule (PECAM-1/CD31) were performed.

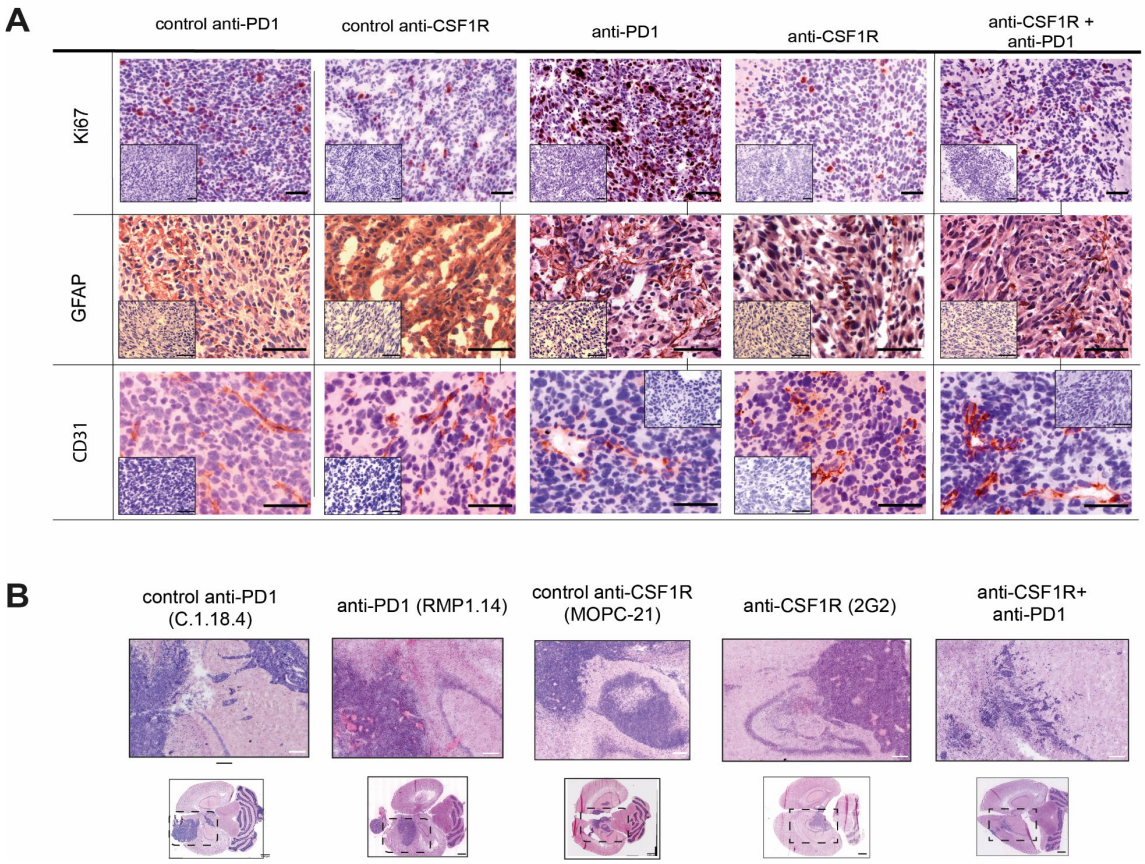

Figure 13: Histologic panel of H&E-, GFAP- and CD31- staining.
(A) Pictures were taken with 20x (Ki67) or 40x magnification (GFAP and CD31). Small pictures in lower left corners represent secondary antibody control sections. Scale bar 100 µm.
(B) Representative H&E sections showing tumour borders, illustrating infiltrative tumour cell growth. Upper image, 5x magnification, scale bar 200µm. Bottom: overview image, scale bar 1000µm. Images adapted from Przystal and Becker et al. [108]

As the first row of Figure 13 shows Ki-67 staining, a well-established marker for proliferating cells, showed strong, intensive specific nuclei staining signal in all evaluated tissue sections.[108] Qualitatively, Ki-67 reduction was found after CSF1R single treatment. Tumour sections from the PD1 treatment group showed

strongest Ki-67 staining and most enrichment of Ki67 positive tumour cells. As Figure 14 reveals quantification of Ki-67 positive cells support trend towards decrease of Ki67 signal after anti-CSF1R monotherapy in comparison to control group without statistical significance.[108] Other treatment groups showed strong heterogenous results of Ki-67 signals without statistical significance. Overall, Ki-67 staining does not show any specific distribution pattern comparing tumour regions.

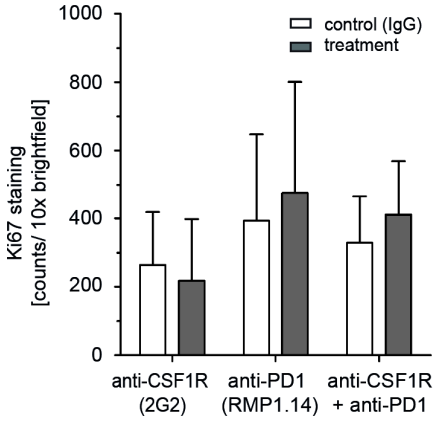

Figure 14: Absolute Ki-67 staining quantification.
Three animals (n=3) per group were analysed. Combination therapy was normalized to the average value of both control groups. One-way ANOVA followed by Tukey's multiple comparison test was used. Graph adapted from Przystal and Becker et al. [108]

Staining against GFAP (second row, Figure 13), generally strong expressed in astrocytes[130] or astrocytic tumours, showed strong fibrillary signal in all evaluated tissue sections. Strongest staining signal was discovered in both control groups. In contrast, more specific fibrillary, astrocytes characteristic staining in all treatment groups which moreover showed qualitatively reduction in comparison to control groups, were detected. GFAP seemed homogeneously spread about all regions of tumour tissue.

CD31, a well-established marker for vessel endothelia, showed strong vessel specific signals and staining distribution (see Figure 13, row 3). Tumour areas showed strong enrichment of neovascularisation and big vessel formation along tumour regions. Any distribution or vessel formation differences between treatment and control groups could not be detected.

As shown in Figure 13B and Figure 15 implanted SMA560 cells formed tumours that infiltrate the adjacent brain tissue illustrated by single scattered cell groups and unclear tumour boundaries.[108] Treatment depended differences

concerning invasiveness or tumour mass by qualitative histologic analysis could not be made.

3.2.2.2 Anti-CSF1R treatment alone and in combination with anti-PD1 reveal increase and change of TILs subpopulations

For examination of treatment related changes in the TME, the focus was on the infiltration of different T cell subtypes, their frequency and distribution. Figure 15 illustrates representative staining sections stained with several T cell specific antibodies.

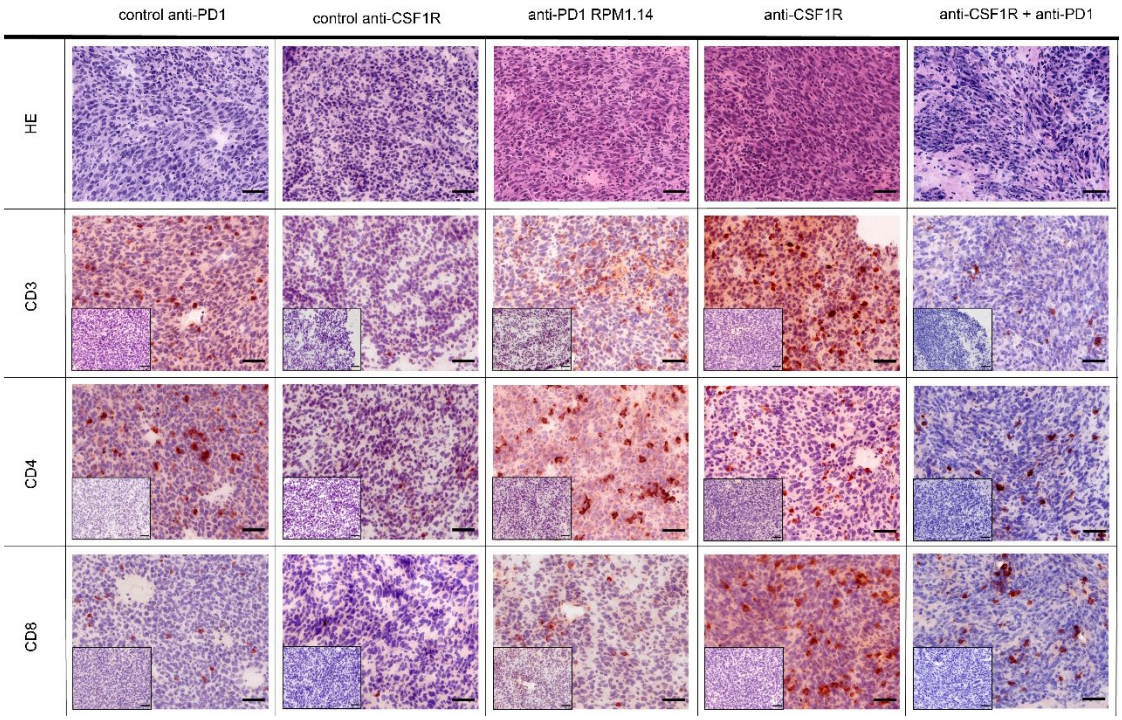

Figure 15: Histologic panel of CD3-, CD4- and CD8- staining.
Representative pictures were all taken from the same animal of respective treatment group. Small pictures present secondary antibody control. All pictures were taken with 20x magnification. Scalebar 100 µm. Images adapted from Przystal and Becker et al. [108]

As Figure 13B and the 1st row of Figure 15 shows, tumour nuclei are strongly stained blue violet in the H&E staining. In comparison to the normal brain tissue, tumour cells and their stained nuclei showed higher cell density. Edges of tumour areas showed rarely clear borders, mostly single strongly blue-violet stained nuclei can be detected in normal mouse brain tissue next to tumour areas which indicates tendency of infiltrative growth, as shown in Figure 13B.[108] In the H&E staining tumour cells showed heaped and disordered growth pattern. Moreover, evident differences between treatment groups concerning cell density,

distribution or growth pattern could not be detected. In general, IHC and H&E staining showed no tendency concerning difference in tumour expansion.

$CD3^+$ T cells showed strong specific membranous staining. As the 2nd row of Figure 15 reveals the number of $CD3^+$ cells were strongly increased inside the CSF1R monotherapy group in comparison to the respective control group. PD1 monotherapy and combination therapy group did not present increased number of CD3 positive cells in qualitative staining examination.

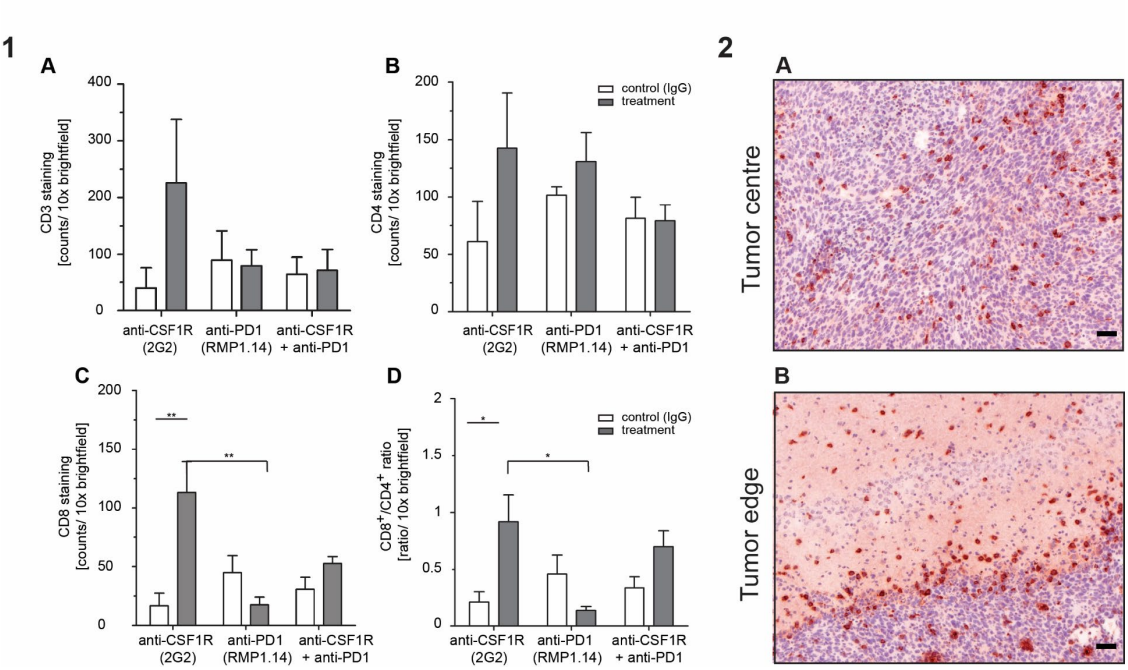

Figure 16: Staining quantification of CD3, CD4 and CD8 and staining heterogeneity.
(1): Staining quantification of $CD3^+$ (A), $CD4^+$ (B), $CD8^+$ (C) cells and ratio $CD8^+/CD4^+$ (D) of treatment groups vs. control groups. Three animals (n=3) per group were analysed. Combination therapy was compared to the average value of both control groups. Significance was tested with one-way ANOVA followed by Tukey's multiple comparison test. **p:< 0.01; p: *<0.05. Images adapted from Przystal and Becker et al. [108]
(2) Representative pictures of $CD8^+$ cell distribution at tumour edge (A) and centre (B). Picture were taken from brain tissue sample of CSF1R monotherapy group.
Magnification 10x, Scalebar 100 µm.

$CD4^+$ T-helper cells reveal strong, specific membranous staining in the 3rd row of Figure 15. In both monotherapy treatment groups, increased presence of $CD4^+$-cells, especially mice treated with PD1 showed high $CD4^+$ cell infiltration inside tumour tissue was observed. Combination therapy group does not present higher numbers of $CD4^+$ cells. Staining against CD8, expressed by cytotoxic T-cells, shows increased specific staining for $CD8^+$-cells in CSF1R monotherapy and the combination therapy regime in both qualitative examination of specific

staining.[108]

During staining examination by microscopy all T cell markers (CD3, CD4 and CD8) revealed specific staining distribution. As representative pictures of Figure 16 (2) present, most immune cells were found at tumour edges, wall like clustered. Fewer numbers of stained immune cells were found at the tumour centre.

Next, semiautomated threshold based staining quantification of sections stained against CD3, CD4 and CD8 was performed. IHC quantification results of three animals per group are illustrated as bar charts in Figure 16. Quantification in general supports qualitative staining findings of evaluated T cell markers. Overall, $CD3^+$ cells were the most present immune cell population in evaluated mouse brain samples. CD3 was highest expressed, mean value 225.67 stain count, in CSF1R monotherapy group but did not show any significant differences in expression to respective control group as the qualitative evaluation might support. PD1 single treatment and combination with CSF1R showed lower expression of CD3 and no statistically significant difference to respective control group ($Mean_{PD1}$: 79.67 counts; $Mean_{Combination}$: 71.67counts).[108]

CD4 quantification showed a statistical non-significant trend towards higher expression in treatment groups than in respective control groups (see Figure 16). Overall, highest expression was found in CSF1R monotherapy group ($Mean_{CSF1R}$: 142.42 counts), lowest expression showed combination therapy group ($Mean_{Combination}$: 79.113 counts). However, trends did not reach statistically significance.[108]

CD8 quantification revealed statistically significant higher counts in CSF1R monotherapy towards respective control group as shown in Figure 16. Combination therapy shows statistically non-significant higher numbers of $CD8^+$ cells than PD1 monotherapy group and respective calculated control-groups.[108]

Moreover, ratio between $CD8^+$ and $CD4^+$ cells was evaluated. As Figure 16 present, a statistically significant difference between ratio of $CD8^+$/ $CD4^+$-cells in CSF1R monotherapy towards respective control group was observed. Moreover, CSF1R monotherapy revealed significance towards PD1 monotherapy.

Combination therapy presented statistically non-significant higher ratio than PD-1 monotherapy and respective control-group.[108]

3.2.2.3 Combined anti-CSF1R and PD1 antibodies lead to staining signal decrease of TAM marker CD204 in IHCs

Next, IHC markers for TAMs were assessed. TAMs are recruited from both resident microglia and chemoattracted monocytes which can penetrate through the BBB and change their phenotype due to tumour produced chemokines as outlined in 1.2.[63] Both infiltrating monocytes and resident microglia express high levels of CD11b which is an adult macrophage marker, too.[63, 131]

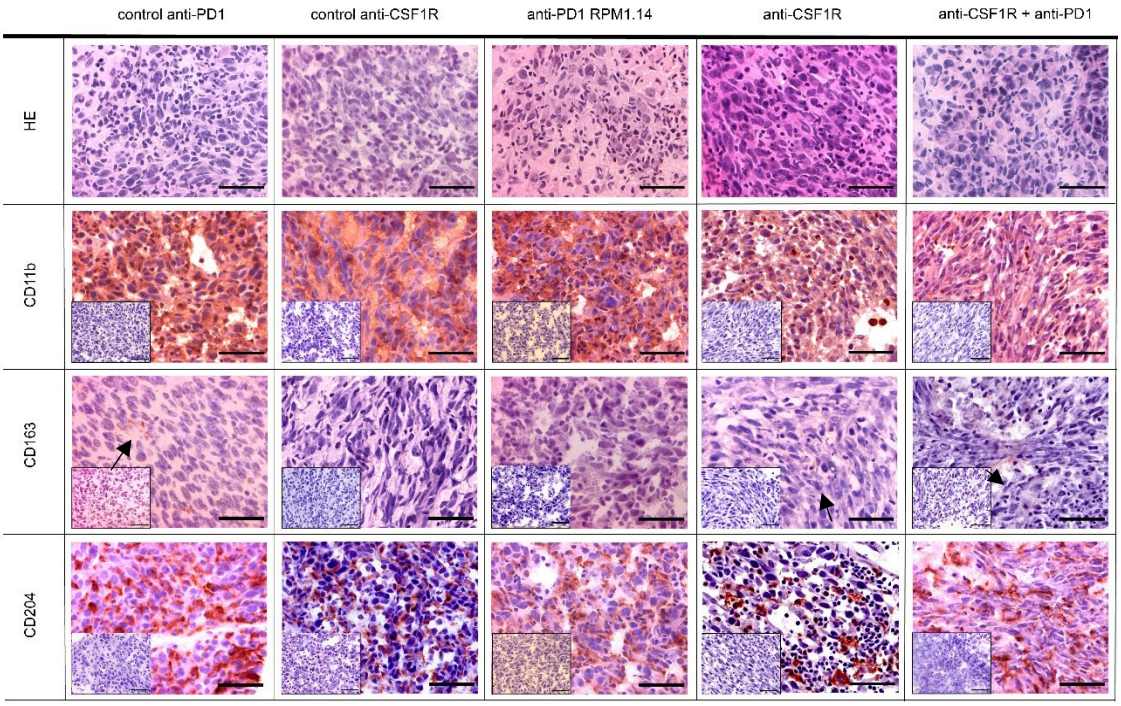

Figure 17: Histologic panel of macrophages markers.
Representative pictures of staining against CD11b, CD163 and CD204. Magnification 40x. Scalebars 50 µm. Images adapted from Przystal and Becker et al. [108]

As Figure 17 reveals staining against CD11b presented in all tumour samples a strong membraneous signal. In control groups and anti-PD1 treatment groups signal intensity were very high, as a consequence tumour tissue showed general strong reddish signal in complete tumour area without any hotspot areas. In the anti-CSF1R and combination treatment group, less numbers of $CD11b^{+}$ cells which was expressed by less intense and more specific colour signal inside respective tumour tissue were observed.(see Figure 17, row 2).[108]

Staining against CD163, marker for infiltrating TAMs in solid tumours which correlate with poor prognosis, showed in general low staining signal in all treatment groups as visualized in row 3 of Figure 17.[88, 132] In some tumour areas single positive cells could be found. Staining intensity was weak and stained cells were very small (arrows in Figure 17 row 3). Absolute quantification of CD163 visualized as a bar chart in Figure 18A, confirmed lack of CD163 expression with a signal area coverage under one percent.[108]

Staining against CD204^{+}-macrophages which correlate with glioma grade and poor patient outcome, presented in all stained sections specific and sharp membranous staining.[71, 88] In all groups clearly positive stained cells were detected. Number of CD204^{+} stained cells was distinctly reduced in the CSF1R and combination treatment group as shown in Figure 17 row 4. Control groups and Anti-PD1 treatment group showed qualitatively higher number of positive stained cells, and staining covered majority of tumour tissue. In general, staining was regularly distributed over the tumour tissue without any perivascular hotspots or specific localization dependent enrichments. CD204 staining quantification illustrated in Figure 18B revealed a strong tendency without statistcally significance for reduction of CD204 in the CSF1R monotherapy and in the combination therapy regime in comparison to respective control groups.[108]

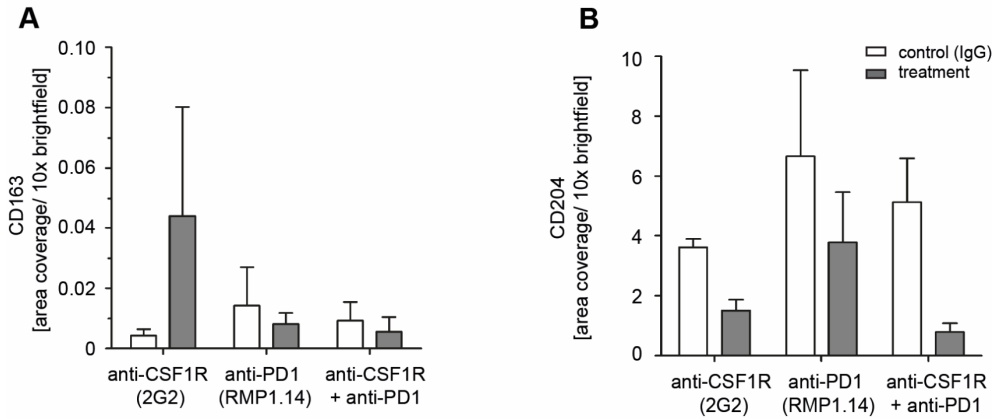

Figure 18: Staining quantification of TAM markers CD163 and CD204.
(A) Proportional CD163 area coverage quantification.
(B) CD204 staining quantification, treatment groups vs. control groups Three animals (n=3) per group were analysed. Combination therapy was compared to the average value of both control groups. Significance was tested with one-way ANOVA followed by Tukey's multiple comparison test. Graphes adapted from Przystal and Becker et al. [108]

3.2.2.4 B cell marker CD45R is present in all treatment groups

Additional B-cell specific markers were evaluated for getting a general impression of the TME (see Figure 19).

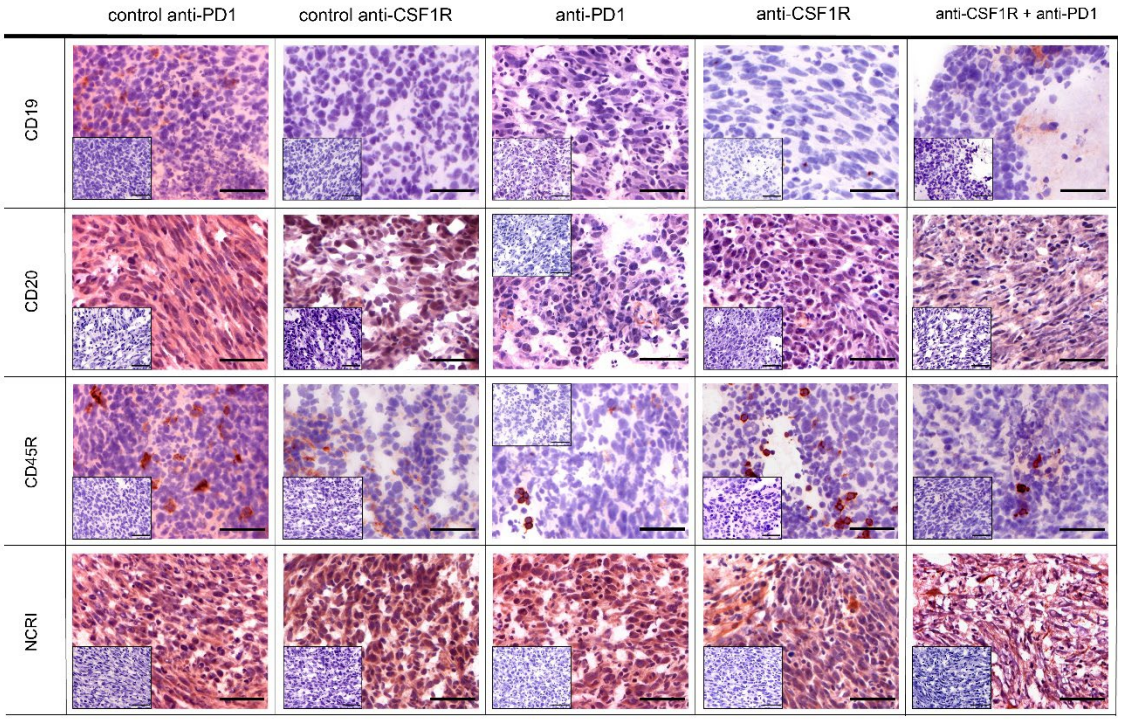

Figure 19: Histologic panel B cell specific markers.
Representative pictures stained against CD19, CD20, CD45R.Magnification 40x, scale bars 50µm.

CD19, an B-cell antigen which plays a role in B-cell development and intrinsic B-cell signalling [133], was heterogeneously expressed. CSF1R and its control reveal no presence of CD19. Anti-PD1 and combination with CSF1R showed single positive cells without any perivascular enrichments. (see Figure 19, row 1) CD20, strongly present on activated B-cells [134], presented intermediate expression in evaluated tissue samples. Anti-PD1 control revealed highest enrichments of $CD20^{+}$ cells. All other treatment groups showed same levels of CD20 expression.

CD45R, also known as B220 which is widely expressed on B- and T-cells, showed sharp and strong single nuclei cell staining in evaluated tissue samples. In every treatment group, small groups of few $CD45R^{+}$ cells were found. Most CD45R expression could be detected in the PD1 control group. (see Figure 19, row 3) All other 4 treatment groups presented consistent number of $CD45^{+}$ cells without any specific localized enrichments.

Natural cytotoxicity triggering receptor 1 (NCRI), common marker for natural killer (NK) cells, presented in general strong staining signal. (see Figure 19, row 4) In both control and the single PD1 treatment group, strong homogeneous, membranous staining signal could be detected. CSF1R alone and in combination with PD1 showed more specific staining signal and pattern over the whole tumour area.

3.2.2.5 Staining against treatment targets and apoptosis shows decrease of CSF1R and increased apoptosis signals in anti-CSF1R receiving treatment groups

For evaluating direct treatment response, staining against treatment target CSF1R, PD1 and its ligand PD-L1 was conducted. Moreover, staining signal of downstream apoptosis marker[135] caspase 3 cleaved was assessed.[108]

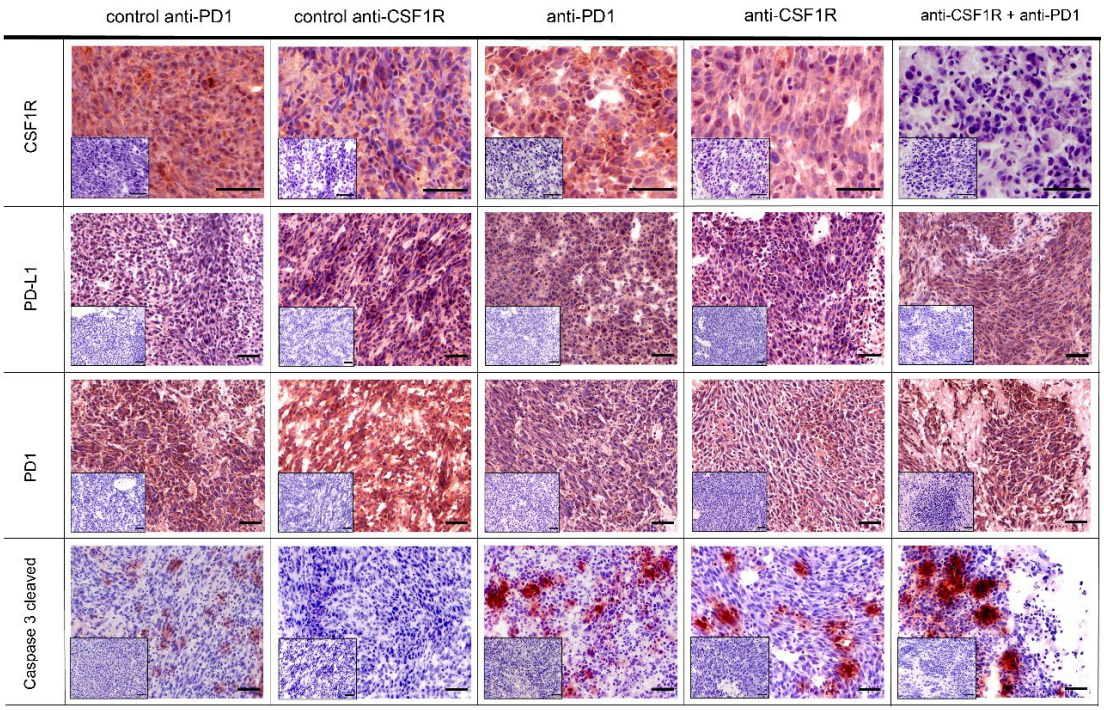

Figure 20: Histologic panel including target specific and apoptosis markers.
Tissue was stained against CSF1R, PD-L1, PD1 and Caspase 3 cleaved. Magnification 40x or 20x, scale bars 50µm. Images adapted from Przystal and Becker et al. [108]

CSF1R staining was present in all treatment groups and their control groups. Antibody staining showed cytoplasmic, fibrillary staining pattern. Highest staining signal could be qualitatively evaluated in both control groups and the PD1 monotherapy group (See Figure 20, row 1). Strongest reduction of staining

frequency and intensity was visible in representative images of the combination therapy group. CSF1R monotherapy led to reduction of staining frequency and intensity in comparison to respective control group, too.[108]

PD-L1 staining revealed presence of PD-L1 in relevant parts of tumour tissue (see Figure 20, row 2). CSF1R control and anti-PD1 treatment group showed highest number of PD-L1 expressing cells. Cytoplasmic staining signal was steadily distributed over evaluated tumour tissue. Slight reduction of PD-L1 expression was detected in combination and in CSF1R single therapy groups. PD1 was present in all treatment groups. Control groups showed strong staining signal and intensity without high specificity (see Figure 20, row 3). Monotherapy groups presented qualitative reduction of staining signal, thus less PD1 expression.[108]

Staining against caspase 3 cleaved revealed enhancement of staining signal in all treatment groups in comparison to respective treatment groups (see Figure 20, row 4). Highest and most frequent qualitatively evaluated staining signals could be found in combination therapy group and after CSF1R monotherapy. Quantification of caspase 3 cleaved staining signals in numerous representative slides of 3 animals per treatment group show highest staining signal between CSF1R monotherapy and the respective control group (see Figure 21, $p_{CSF1R\ vs.\ control} \leq 0.082$), followed by the simultaneous combination therapy group.[108]

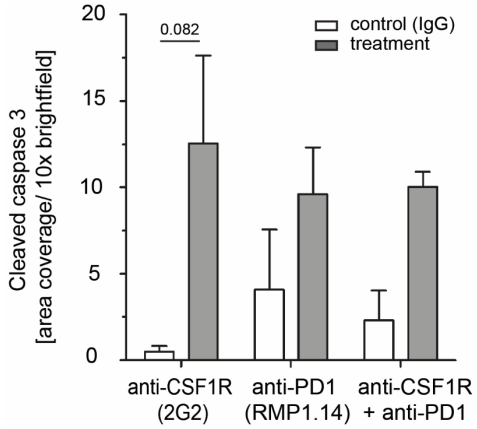

Figure 21: Caspase 3 cleaved area coverage quantification.
Three animals (n=3) per group were analysed. Combination therapy was compared to the average value of both control groups. Significance was tested with one-way ANOVA followed by Tukey's multiple comparison test. Graph adapted from Przystal and Becker et al. [108]

In summary, histological analysis of post-treatment tissue might indicate recomposition of the TME. Threshold- based staining quantification showed increased number of $CD8^+$ T cells, particularly in the CSF1R monotherapy and the combination therapy regime. Moreover, decrease of TAM markers CD204 and CD11b after CSF1R inhibition and its combination with anti-PD1 treatment was observed. Finally caspase 3 cleaved an apoptosis marker was increased in all three treatment groups. [108]

3.3 Immunological characterisation of a PDGFB driven glioma mouse model using the RCAS/TVA delivery system.

3.3.1 Animal experimental structures

Anti-CSF1R treatment in combination with anti-PD1 immune checkpoint inhibition showed re-composition of the TME in the immunocompetent VM/Dk mouse model using the syngeneic spontaneous developed mouse glioma line SMA560.[109] As outlined in paragraph 1.3 the chosen model reflects glioma specific histologic features. The used SMA560 cells show presence of MHC I and secretion of pro-tumourgenic cytokines which qualify the model for immunotherapeutic drug testing.[95, 98] In contrast GEMs do not depend on syngeneic intracranial tumour cell implantation as performed by using the VM/Dk SMA560 model. GEMs enable tumour formation by the mice themselves, they offer better interaction between the tumour and the TME and reflect better the course of disease as explained in 1.3.1.1. Consequently, a PDGF-B-driven proneural glioma mouse model using the RCAS/TVA somatic gene-delivery system was chosen for receiving more insights into the modulated TME.

First, in a pilot study, the model was established and characterised by imaging and immunohistochemistry. As a next step, a treatment experiment with multiple combination therapy approaches using anti-CSF1R and anti-PD1 antibodies which have been used in the VM/Dk mouse model was performed.[101, 136]

As Figure 22 shows, glioma formation was induced primarily by intracranial implantation of DF-1 cells which produce viruses containing a PDGFB amplification, as described in 2.2.1.4 and 2.2.3. Animals were regularly scored as described in 2.2.4. Animals were sacrificed when reaching defined endpoints (see Table 5).

In the first experiment virus producing DF-1 cells were implanted in seven animals. All operated animals survived surgery and post-surgical examination without signs for infection or neurological deficits. As the Kaplan-Meyer curve in Figure 24 shows mice reached defined endpoint of experiment between day 35 and 43 after surgery. animal brains were collected, perfused and histologically analysed as described in 2.2.5.

In a further experiment using the same experimental setup with eight animals MRI and PET imaging for monitoring tumour formation was included. Seven of eight operated mice survived surgery and post-surgical examination. As visualized in Figure 22, animals underwent MRI twice per week and received an additional baseline measurement one day before surgery (see 2.2.7). Moreover, animals underwent weekly FET-PET scans, depending on availability of the FET tracer, as described in 2.2.7.3. All animal brains were collected either after perfusion or without perfusion. Brains were further histologically analysed

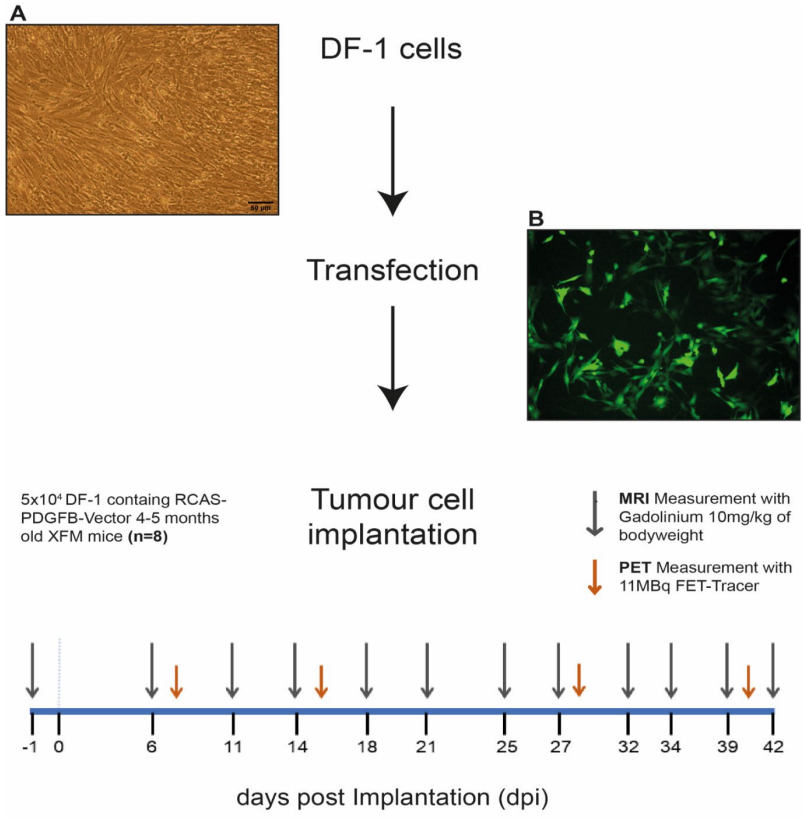

Figure 22: Experiment schedule using the RCAS/TVA system.
Tumour growth was monitored by MRI and PET measurements. (A) Picture of cultured confluent DF-1 cells, scale bar 50 µm. (B) Immunofluorescent image of DF-1 cells at day 5 after transfection with control-plasmid. DF-1 cells express GFP, magnification 20x.

As the Kaplan-Meyer curve in Figure 24 shows majority of mice became symptomatic between day 34 and 41. Two animals reached earlier defined endpoints during MRI measurements, probably due to acute cardiac arrests.

3.3.2 Experimental reproducibility: tumour formation leads to rapid weight loss

The first two performed experiments using the RCAS/TVA delivery system showed both stereotypical and similar experimental developments.

After tumour induction through implantation of virus producing DF-1 cells, mice showed a period of stable general appearance. Most animals could even increase their body weight during this time span despite of simultaneous tumour growth. As the representative bodyweight development curve in Figure 23 shows, mice could maintain stable weight status without neurological worsening until two or three days before reaching experimental endpoints including fast weight loss during two or three days.

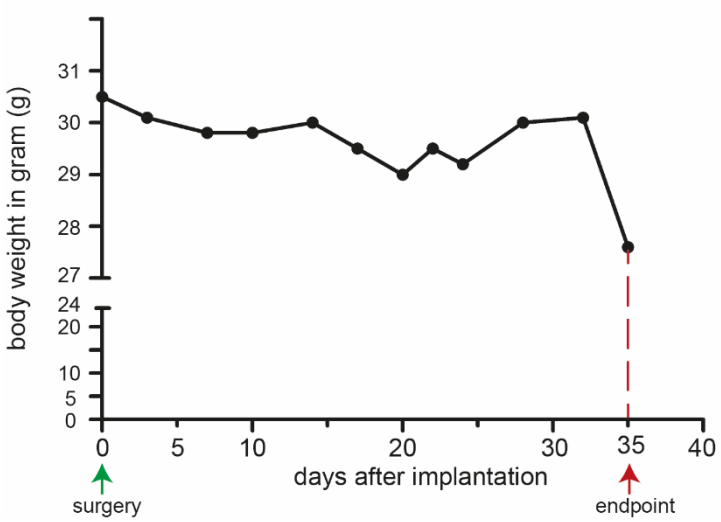

Figure 23: Representative body weight curve.
Exemplary mice of the first experiment were sacrificed at day 35 after surgery because of reaching defined experiment endpoint as outlined in Table 5. Green arrow indicates surgery, red arrow indicates experimental endpoint.

Comparing both executed experiments stable reproductivity of tumour formation can be found. According to the Kaplan Meyer Curve in Figure 24 untreated cohorts of mice with PDGFB driven gliomas show comparable median symptom-free survival (38 days vs. 39 days) referring to defined endpoints in Table 5.

Consequently, executed tumour induction using the RCAS/TVA model seems to be reproducible and show stable course of disease progression.

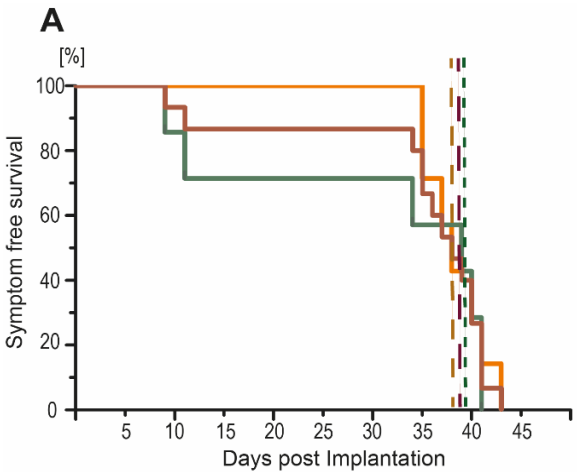

B

Studies	Median symptom-free survival in days
Pilot study (n=7)	39
Imaging study (n=7)	38
Merged (n=14)	38,5

Figure 24: Survival curves of pilot experiments
(A): Kaplan-Meyer Curve of both characterisation experiments using the RCAS/TVA system. (B): Table including median symptom-free survival and group size.

3.3.3 Monitoring tumour formation by MRI and FET-PET imaging

Second characterisation experiment included regular MRI and FET-PET measurements. Overall, 12 MRI measurements using contrast agent could be included for measuring the tumour growth development. As described in 2.2.7 tumour volumes were drawn and calculated.

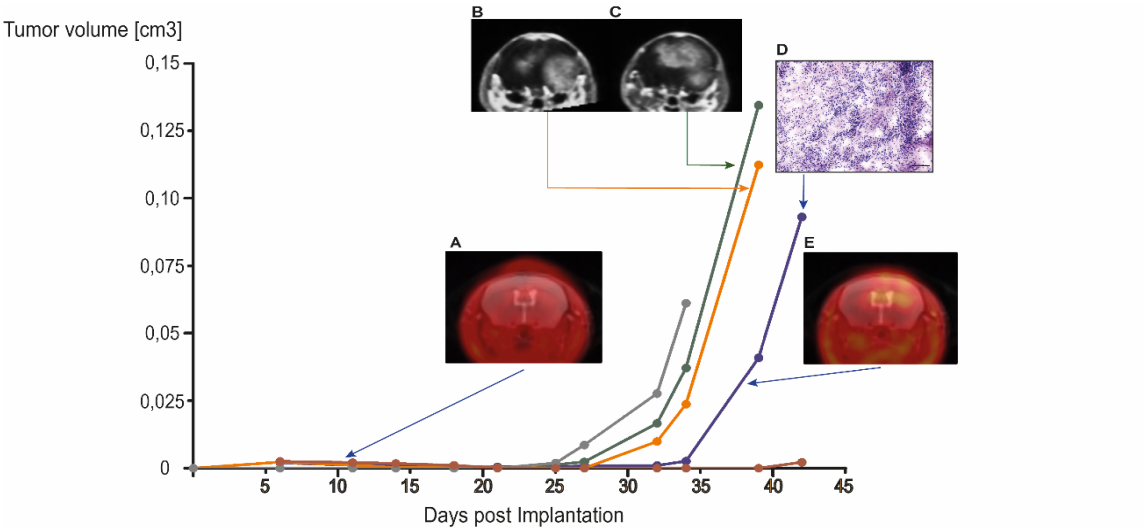

Figure 25. Tumour volume development of 5 representative MRI imaged animals.
(A): Representative FET-PET image day7, (B)+(C): Representative MRI images day 39 of 2 animals showing glioma like gadolinium enhancement in finale stage of disease. (D): Representative H&E staining showing glioblastoma like histology in region of previous occurred gadolinium enhancement. Scale bar 50 µm (E): Representative FET-PET image, showing FET activity in potential tumour areas at day 42.

As Figure 25 reveals, MRI could detect specific, tumour typical contrast agent enhancement as a sign for BBB leakage starting in the interval from day 25 to 32 after surgery. During the first 25 days slight self-receding signals could be detected between day 6 and 14 (volume range: 0.00118-0.00254cm^3). Visible weak, contrast enhancement might be short-time inflammatory processes caused by surgery or the viral infection process of resident glial cells expressing the TVA-receptor. During the first 25 days PET measurements showed no accumulation of FET. Detected tumour specific contrast agent enhancement started in region of DF-1 cell implantation but quickly increased in size and localisation. As visible in Figure 25B and C contrast enhancement were found bi-hemispheric, expanding over the corpus callosum, covering subcortical and temporal lobe regions at the last measurements before reaching defined endpoints (see 2.2.4.1). Additionally, strong FET accumulations were visible in regions with Gadolinium enhancement (see Figure 25E).

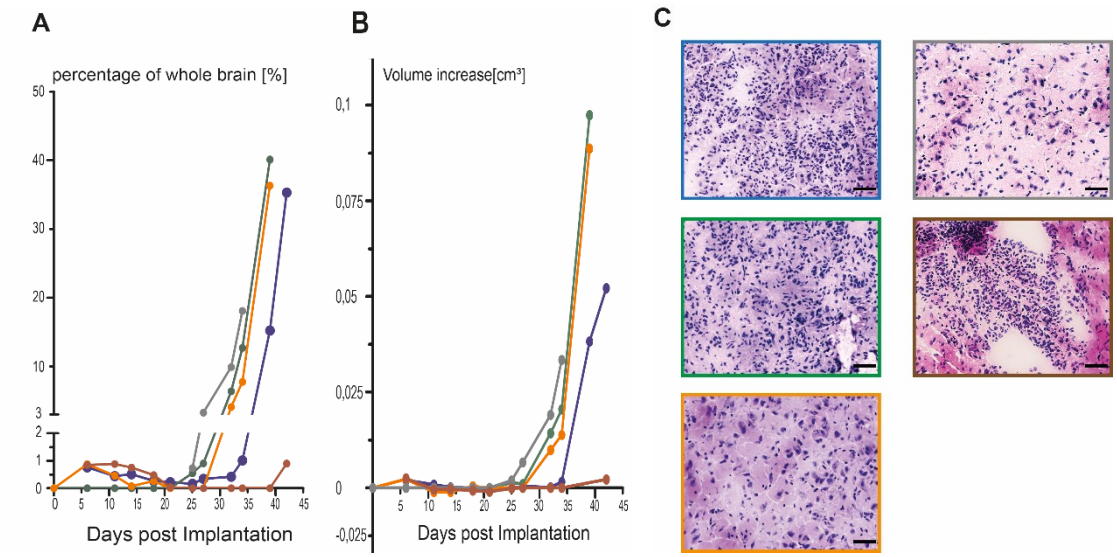

Figure 26. Tumour volume curves.
A): Tumour as a percentage of whole brain tissue. (B): Absolute tumour volume increase in cm3. (C): Representative *ex vivo* H&E staining images of observed animals. Frame colour represents respective line colour in A and B. 20x magnification. Scale bar 50 µm.

Overall, final volume measurement before reaching experimental endpoints, revealed volumes in range of 0.065cm^3 to 0.135cm^3 in four of five observed animals (Figure 25). Only one animal showed less contrast agent enhancement in the range of 0,002 cm^3 which represents less than 1 percent tumour volume

proportion of the whole brain volume (see brain curve in Figure 25 and Figure 26A). However, ex vivo H&E staining (Figure 26C, brown frame) showed a small group of basophilic stained cells in the region of DF-1 cell implantation without signs of infiltration into the resident brain tissue which might be a sign unsuccessful DF1 cell implantation. Contrast agent enhancement in general shows features of exponential growth which is illustrated in Figure 25 and 26 with highest growth rates between measurements on day 39 and 42. Calculated tumour volumes represent up to 18% to 40% of the whole mouse brain volume in the final stage of disease (day 39 to 42) in 4 of 5 observed animals(see Figure 26A).

After experimental closure and brain collection, H&E staining to assess if previously observed glioma like MRI findings correlate with histological diagnosis for glioblastoma formation was performed. As visible in Figure 26C in all 5 animals histologic features of gliomagenesis could be observed. High density of small strongly haematoxylin/ basophilic stained tumour cells with high grade of neovascularisation were found. Tumour cells generally infiltrated adjoined brain tissue. In 3 of 5 animals tumours showed huge dimensions and covered multiple brain regions as observed in MRI imaging. Additionally, infiltration and crossing of the corpus callosum could be seen in histology of 4 out of 5 animals which reached endpoint after day 32 post surgery.

To conclude *ex vivo* histologic finding support observations using longitudinal MRI and PET measurements.

3.3.4 RCAS/TVA model shows strong immune cell infiltration in IHC

Besides H&E staining multiple IHC staining against several tumour tissue infiltrating immune host cells and vascularisation markers were performed. Moreover, a basal comparison between the composition of the TME in the PDGFB- driven glioma model and the previously used VM/Dk mouse model was executed.

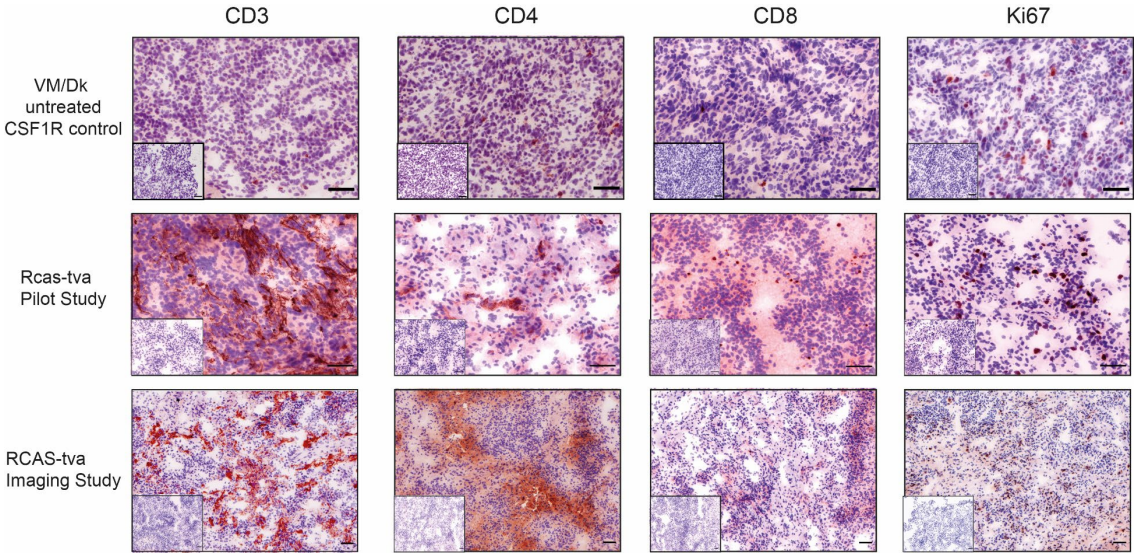

Figure 27: Histologic panel of CD3-, CD4- CD8- and Ki67 staining.
Representative pictures were all taken from the same animal of respective mouse model and experiment. All pictures were taken either with 10x (3rd row) or 20x (row 1+2) magnification. Scalebar 100 µm.

Staining against T cell specific markers showed generally stronger and larger staining distribution in the two performed experiments using the RCAS/TVA model for tumour initiation. As visible in Figure 27 staining signal coding for CD3 was very frequent in both experiments with the RCAS/TVA model (see 1st column Figure 27). Staining showed high specificity and uniform distribution over the tumour tissue. In untreated tumour tissue of SMA560 gliomas overall infiltration of $CD3^+$ cells was very weak and unspecific. Staining against CD4 showed highest specificity in the first performed RCAS/TVA pilot study. In the second experiment CD4 staining was still strong but with lower specificity. SMA560 glioma tumours showed only single positively staining cells expressing CD4 (see column 2 Figure 27). Cytotoxic T cells expressing CD8 were more often qualitatively visible in both RCAS/TVA experiments. Single positive $CD8^+$-cells with strong and specific staining were detected. In contrast, fewer cells were

found in the VM/Dk model (first row Figure 27). Proliferation marker Ki-67 was equally visible in all 3 experiments. No qualitative differences between both models could have been found. Ki-67 was often and stable expressed by tumour cells (column 4, Figure 27).

Staining against macrophages specific markers showed similarities and differences between both used mouse models.

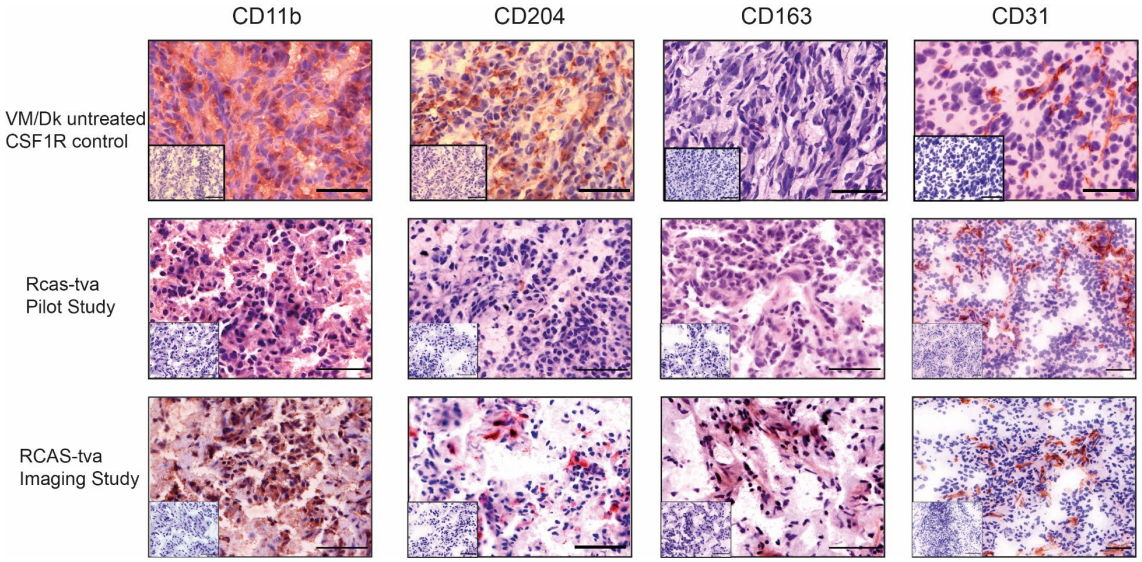

Figure 28: Histologic panel of CD11b, CD204, CD163 and CD31 staining.
Representative pictures were all taken from the same animal of respective mouse model and experiment. All pictures were taken either with 20x or 40x magnification. Scalebars 50 µm.

As visualized in the 1st row of Figure 28, stronger staining against CD11b was observed in the VM/Dk mouse model. However, both experiments using the RCAS/TVA delivery system showed strong and intensive staining against CD11b as visualized in the first column of Figure 28. Additionally, more $CD204^{+}$ cells were observed in the VM/DK mouse model and showed a wider range of distribution. In contrast, RCAS/TVA mouse tissue showed only single cells which showed sharp and specific staining signal (see column 2, Figure 28). Contrary CD163 staining showed higher staining signal in the performed RCAS/TVA experiments. Particularly tissue of the second experiment using longitudinal MRI imaging showed highly specific, fibrillary staining signal. The VM/Dk model only reveals singular positive staining against CD163 (column 3, Figure 28). CD31, highly expressed on endothelial cells and therefore a good vascularisation marker, was highly expressed in both used animal models. Both models showed frequent, large vessel formation. Overall, it seems like the RCAS/TVA model

more frequently build strong neovascularisation. Diameter of vessels and number of vessels seemed to be qualitatively higher in the RCAS/TVA model (column 4, Figure 28). VM/Dk vessel formation seemed to have smaller vessel diameter and lower frequency in comparison to the RCAS/TVA model.

In summary, immunohistochemistry comparison reveals that the RCAS/TVA system might have higher immunogenicity than the VM/Dk model. This finding is supported by higher numbers of infiltrating T cells. Interestingly, it seems like the VM/Dk model intrinsically attracts higher number of macrophages into its TME. Both models show high grade of neovascularisation, driven by the PDGFB-amplification the RCAS/TVA model show higher vessel density and higher vessel diameters.

3.3.5 Treatment experiment does not show significant symptom free survival benefits

As a next step a treatment study using the PDGFB-driven mouse model including the RCAS/TVA delivery system was performed. Therefore, the previously used therapy approach in the VM/Dk mouse model was used and adapted. Tumour initiation was performed as previously described in 2.2.1.4, 2.2.3 and 3.3.1. In this case a wider age range of animals were used referring to the respective animal licence listed in 2.2.4. Animals were in the range of three to six months.

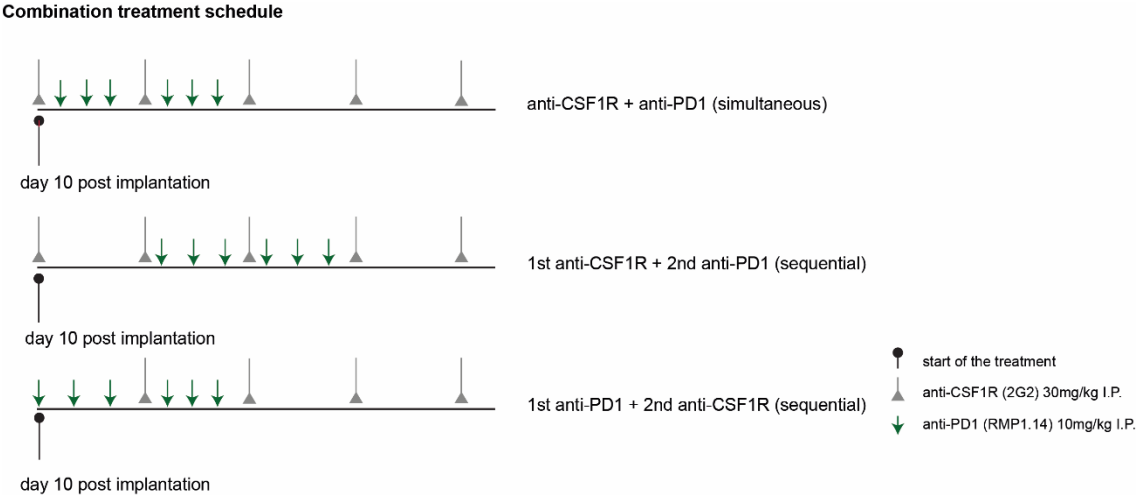

Figure 29: Combination treatment schedule.
Treatment started at day 10, antibodies were applied I P. Therapy groups consisted out of 7 animals per group. Besides 3 combination therapy groups there is one control group (MOPC-1), Anti-CSF1R and Anti-PD1 monotherapy groups.

As Figure 29 shows therapy starts at day 10 after DF-1 cell implantation. Overall, there were 6 therapy groups. 1 control group with an CSF1R control antibody (MOPC-21), single treatment groups with Anti-CSF1R, Anti-PD1 and 3 combination therapy groups with simultaneous and sequential treatments as shown in Figure 29.

42 animals were included into the treatment schedule of Figure 29 starting at 10 dpi. Treatment groups were equally balanced in regard of age and gender. All animals of the PD1 monotherapy group received 6 times anti-PD1 treatment. Furthermore, complete simultaneous combination therapy cohort received Anti-PD1 antibody for six times. Sequential treatment cohorts could not receive full dose of anti-PD1. Cohort starting with anti-CSF1R followed by anti-PD1 only 2 animals out of 7 received 6 injections, in contrast cohort starting with Anti-PD1 followed by Anti-CSF1R 5 of 7 animals could complete Anti-PD1 treatment.

In general, mice showed same stereotypical reaching the endpoint referring to Table 5, including weight loss as experienced in previously executed pilot studies described in 3.3.1+2. After a stable period without symptoms and stable bodyweight, mice reached defined endpoints, see 2.2.4.1.

A

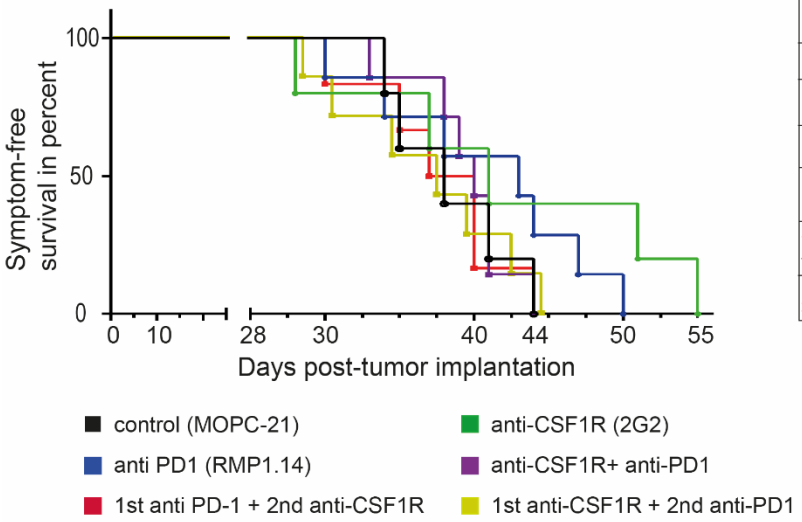

B

group	animal numbers	median symptom -free survival (d)
MOPC-21	5	38
anti-PD1	7	43
anti-CSF1R	5	41
anti-CSF1R +anti-PD1	7	40
1st anti-CSF1R + 2nd anti-PD1	7	37
1st anti-PD1+ 2nd anti-CSF1R	6	38.5

Figure 30: Onset of neurological symptoms in the RCAS/TVA treatment experiment.
(A) Kaplan-Meyer curve of executed treatment experiment using the RCAS/TVA model. Symptom-free survival is defined as reaching experimental endpoint as explained in Table 5
(B): Table showing median symptom-free survival and included group size numbers. Log-Rank test: 0.3652.

In Figure 30A the Kaplan-Meyer curve of the treatment experiment reveals no statistically significance in regard of time points reaching defined experimental endpoint between respective treatment groups and the control group (log-rank test: 0.3652). Statistically monotherapies groups showed longer median symptom-free survival (defined as reaching experimental endpoints in Table 5) than combination therapy regimes or control group as shown in Figure 30B. Comparing group consistencies simultaneous combination therapy group showed smallest standard deviation values (3.41), followed by the control group (4.16). Median symptom-free survival of control group was the same as observed in the previously executed pilot experiments which show reproducibility of untreated tumour formation. Interestingly monotherapy groups show very heterogeneous timepoints of reaching experimental endpoints. The CSF1R monotherapy group had two animals which reached experimental endpoints

between day 52 and 55 after surgery (see Figure 30A). However, the other animals of the group showed no latency of reaching experimental endpoint than our control group despite of the described long tail inside the Kaplan-Meyer curve. Comparing the combination therapy groups, the simultaneous combination therapy group in which all animals received full therapy performed better than the two sequential combination therapy groups in which only minority of animals could complete our treatment schedule.

To sum up our results, our study cannot show any statistically significant symptom-free survival benefits between mono- and combination therapy regimes. There are some long-term surviving animals out of both monotherapy groups which showed prolonged symptom-free survival.

Overall, the experiment shows a strong reproducibility of untreated glioma development in comparison to previously described pilot experiments, whereas treatment related survival benefits were highly heterogeneous.

3.4 Production of YFP and CFP labelled long-term glioma cell lines

As described in 2.2.13 and 14 two plasmids containing either YFP or CFP were constructed. Next, respective viruses were produced for transfecting long-term glioma cell lines. The aim of labelling long-term cell lines was to obtain further tumour cell monitoring possibilities for the following animal experiments. Fluorescence-labelled cells offer the possibility to better monitor tumour growth, for example through bioluminescence imaging or post-mortem fluorescence immunohistochemistry.

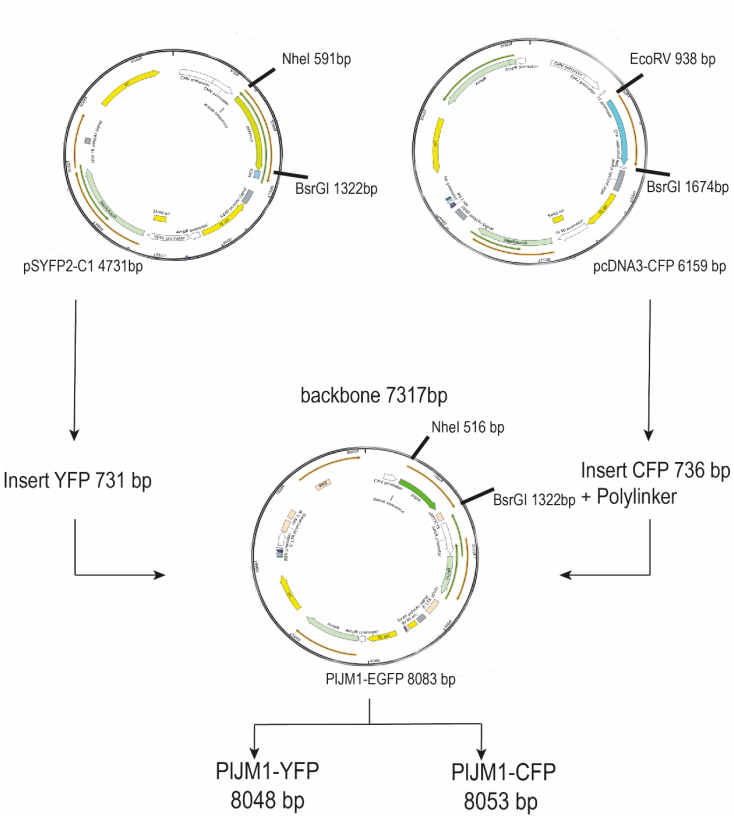

Figure 31: Cloning strategy for production of PIJM1-YFP and CFP plasmids.
Plasmid cards created and modified with SnapGene®.

3.4.1 Plasmid Construction

Figure 31 shows executed cloning strategy. As described in 2.2.12.1 our plasmids were cut by restriction digestion. For pSYFP2-C1 and PIJM1-GFP restriction enzymes *NheI* and *BsrGI* and for PcDNA-CFP restriction enzymes *EcoRV* and *BsrGI* were used. Plasmid fragments YFP (731bp), CFP including added polylinkers (736bp) and the PIJM1-backbone (7317 bp) were cut out of receiving gels, DNA were extracted and amount of DNA and purity were measured (see 2.2.12.1-3). Plasmid fragments were ligated (see 2.2.12.3) and as a control,

control-digestions with respective restriction enzymes were performed. Next, transformation in E. coli Stbl3 was performed as described in 2.2.12.4. Colonies were expanded by Maxi-preps. Plasmids were regularly checked by control digestions.

3.4.2 Virus Production

Lentiviruses for cell transfection were produced using the protocol described in 2.2.13. Respective packaging plasmids (pMDLg/pRRE, pMD2.G and pRSV-Rev) were manually expanded by maxi-preps. After virus production, virus titre was evaluated as described in 2.2.13.2. HT-1080 cells were transfected by viruses containing either PlJM1-CFP or YFP for 96h. DNA was extracted and a qPCR (See 2.2.13.2) was performed. In the qPCR comparison between the DNA-copies of house-keeping proteins and integrated viral DNA fragments were evaluated for calculating virus copy number. The number of DNA copies for albumin (Alb) was compared with the transfected plasmids (virus plJM1-CFP/YFP) using a primer for the post-transcriptional regulatory element of woodland mackerel hepatitis (WPRE), which provides information on the number of virus copies and their titres. [116]

Titration and calculation show that the virus including CFP has a vector copy number average in the range of 4.49-10.24 and a virus titre in the range of $2.69*10^8$-$1.54*10^9$ Tu/ml. Virus containing YFP showed a vector copy number in the range of 7.11-8.12 and virus titre in the range of 3.45-$6.04*10^8$ Tu/ml.

3.4.3 Transfection of long-term glioma cell lines

Infection of several long-term glioma cell lines with virus containing CFP or YFP was performed.

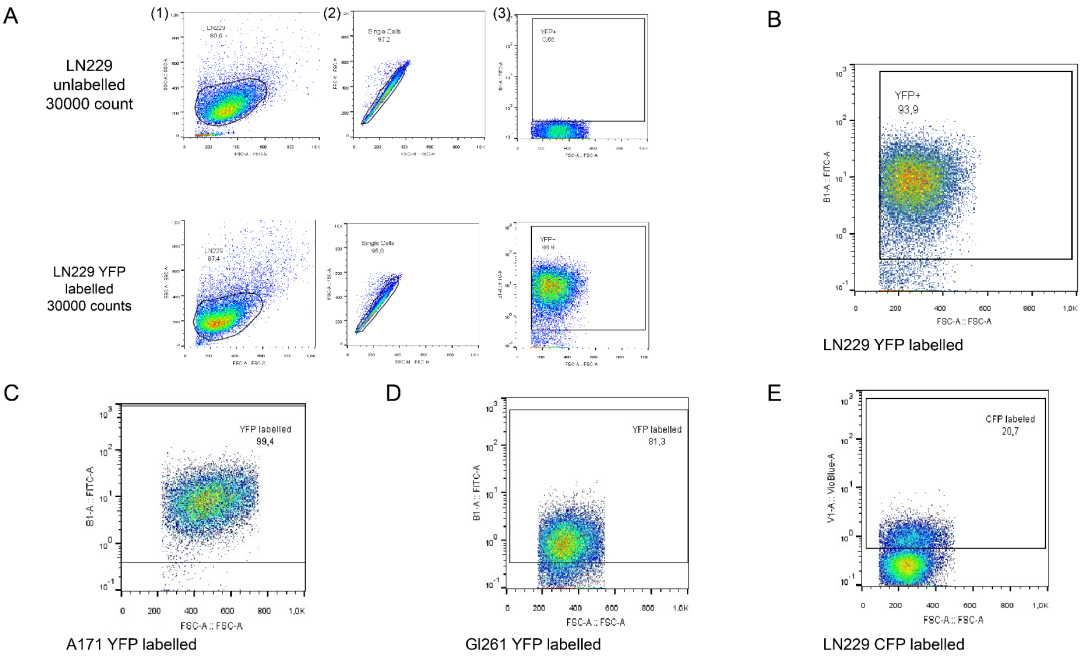

Figure 32: Transfection control by FACS measurements.
(A+ B): Exemplary gating strategy for testing cell labelling for LN229 unlabelled vs. transfected with Virus containing PIJM1-YFP, 30000 counts were evaluated by MACs quant flow cytometer (1): whole cell population, (2): single cells (3): labelled cell population D. Analysis was performed using FlowJO® 10 (C): A171 (D) GL261 labelled with YFP. (E) LN229 labelled with CFP.

Transfection of LN229, A171, GL261 was performed as described in 2.2.13.3+4 with 50 MOI of virus. Selection for cells positively transfected was performed by puromycin. After puromycin selection, transfected cells were expanded. Transfection control was performed by FACS measurements. FACS results are illustrated in Figure 32. Overall, successful transfection by YFP in all 3 transfected cell lines was observed. CFP containing virus could only show FACS signal in 28.7% of LN229 cell population in performed FACS measurement, the two other cell lines should insufficient survival of cells during puromycin selection.

4 Discussion

Even in highly selected clinical trial populations of patients with diagnosed glioblastomas the median overall survival is still in the range of 1.5 years.[10-12, 108] Despite of several clinical trials trying to evaluate effectiveness of immunotherapeutic therapy regimes or targetable structures of the tumour microenvironment (TME), studies could not reach primary endpoints or show treatment depended improvement of prognosis.[49, 53] However, preclinical studies focusing on the TME as therapeutic target have shown promising results *in vitro* and *in vivo*.[62, 77]

Most dominant cellular population inside the TME are tumour-associated macrophages (TAMs) which function as tumoural supporting host cells with up to 30 percent of tumour mass.[63, 71] Key axis in this regard is the interaction between the colony stimulating factor 1 receptor (CSF1R) and its ligand CSF1.[63, 67, 71] CSF1R is mainly expressed on TAMs which show a pro-tumourgenic phenotype and interacts with CSF1 which is strongly secreted by tumour cells (see 1.2 and 1.2.1).[61, 71] Consequently CSF1R plays an important role in TAM survival and differentiation in several tumour entities, including gliomas.[67, 132, 137] Its expression in gliomas correlates with higher malignancy and invasiveness *in vitro and in vivo* evaluated in preclinical settings.[67] In clinical study population, CSF1/CSF1R expression has been eagerly evaluated on gene-expression level and RNA level.[138] Data of chapter 3.1 and 3.2 has been published recently.[108] Interestingly, multidimensional analysis of CSF1R in IHC studies focussing on expression profiles after first diagnosis and after first relapse of disease have not been published before.[108] First study objective had the focus to assess presence of CSF1R in a cohort of patient-derived glioblastoma tissue.

CSF1R staining on a TMA was performed in a cohort of 28 patients with at least two tissue samples per patient for comparing CSF1R presence after first diagnosis and after first progression of $IDH_{wildtype}$ glioblastoma (see Figure 5). Anti-CSF1R antibody specificity was tested on human tonsil tissue (see Figure 7). Used anti-CSF1R antibody clone 29 showed high staining specificity and

staining pattern was consistent to a study by Moreno et al. which has examined distribution of CSF1R$^+$ macrophages in lymphomas by the use of a mouse monoclonal CSF1R antibody (clone FER216) (Figure 7 and 3.1.1).[119] Clone 29 antibody specificity was confirmed in chosen tissue samples, too. Staining pattern and observed staining morphology were well-comparable to free-accessible glioma tissue cores stained against CSF1R in the online available human protein atlas (see 3.1.1). [139] Unspecific staining signals inside and besides vessels potentially caused by degraded lymphatic cellular particles, were excluded from performed staining quantification (Table 9).

Performed IHC quantification showed consistent presence of CSF1R in the chosen study cohort with mean CSF1R expression of 16.28 percent positive stained area count (see 3.1.2). More than 90 percent of evaluated samples showed at least low expression (1-10 % positive cell area count) of CSF1R (Table 9), including over 25 percent of samples with at least high expression level (>25% positive cell area count).[108] Calculation of an established IRS as shown in Figure 10, confirms results of the quantitative and interval-based interpretation of evaluated CSF1R stainings.[108] Moreover, IRS links staining frequency with staining intensity and gives evidence of the strong staining signal in majority of evaluated tissue samples.

Shown presence of CSF1R in the evaluated patient cohort can be compared to studies which looked at RNA expression levels of CSF1 the ligand of CSF1R.[138] The authors could show in a comprehensive meta-analysis of several mRNA datasets that CSF1 is significantly upregulated in high grade glioma which might indicate broad presence of CSF1R, too.[138] Moreover several studies focusing on presence of macrophages and microglia inside the TME can show that immunohistochemical markers for TAMs like CD204 and CD68 are highly present in Glioblastoma.[71, 138] Particularly the immunohistochemical study of Komohara et al. shows that expression of CD204 and CD68 correlate with higher tumour grade and CD204$^+$ infiltrating macrophages are highly present in glioblastomas.[71] Interestingly, Komohara et al. additionally could show that presence of m-CSF1 correlates with WHO Grade of evaluated glioma, too.[71]To test if CSF1R which is according to the literature

mainly expressed on TAMs is associated with higher number of TAMs, chosen 28 matched glioma pairs were stained against CD204 and CD163, too. As shown by Przystal and Becker et al. staining quantification revealed high expression of CD204 and CD163 inside primary and recurrent tumour samples.[108] Correlation analysis with CSF1R showed statistically significance in primary tissue samples, too ($r_{prim\ CD163\text{-}CSF1R}$= 0.492, $p_{prim.}$ < 0.005; $r_{prim\ CD204\text{-}CSF1R}$ =0.381, p < 0.003).[108] This finding supports presence of CSF1R on infiltrating and resident macrophages and microglia in human glioblastomas and underlines the well-known presence of TAMs inside the TME of high-grade gliomas in a cohort of matched-pair tissue samples.[108]

Besides, TAM infiltration and CSF1R expression profiling, staining against CD3, CD4, CD8 and the immune checkpoint PD1/PD-L1was performed for better description of the present TME composition in the evaluated matched-pair tissue sample cohort, too. PD1 and its ligand PD-L1 could be observed at low expression levels in the majority of cases and correlated positively with CD204 and CD163 which highlights coexistence of both possible treatment targets.[108] In this regard, Berghoff et al. has published a comprehensive study focusing on correlation of Tumour infiltrating lymphocytes (TILs) markers and expression of PD1 and PD-L1 in a large subset of unmatched glioblastoma samples, mainly consisting of tissue samples after primary diagnosis.[84] In contrast executed IHC study in this work underline presence of TILs as well as moderate expression of PD1 and PD-L1 in a smaller study cohort which consists exclusively out of matched-pair tissue samples. In comparison to CSF1R, PD1 showed weaker staining intensity and showed lower frequency of staining signal. PD-L1 revealed higher presence as PD1 in evaluated tissue samples and showed comparable quantity of staining signal as CSF1R as shown by Przystal and Becker et al.[108] However, staining intensity was higher for CSF1R compared to PD-L1 in majority of evaluated matched pairs. Moreover, presence of PD-L1 correlated positively with CSF1R in primary tissue samples ($r_{prim:PD\text{-}L1\text{-}CSF1R}$= 0.492, p_{prim}<0.005).[108] Additionally, presence of PD1 in primary tissues correlated positively with presence of $CD4^+$ cells inside the TME.[108] Logically expected positive correlation between cells expressing CD3 and subpopulation defining markers

CD4 and CD8 were detected after IHC quantification, too.[108] Like Berghoff et al. have shown, no significant expression changes in recurrent tissue samples in comparison to primary tissue samples could be evaluated.[84, 108] Consequently, it could be verified that besides CSF1R, targets for immune-checkpoint inhibitors PD1 and PD-L1 are present in evaluated matched pair glioblastoma tissue samples, which indicate that both potential therapeutic targets can be targetable in human gliomas. However, larger study cohorts are needed to validate described findings.

Unlike previously published data, CSF1R and TAMs staining distribution analysis revealed no expression difference between primary and recurrent tumour samples. In contrast to these findings, several studies which compared multimodal gene expression profiles of glioblastoma tissue samples before and after treatment showed that tumour features as well as the composition of the TME might change during course of disease(Table 9+Figure 11).[140] Due to several factors including received therapy, tumours face selective pressure in particular during early timepoints of disease.[141] If tumoural subclones which show most fit to evade immunogenic recognition and show resistance towards therapy are selected and expanding inside the tumour, overall prognosis for the patient becomes worse.[61, 141] Additionally, a study of 19 matched glioblastoma tissue pairs showed that genes coding for CD204 and CD163 are significantly enriched in recurrent tissue samples which might indicate higher immunosuppressive characteristics of the TME in recurrent tumours.[140] However, described immunohistochemical results of this work could not reflect these findings by Hudson et al. Both CSF1R and TAM markers (CD204, CD163) are equally present in both tissue types.[108] Moreover, analysis of single pairs shown in Figure 11A reveals that over 50 percent of tumours do not change grade of CSF1R expression. Interestingly, if expression change occurs, mainly CSF1R expression decreases towards relapse (Figure 11A). The change of CSF1R expression positively correlates with CD163 expression changes which are suggestive of decrease of TAM numbers inside these distinct matched pair tissue-samples.[108] Besides CSF1R, expression change analysis concerning PD1/PDL1 and TILs markers confirm tendency of stable TME composition during

course of disease in distinct matched pairs.[108]
Inside the evaluated tissue cohort two treatment modalities were enclosed: radiotherapy alone and radiotherapy followed by adjuvant and concomitant temozolomide therapy after surgery (Figure 5).[10] Grouping according to received therapy as well as grouping by earlier described tissue type showed no differences in CSF1R expression levels (see 3.1.2). This is suggestive that potential CSF1R inhibition as a therapeutic option could be applicable in both primary and recurrent states of disease. Additionally, it seems like standard of care therapy regimes do not alter CSF1R expression levels, which enables wide inclusion criteria for potential CSF1R targeting in clinical study populations. However, the small number of enclosed samples ought to be considered as well as derived conclusions should be confirmed in larger study cohorts.[108]
All in all, presence of CSF1R and PD1/PD-L1 as targets for pharmaceutical inhibition could lead to combination therapeutic approaches because so far monotherapies targeting CSF1R or PD1 in recurrent glioblastoma could not reach experimental endpoints which underline the necessity of combination therapeutic approaches. [53, 90, 108]

After evaluating the presence of CSF1R in human tissue samples, *in vivo* studies focusing on CSF1R inhibition related modification of the TME in the immunocompetent, syngeneic VM/Dk mouse model were performed. Targeting of CSF1R in both preclinical *in vivo* studies and clinical phase I and II trials was mainly executed by the use of small molecule kinase inhibitors targeting the intracellular tyrosinase kinase domain of CSF1R.[89] Unfortunately small molecule kinase inhibitors like PLX3397 or BLZ945 which have been used in preclinical breast cancer and glioma models but also in a clinical phase II study in recurrent glioblastomas have not shown always exclusively CSF1R inhibition.[77, 90, 132] These inhibitors bind other tyrosine kinase receptor motives like c-kit, a receptor mainly expressed on haematopoietic stem cells but also upregulated in several cancer types, too.[89] Unspecific inhibition of tyrosine kinases lead to difficulties concerning evaluating singular effect and consequences of CSF1R inhibition.[89] Therefore in the present study CSF1R was inhibited by an 2G2 antibody which exclusively binds to the extracellular

ligand binding domain of CSF1R as shown by Ries et al.[88] The humanized version of this murine chimeric antibody (RG7155) has shown strong reduction of $CSF1R^+$ macrophages and clinical responses in a phase I trial in diffuse-type giant cell tumours, which characteristically secret high levels of CSF1 and attract large numbers of $CSF1^+$ macrophages.[88] Preliminary experiments in our research group which have been published recently could have shown that anti-CSF1R monotherapy by 2G2 as well as anti-PD1 monotherapy led to a statistically significant delayed onset of neurological symptoms (as defined in Table 5) within the VM/Dk mouse model.[108] However, evaluation of composition of the respective TMEs in IHC revealed limitations concerning comparability because animals which have been treated reached defined endpoint (as described in 2.2.4) at different time points.

Therefore (as described in paragraph 3.2.1), as part of this work an animal experiment was conducted, in which the included experimental animals, which received different treatment regimes, were withdrawn from the experiment on day eighteen after surgery.(Figure 11).[108] Hence, it is possible to study the composition of the TME at the same time point focusing on treatment dependency. In the animal experiment simultaneous combination therapy targeting CSF1R and PD1 was included. The rationale to include a combination therapy regime was based on three main reasons.

First, resistance towards CSF1R inhibition was reported in over 50% of animals in a published work by Quail et al. in an *in vivo* glioma model.[142] Acquired resistance utilized insulin-like growth factor 1 receptor (IGF1R) signalling which was activated by interleukin 4 (IL4) and led to higher intracellular activity of the phosphatidylinositol 3-kinase (PI3K).[142] Explained resistance mechanism supports necessity of combination partner for CSF1R inhibition to prevent acquired therapeutic resistance.

Secondly, reported human tissue samples evaluation showed presence of both targets CSF1R and PD1 in majority of evaluated tissue samples showing consistent expression in both primary and recurrent human glioblastoma samples which reveal potential application of combination approaches in human glioblastoma.[108]

Lastly in 2014 a study revealed that CSF1R inhibition by PLX3397 showed improved efficacy of checkpoint inhibition in a mouse model of pancreatic adenocarcinoma.[137] Moreover, Zhu et al. could show that CSF1R inhibition can educate TAMs towards an anti-tumourgenic phenotype and can improve T cell function inside the TME.[137] Consequently, dual combination improvement might be translated to an preclinical glioma model, too.

As shown in 3.2.2, *ex vivo* IHC of executed animal experiment could reveal composition changes in the glioma-associated microenvironment in all treatment groups in comparison to respective control groups.[108] As shown in Figure 18 reduction of TAM markers CD11b and CD204 could be observed qualitatively after CSF1R inhibition or in combination with anti-PD1 treatment.[108] Marker CD163 showed general weak expression in all treatment groups and was not changed by therapy as illustrated in Figure 17 and Figure 18.[108]TAM survival and attraction to tumours as illustrated in Figure 2 depend on the paracrine CSF1R/CSF1 signalling loop inside the TME of gliomas.[67] Observed findings support earlier published studies focusing on consequences of CSF1R inhibition. As closely studied by Coniglio et al. interaction between glioma cells and tumour-associated macrophages depend on CSF1R/CSF1 and EGF/EGFR1 signalling.[67] Like performed CSF1R inhibition by the 2G2 antibody, inhibition by tyrosine kinase inhibitor PLX3397 executed by Coniglio et al. has revealed reduction of TAM markers and showed decreased invasiveness of glioma cells *in vivo*.[67] Of note, CSF1R inhibition in other preclinical cancer models like pancreas tumours or adeno-colorectal showed reduction of $CD11b^+$ cells, too.[88, 137] Consequently, reported reduction of evaluated markers CD204 and CD11b are highly suggestive of depletion of TAMs inside the TME depending on performed CSF1R inhibition.[108] In contrast treatment group which received single PD1 inhibition could not present changes in TAM numbers which supports dependency of TAMs concerning CSF1R signalling. As other studies have shown up to 30 percent of tumour mass in human glioblastoma consist of TAMs.[63] Moreover, a comprehensive analysis of Komohara et al. has shown that in glioma number of macrophages which express CD204 as a marker for a pro-tumourgenic phenotype correlate with grade of malignancy.[63, 71] Hence,

decrease of CD204 and CD11b *in vivo* can be considered as decrease of malignancy and immune suppression inside the TME.[108]

Besides evaluation of TAM signatures inside the TME, assessment of T cell specific markers by IHC was performed, too. As shown in Figure 15 and Figure 16 performed staining quantification revealed increased number of $CD8^+$ cells and an elevated $CD8^+/CD4^+$-ratio particularly in the anti-CSF1R monotherapy group as well as in combination with anti-PD1 treatment.[108] Interestingly, overall number of $CD3^+$ cells, (generally expressed by T cells), was elevated exclusively in group treated with the 2G2 anti-CSF1R antibody, whereas $CD4^+$cells were slightly increased inside the anti-PD1 treatment group, too.[108] Distribution of T cells shown in Figure 16B presented clear enrichment of stained T cells at tumour borders of animals which have received anti-CSF1R treatment. Staining distribution might be suggestive for T cell attraction towards the tumour mass due to the less immune suppressive microenvironment.
Observed findings show strong similarities in comparison to other studies which either used small molecular inhibitors or the 2G2 antibody for CSF1R inhibition in preclinical models of several tumour entities. In the earlier mentioned study performed by Zhu et al., CSF1R inhibition alone as well as in combination with a checkpoint inhibitor led to both higher numbers of $CD8^+$ cells and overall increase of $CD3^+$ cells in a mouse model of pancreatic adenocarcinoma.[137] Increased $CD8^+/CD4^+$ in combination with higher numbers of $CD3^+$ cells was also found in the fundamental work published by Ries et al., characterizing the used 2G2 antibody and its humanized version RG7155 .[88] Treatment antibody was tested in an MCA1 fibrosarcoma and an adeno-colorectal mouse models showing increased T cell infiltration in FACS analysis, particularly higher number of $CD8^+$ cytotoxic T cells were found which fits to shown IHC quantification shown in Figure 16.[88, 108].Described findings might indicate that CSF1R depending attraction of $CD8^+$ cytotoxic T cells might be another sign for increased immunogenicity of respective TMEs. Particularly interesting in this regard is a study published 2019 which evaluated immune responses after neoadjuvant PD1 immunotherapy in recurrent glioblastomas.[94] Cloughesy et al. could reveal that improved outcomes after neoadjuvant treatment with Pembrolizumab showed

increased numbers of $CD8^+$ cells inside the TME of most patient's which could benefit from immunotherapy.[94] This observation might underline the connection between $CD8^+$ cell infiltration and higher response to checkpoint inhibitions in human glioblastoma.[94] This hypothesis is supported by another study by Zhao et al.. His work included 66 glioblastoma patients who were either responder or non-responder to anti-PD1 therapy. Next, they could reveal longitudinal molecular causes on transcriptomic and genomic level for therapeutic responses.[143] One aspect which were linked to unfavourable response towards nivolumab in a subgroup of PTEN-mutant glioblastoma was the lack of TILs infiltration inside the patient's TME.[143] This might emphasize the importance to attract functional-active TILs towards the TME which might be possible by CSF1R inhibition.[108]

In addition, IHC staining concerning basal features of the tumour cells including proliferation, angiogenesis, invasiveness, and origin were executed. Staining against the proliferation marker Ki67 and endothelial marker CD31 could not show clear difference between treatment and control groups. (Figure 13-14) However, glioma like vessel formation, observed infiltrative growing behaviour as illustrated in Figure 13B confirm representative glioma like characteristics of the used VM/Dk SMA560 glioma mouse model.[108] Despite of the unchanged proliferation profile of tumour cells, quantification of caspase 3 cleaved staining, an apoptosis marker, showed enrichment inside both mono and combination therapy regimes (see Figure 21- 22).Increased staining signal indicate increased occurring apoptosis inside these tumours. Observed caspase 3 cleaved reduction confirms finding in a study targeting CSF1R by BLZ945 in a proneural glioma model.[77] Interestingly a study analysing the expression of caspase 3 cleaved in human gliomas could show that increased staining signal is linked to favourable prognosis and lower tumour grade in human gliomas which might be an interesting aspect for future *in vivo* experiments to study, too.[144] However, performed apoptosis staining cannot distinguish if either TAMs or tumour cells underwent apoptosis in evaluated mouse glioma tissue samples. Nevertheless, caspase 3 signalling as a pathway for microglial translation towards a tumour supporting phenotype have been closely studied inside the glioma-associated

microenvironment, too.[145] *In vitro* co-culture experiments have shown that glioma cells suppress basal levels of caspase 3. Additionally, inhibition of microglial caspase 3 enhanced tumour growth of experimental gliomas *in vivo*.[145]

Evaluation of therapeutic targets PD1 and CSF1R in IHC revealed unchanged presence of PD1 and PDL1 in all groups, whereas CSF1R was slightly reduced after treatment including CSF1R inhibition.(Figure 20) In contrast fundamental work of Pyonteck et al. which have showed polarization changes of TAMs after CSF1R inhibition in several preclinical glioma models could not detect CSF1R expression changes after CSF1R inhibition.[77] In this regard, further studies evaluating the role of PD1 inhibition concerning downregulation of CSF1R after combination therapy might be helpful.

However, synergistic effects of anti-PD1 and anti-CSF1R have not been exclusively tested in preclinical glioma models. Another study in a BRAFV600-driven melanoma model could show that CSF1R inhibition enhances PD1 efficacy and led to improved survival *in vivo*.[146] Enhancing PD1 efficacy or overcoming anti PD1 resistance has not only been tested by combination therapy regimes including anti-CSF1R but also with other targets inside the TME like the C-X-C chemokine receptor type 4 (CXCR-4)/ C-X-C chemokine Ligand 12(CXCL-12) axis. [147]Interestingly Wu et al. could reveal similar post-treatment TME changes like increased CD8/CD4 ratio or improved TILs numbers. Moreover, the study shows modification inside the compartment of regulatory T cells after treatment.[147]

Further immunohistochemical staining of the shown work which is published by Przystal and Becker et al. showed that FoxP3 positive regulatory T cells were significantly decreased after anti-CSF1R therapy, too.[108] This observation is in good agreement with the results presented here and supports the hypothesis that CSF1R inhibition could lead to a re-education of the TME leading to improved immunogenicity.[108] Consequently, CSF1R inhibition generally might help to overcome immunosuppressive characteristics of the glioma-associated microenvironment and might secure better efficacy of checkpoint inhibitors.[49, 107, 108] In context of the performed study another animal experiment focusing

on the onset of neurological symptoms (equally defined as in 2.2.4) was performed as part of the overall project “Targeting of CSF1R” which has been published recently and ought to be discussed.[108] First, monotherapies supported previously performed experiment and showed again improved symptom-free survival (as defined in Table 5) against respective control groups in the VM/Dk mouse model. Additionally, three combination therapy approaches, one simultaneous and two sequential treatment schedules were executed.[108] Combination therapy regimes showed comparable median symptom-free survival as monotherapies. However, analysis of symptom-free survival showed that some animals which have been treated sequentially starting with anti-CSF1R followed by anti-PD1 could strongly benefit from therapy and showed a durable long tail in the Kaplan-Meyer curve as illustrated in Przystal and Becker et al.[108] Nevertheless, the question why only several animals have shown favourable prognosis remained not clearly answered, yet. In this regard there might be further causes which limit synergistic potential of combination regimes consisting of CSF1R and PD1 inhibition. These underlying factors need to be further investigated.[108] However, further experiments performed by one of our collaboration partners using several patient-derived microtumours (PDMs) confirmed potential of CSF1R inhibition in combination with anti-PD1 treatment.[108] Therefore glioblastoma cells and TILs were isolated from intraoperatively resected glioblastoma tissue. Next, cancer cells and TILs were co-cultured and treated with anti-CSF1R and anti-PD1 antibodies. Treatment induced toxicity was measured with a CellTox™ Green Cytotoxicity Assay, additionally PDMs were stained against CSF1R and other TAM markers.[108, 148] PDMs which showed histologic enrichment of CSF1R and presence of TAM markers revealed statistically significant increased cytotoxicity after CSF1R inhibition and highest after combination with anti-PD1 inhibition.[108]

Taken together recomposition of the TME shown in post treatment mouse glioma tissue, in combination with improved symptom-free survival after CSF1R inhibition and increased cytotoxicity in several PDMs after combination strategy including CSF1R and PD1 inhibition might show the translational potential of this therapeutic approach.[108]

A preclinical mouse model which has been frequently used for examining the effects of CSF1R inhibition on the glioma associated microenvironment is a PDGFB–driven glioma mouse model using the RCAS/TVA delivery system as described in Figure 3 and under paragraph 1.3.1.1.[77, 95] In comparison to the VM/Dk mouse model tumours are initiated through somatic gen transfer of an PDGFB amplification into Nestin positive cerebral mouse cells expressing the TVA-receptor.[102] Additionally the mouse strain has a deficit Ink4a-$^{-/-}$background which leads in combination with delivered oncogene PDGFB, often occurring in human glioma which have a pro-neural gene signature, to stable glioblastoma formation.[44, 102, 103] Consequently, the model better reflects the natural course of disease and glioma development and does not depend on orthotopic implantation of syngeneic glioma cells as performed in the VM/Dk model.

First tumour initiation was characterized as summarized in Figure 22. In two independently performed characterization experiments focusing either on MRI/FET-PET imaging or ex vivo IHC analysis tumour median symptom-free survival, defined as reaching endpoints stated in Table 5, were in the range of 38-39 days post DF1 cell implantation.(Figure 24) The described reaching of endpoints is well consistent with the work of Hambardzumyan, who developed the characterized animal model and tested different locations for tumour initiation by PDGFB amplifications.(Figure 24)[102] Interestingly, untreated animals of all three performed animal experiments have shown equal median symptom-free survival which highlights high reproducibility of the mouse model (Figure 24- 31). Pyonteck et al. underlines reproducibility of the model with reported median symptom-free survival of used vehicle control with 39.9 days post-surgery.[77]

Monitoring tumour growth by MRI in the used animal model has been evaluated in contrast to other studies by acquisition of T1 sequences with the contrast agent Gadolinium which is a standard diagnostic tool for evaluating treatment responses in human glioblastoma, too.[28](Figure 25-26) Described imaging modality and evaluation of tumour mass in studies evaluating response to CSF1R inhibition have utilized T2 imaging without contrast agent.[77, 142, 149] Advantage of chosen sequence is the presentation of barrier disorders of the BBB

due to tumour growth, resulting in contrast enhancement which is observed in human high-grade gliomas, too.[24, 28] Imaging revealed quantifiable contrast agent uptake starting on day 25 to day 30 after DF1 cell implantation followed by exponential growth pattern, showing stereotypical radiologic picture of high-grade glioma. (Figure 25- 26) Equally as described by Hambardzumyan, initiated tumours mainly infiltrated the temporal and parietal lobe and presented rare infiltration of the brainstem or the cerebellum.[102] Tumour sizes during day 32 to 39 showed exponential growth behaviour. Inside described time interval tumours reached volume above 40mm^3. Volume of 40mm^3 measured in T2 sequences was used for stratification and grouping in several studies targeting CSF1R. [77, 142, 149]Pyonteck et al. could show that tumours larger than 40mm^3 showed reduced tumour volume after inhibition of CSF1R, whereas tumours between the size 4.5 to 40mm^3 showed stable tumour volume after therapy starting therapy four to five weeks after tumour initiation.[77] Consequently range of reaching stratification volume of 40mm^3 has been reached in the same time frame as described in cited literature.[77, 142, 149] However, it has to be considered that tumour volume measured in T1 images with contrast agent might be even higher in T2 images due to tumour oedema around the tumour lesion.[19, 24, 28] As visible in Figure 25C, H&E staining revealed clear histologic features of glioblastoma including strong neovascularisation, necrosis areas and increased cellular density as mentioned by Hambardzumyan, too,[102] All in all, findings highlight the utility of T1 contrast enhanced imaging as well as confirm the reproducibility of the PDGFB-driven model and its glioma-like characteristics. Next, baseline immunogenicity of the PDGFB-driven model in IHC was evaluated and compared towards the VM/Dk model. Immune cell infiltration was present in both animal models. (Figure 27-28) However, basal infiltration of T cells was higher in the PDGFB-driven mouse model, suggestive for intrinsic higher immunogenicity of developed tumours. However, viral delivery system must be taken into consideration concerning immune reaction towards genes delivered by the RCAS/TVA system. As von Werder et al. mentioned the virus itself shows low immunogenicity but genes transferred by the system might induce inflammatory responses particularly in older mammalians.[101] Of note, PDGFB-driven model

showed higher expression of CD163 as TAM marker, whereas the VM/Dk model presented more basal CD204 expression with an overall lack of CD163 expression.(Figure 28) This difference might be especially interesting because of a study focusing on the immune landscape of the TME in human gliomas. There it could be shown that medium and high CD163 expression in human glioblastomas showed unfavourable prognosis despite of molecular subtypes.[150] Both evaluated glioma mouse models showed intrinsically high expression of proliferation marker Ki67 and showed strong neovascularisation.(Figure 27-28) Particularly the PDGFB-driven model revealed frequent, large vessel formation. This could be explained by the initiation process through PDGFB amplification. PDGFB signalling can lead to enhanced expression of VEGF which directly increases angiogenesis.[102, 151] Additional paracrine effects of PDGF are frequently reported.[102, 151]
Finally, it could be demonstrated that the PDGFB-driven model is suitable for the testing of CSF1R and immune checkpoint inhibitors, has a stable proportion of TAMs in the TME, and the tumours present typical histological and radiological characteristics of human glioblastoma (Figure 25-28).

Thus, the model was used in a second therapy study in the overall project "Targeting of CSF1R". As described in Figure 29, animals were rationed into several mono and combination therapy groups. As mentioned, sequential combination therapies starting with anti-CSF1R followed by anti-PD1 have shown favourable prognosis for some animals in the VM/Dk model.[108] Anti-CSF1R as enhancer for improved efficacy of checkpoint inhibition was evaluated in two different melanoma models by Neubert et al, too. CSF1R inhibition depleted number of TAMs which led to tumour regression by followed immune checkpoint inhibition.[146] In contrast, monotherapy by CSF1R inhibition could not induce tumour mass reduction, as well as immune checkpoint inhibition showed shorter effect of tumour mass reduction in comparison to combination therapy.[146] Despite of the promising observations inside the VM/Dk model and several published studies showing enhanced efficacy of anti-PD1 treatment through CSF1R inhibition, experiment could not show delayed onset of neurological symptoms in combination therapy groups in the PDGFB-driven glioma mouse

model.[137, 146] (Figure 30) In contrast to the expected outcomes, mono therapeutical therapy regimes revealed modest later onset of neurological symptoms (as defined in Table 5) than combination therapy approaches.(Figure 30B) Several reasons for not reaching expected outcomes and highly heterogenous survival inside the treatment groups of the executed experiment can be considered.

First, the PDGFB-driven model shows generally longer time till reaching defined experimental endpoints than in the VM/Dk mouse model (see Table 5). According to the function of the model, tumours are induced through mammalian cells themselves whereas the VM/Dk model depends on syngeneic tumour cell implantation.[96, 102] Concerning these different origins of tumours kinetic of tumoural growth might be different, too. For example, performed MRI/FET-PT showed onset on contrast agent enhancement around day 25 to 28 which revealed exponential growing kinetics, whereas an imaging study using FET-Pet study of GL261 cells implanted into C57BL/6mice tend to show more linear longitudinal tumour growth dynamics, measured by FET uptake, which might show hypothetical better growing kinetic for analysis of targeted therapies.[126]

Secondly, direct comparison towards the principal preclinical study showing strong survival benefits after CSF1R inhibition presents important differences concerning treatment delivery and application pattern. Pyonteck et al. have treated mice with the well-characterized CSF1R tyrosine kinase inhibitor BLZ945 daily till reaching defined endpoints. Long-term survival in over 60 percent of treated XFM animals could be observed.[77] BLZ945 application frequency is consistent in the other published studies focusing either on acquired resistance to CSF1R or efficacy of tyrosine kinase inhibitors in combination with CSF1R inhibition.[142, 149] In contrast in the described study mice have received anti-CSF1R antibody 2G2 twice per week as illustrated in Figure 29. Additionally, BLZ945 was applied by oral gavage whereas 2G2 was applied through IP injection.[77]

Thirdly, most of included animals in the study have not complete planed treatment schedule due to early onset of neurological symptoms. Moreover, strong heterogenous survival inside the treatment groups was observed. Particularly

inside the mono therapy groups minority of animals could benefit from therapy whereas majority could benefit moderately by therapy. (Figure 30)
Taken together, increased dosage or frequency of CSF1R application could be considered as potential pitfall of the experiment.
Overall, the experiment shows a strong reproducibility of untreated glioma development in comparison to previously described pilot experiments, whereas treatment related benefits concerning onset of neurological symptoms were highly heterogeneous. Reasons for difference in treatment responses could not been answered through performed animal experiment and should be tackled in further experiments.

Answering the open question arising through the two treatment studies concerning diverse treatment response, easily accessible imaging modalities might be helpful to evaluate tumour development and tumoural burden after application of treatment modalities. Therefore, CFP and YFP labelling of long-term cell lines was performed. As shown in Figure 32 several cell lines have been successfully labelled. Labelled glioma cell lines enable for the evaluation of tumour size dynamics, and the cells can be used in a wide variety of models use *in vitro* and *in vivo*. Of note, usage of labelled cells in different animal models like the zebrafish model could be considered, too. In particular, the scope of drug screens and dose finding can be implemented within the zebrafish model, as for example a study by Pudelko et al. could demonstrate. [152] Consequently, labelled cells might give the opportunity for evaluating growth dynamics after anti-CSF1R and anti-PD1 inhibition by bioluminescence, too. For instance, a study from Ladomersky et al. testing combination therapies combining anti-PD1 with anti-IDO1 and radiation treatment could evaluate synergistic treatment effects by monitoring tumour growth with bioluminescence imaging in experimental gliomas.[153] Consequently, a wider spectrum of imaging modalities could be beneficial to answer open questions concerning heterogeneous response towards CSF1R inhibition particularly in the PDGFB-driven glioma mouse model.
Another issue which has to be addressed before clinical translation are immune-related adverse events (irAEs) and possible off target effects of CSF1R inhibition. A new spectrum of AEs has been reported after anti-CTLA4 or anti-PD1

treatments. Most occurring irAEs are fatigue, diarrhea, autoimmune colitis or increased liver enzymes.[154, 155] IrAEs are more frequent in combination immunotherapeutic regimes than in monotherapies. [154] Therefore potential combination partners as anti-CSF1R treatment and its possible adverse events profile must be closely evaluated. As described in 1.2.1, CSF1R is essential for neuronal development and is wildly expressed in neural cell lineages.[85] Mutations inside the CSF1R play a crucial role in rare neurological diseases like the adult-onset leukoencephalopathy with axonal spheroids and pigmented glia.[156] Therefore inhibition of CSF1R in particular in the context of brain tumours might cause neurological toxicity, too. So far clinical studies investigating CSF1R inhibition in tumoural diseases most often showed increase of liver enzymes due to depletion of CSF1R-positive Kupffer cells. [88, 107] Generally, preliminary safety reports of phase 1 and 2 studies with CSF1R inhibitors tend towards a favourable safety profile.[88, 107] However, clinical trials focussing on dose finding and titration in context of preventing treatment related neurotoxicity and adverse events are warranted.

To sum up and make the point, the discussed project describes stable presence of CSF1R in matched pair human glioblastoma tissue samples. Histologic post-treatment analysis could show recomposition of the glioma microenvironment including increased TIL attraction and decrease of TAMs in the VM/Dk SMA560 mouse model after CSF1R inhibition and in combination with anti-PD1 blockage.[108] Consequently, the study could illustrate potential of anti-CSF1R for clinical translation probably in combination with anti-PD1. Further experiments in larger study cohorts need to address particularly dosage and timing of anti-CSF1R inhibition and its combination with anti-PD1.[108] Therefore, performed study gives a comprehensive multimodal description of an PDGFB-driven glioma mouse model further preclinical immunotherapeutic approaches. Multimodal characterization gives evidence about tumoural growth kinetics using FET-PET and T1 contrast enhanced MRI scans and highlights high immunogenicity and glioma-like histologic features of the glioma mouse model using the RCAS/TVA delivery system. Executed treatment study using the characterized mouse model could not reveal later onset of neurological symptoms after CSF1R inhibition or

in combination with anti-PD1. However, experiment confirms high reproducibility of tumour formation and its utility for preclinical immunotherapeutic glioma studies. Further experiments focussing on underlying drivers for heterogeneous treatment responses of anti-CSF1R and anti PD1 inhibition probably using multimodal imaging approaches for better assessing treatment response and timing are warranted. Moreover, further clinical studies, especially targeting the timing of therapy and dose finding, are urgently needed for further evaluation of possible treatment induced side-effects.

5 Summary and further prospective

5.1 English summary

One of the most aggressive primary tumours of the central nervous system are glioblastomas. Despite of multimodal therapeutic approaches patient's prognosis of highly selected clinical trial populations is still in the range of 1.5 years. [10-12] Therefore, novel therapeutic strategies are urgently needed.

Therapeutic targeting of the glioblastoma-associated microenvironment is a promising approach in this regard.[49, 61] Particularly macrophages represent a highly abundant population of tumour-infiltrating host cells and are key players of the immune suppressive milieu inside human gliomas.[63, 71] In this regard the colony stimulating factor-1/colony stimulating factor-1 receptor (CSF1/CSF1R) axis plays an important role for macrophage differentiation and survival. [67, 88]

To assess presence of CSF1R in human glioblastoma, CSF1R staining in human tissue samples from primary and recurrent glioblastoma was performed inside the described study and discussed in the context of TME specific histologic markers. For targeting the TME an anti-CSF1R approach using the antibody clone 2G2 in combination with immune checkpoint inhibition by an anti-PD1 antibody was performed in two preclinical glioma mouse models.[88] Composition of the TME after executed treatments was evaluated by immunohistochemistry. Additionally the study includes characterization of a frequent used PDGFB-driven glioma model using the somatic gen transfer system RCAS/TVA by the means of MRI, FET-PET imaging and IHC. [102]

The evaluated target, CSF1R is present in human samples of primary and recurrent glioblastoma. (Table 9)[108] Moreover, analysis show no statistical difference of CSF1R expression linked to received treatment or after first relapse of disease. Use of an established Immunoreactive Score (IRS) confirmed results and pronounced high staining intensity of CSF1R inside evaluated tissue samples.[108] Single case analysis showed that over 50% of cases have stable expression after first relapse with tendency of showing higher CSF1R expression after first diagnosis than after first relapse of disease.(Figure 11)

Monotherapy with anti-CSF1R antibody as well as in combination with anti-PD1

antibody in the syngeneic, immunocompetent VM/Dk mouse model revealed reduction of CD204 and CD11b positive cells in IHCs, which most likely indicate reduction of TAMs inside the TME.[108](Figure 17-18) Simultaneously increased numbers of infiltrated $CD8^+$ cells, higher $CD8^+/CD4^+$ ratios and increased Caspase 3 cleaved signals were observed *in vivo*, suggestive for improved immunogenicity of the treated experimental gliomas and recomposition of the TME depending on CSF1R inhibition. (Figure 15-16+ 20-21)

Characterization of the pro-neural glioma model using the RCAS/TVA delivery system could reveal stable tumour formation *in vivo*, showing high reproductivity in regard of onset of neurological symptoms as defined in Table 5. Monitoring tumour growth by MRI present first contrast agent enhancement starting at day 25 to day 30 after surgery, followed by exponential growth dynamics going hand in hand with FET accumulation.(Figure 25) TME consisting of TAMs, particularly $CD163^+$ and $CD204^+$ cells in combination with basal infiltration of T cells was observed in untreated ex vivo experimental glioma samples. (Figure 27-28)

However, anti-CSF1R approach could not repeat observed later onset of neurological symptoms (as defined in Table 5) in combination treatment regimens as in the VM/DK model has shown before.(Figure 30) In contrast several animals treated exclusively with anti CSF1R or anti-PD1 showed prolonged time till reaching defined endpoints, building a long tail inside the Kaplan-Meyer curve.

Taking all results together and considering the other published results by Przystal and Becker et al., CSF1R is identified as a promising therapeutic target for glioblastoma, probably in combination with PD1 inhibition.[108] However, further studies concerning the question why only some animals per combination treatment show favourable prognosis ought to be addressed, in particularly inside the characterized PDGFB-driven glioma model using the somatic gen transfer system RCAS/TVA. Before clinical translation, it also needs further data to evaluate anti-CSF1R antibody tolerability and toxicity in combination with anti-PD1. Therefore, further clinical studies, especially targeting the timing of therapy and dose finding, are urgently needed for further evaluation.

5.2 German summary

Das Glioblastom ist ein aggressiver primärer Tumor des Zentralnervensystems. Das mediane Gesamtüberleben der Patienten liegt selbst in ausgewählten klinischen Studienpopulationen, im Bereich von 1,5 Jahren. [10-12] Daher sind dringend neue therapeutische Strategien erforderlich.
Ein vielversprechender Ansatz in dieser Hinsicht ist das Gliom-assoziierte Mikromilieu.[61, 71] Insbesondere Makrophagen stellen eine sehr zellreiche Population tumorinfiltrierender Wirtszellen dar und spielen eine Schlüsselrolle im immunsuppressiven Milieu innerhalb menschlicher Gliome.[63, 71] Dabei spielt die Interaktion zwischen dem Kolonie-stimulierende Faktor-1/Kolonie-stimulierende Faktor-1-Rezeptor (CSF1/CSF1R) eine entscheidende Rolle für die Differenzierung und das Überleben der Makrophagen. [67, 88]

Um das Vorhandensein von CSF1R im menschlichen Glioblastomen zu evaluieren, wurde im Rahmen der beschriebenen Arbeit immunhistochemische Färbungen von CSF1R in menschlichen Gewebeproben von primären und rezidivierenden Glioblastomen erstellt und im Zusammenhang mit spezifischen histologischen Markern diskutiert. Um das Tumormikromilieu therapeutisch anzuvisieren, wurde ein anti-CSF1R-Ansatz unter Verwendung des Antikörperklons 2G2 in Kombination mit einem anti-PD1 Immuncheckpointinhibitor in zwei präklinischen Gliom-Mausmodellen getestet.[102] Die Zusammensetzung des Tumormikromilieu nach durchgeführten Behandlungen wurde mittels Immunhistochemie evaluiert. Zusätzlich umfasst die gezeigte Arbeit die Charakterisierung eines häufig verwendeten pro-neuralen Gliom Mausmodelles unter Verwendung des somatischen Gen-Transfer-Systems RCAS/TVA mittels MRT, FET-PET-Bildgebung und immunhistochemischer Gewebsanalyse.[102]

Der evaluierte Kolonie-stimulierende Faktor-1-Rezeptor liegt in menschlichen Proben von primären und rezidivierenden Glioblastomen vor. Darüber hinaus lässt sich kein statistischer Unterschied der CSF1R Expression in Verbindung mit der erhaltenen Behandlung oder nach dem ersten Krankheitsschub feststellen.(Table 9) Die Verwendung eines etablierten Immunoreactive Scores (IRS) bestätigte die Ergebnisse und zeigte die hohe Färbeintensität von CSF1R

in den untersuchten Gewebeproben.(Figure 10) Die Einzelfallanalyse zeigt, dass über 50% der Fälle nach dem ersten Rezidiv eine stabile CSF1R Expression aufweisen mit der Tendenz, eher nach der Erstdiagnose eine höhere CSF1R Expression zu zeigen als nach dem ersten Rezidiv.(Figure 11)

Die Monotherapie mit dem anti-CSF1R-Antikörper sowie in Kombination mit dem anti-PD1-Antikörper im syngenen, immunkompetenten VM/Dk-Mausmodell zeigt eine Reduktion von CD204- und CD11b-positiven Zellen in der Immunhistochemie, was höchstwahrscheinlich auf eine Reduktion der TAMs innerhalb des Gliom-assoziierten Mikromilieus hinweist.(Figure 18+21) Gleichzeitig wurden *in vivo* eine erhöhte Anzahl infiltrierter $CD8^+$-Zellen, ein höheres $CD8^+/CD4^+$-Verhältnis und ein erhöhtes „caspase 3-cleaved“ Signal beobachtet, was auf eine erhöhte Immunogenität der behandelten experimentellen Gliome und eine Neuzusammensetzung des Tumormilieus in Abhängigkeit von der CSF1R-Inhibition hindeutet.(Figure 16) [108]

Die Charakterisierung des pro-neuralen Gliom Mausmodelles unter Verwendung des RCAS/TVA-Systems zeigte eine stabile Tumorformation *in vivo*, einhergehend mit einer hohen Reproduzierbarkeit hinsichtlich des Erreichens der experimentellen Endpunkte, wie in Tabelle 5 definiert. Die Überwachung des Tumorwachstums mittels MRT zeigt erste Kontrastmittelaufnahme ab Tag 25 bis Tag 30 nach Tumorinduktion, gefolgt von einer exponentiellen tumoralen Wachstumsdynamik, die auch im FET-PET erkennbar ist. (Figure 25) Immunhistochemisch zeigt sich ein Tumormikromilieu mit vielen tumor-assoziierten Makrophagen, die Expression von CD163 und CD204 aufweisen. Zudem zeigt sich eine erhöhte basale Infiltration von T-Zellen im Vergleich zum VM/Dk Mausmodell. (Figure 27-28)

Allerdings konnte der anti-CSF1R-Ansatz das spätere Erreichen der festgelegten Versuchsendpunkte (wie in Tabelle 5 definiert) in Kombinationsbehandlungs-Schemata nicht, wie im VM/DK-Modell zuvor festgestellt, beobachten.(Figure 30) Im Gegensatz dazu zeigten einige Tiere, die ausschließlich mit anti-CSF1R oder anti-PD1 behandelt wurden, eine verlängerte Zeit bis zum Erreichen der definierten Versuchsendpunkte.

In Zusammenschau der in dieser Arbeit gezeigten Ergebnisse unter Berücksichtigung der von Przystal und Becker et al. publizierten Behandlungsstudien konnte CSF1R als vielversprechendes therapeutisches Ziel im Glioblastom, wahrscheinlich in Kombination mit einer PD1-Inhibition, identifiziert werden.[108] Weitere Studien zu der Frage, warum nur einige, wenige Tiere von der Kombinationstherapie profitieren, sollte im Weiteren adressiert werden, insbesondere innerhalb des charakterisierten pro-neuralen Gliom Mausmodelles mit dem somatischen Gen-Transfer-System RCAS/TVA. Vor der klinischen Translation und Testung in klinischen Studien, benötigt es zudem weitere Daten zur Evaluation der anti-CSF1R Antikörper Verträglichkeit und Toxizität in Kombination mit anti-PD1.

Daher sind weitere klinische Studien, die vor allem den Therapiezeitpunkt und die Dosisfindung ins Auge fassen, zur weiteren Evaluation dringend notwendig.

6 References

1. Louis, D.N., et al., *The 2016 World Health Organization Classification of Tumors of the Central Nervous System: a summary.* Acta Neuropathol, 2016. **131**(6): p. 803-20.
2. Wen, P.Y. and S. Kesari, *Malignant Gliomas in Adults.* New England Journal of Medicine, 2008. **359**(5): p. 492-507.
3. Ostrom, Q.T., et al., *CBTRUS Statistical Report: Primary Brain and Other Central Nervous System Tumors Diagnosed in the United States in 2011-2015.* Neuro Oncol, 2018. **20**(suppl_4): p. iv1-iv86.
4. Weller, M., et al., *Glioma.* Nature Reviews Disease Primers, 2015. **1**(1): p. 15017.
5. Molinaro, A.M., et al., *Genetic and molecular epidemiology of adult diffuse glioma.* Nat Rev Neurol, 2019. **15**(7): p. 405-417.
6. Pajtler, K.W., et al., *Molecular Classification of Ependymal Tumors across All CNS Compartments, Histopathological Grades, and Age Groups.* Cancer Cell, 2015. **27**(5): p. 728-43.
7. Ostrom, Q.T., et al., *Adult Glioma Incidence and Survival by Race or Ethnicity in the United States From 2000 to 2014.* JAMA Oncol, 2018. **4**(9): p. 1254-1262.
8. Gilbert, M.R., et al., *A randomized trial of bevacizumab for newly diagnosed glioblastoma.* N Engl J Med, 2014. **370**(8): p. 699-708.
9. Gilbert, M.R., et al., *Dose-dense temozolomide for newly diagnosed glioblastoma: a randomized phase III clinical trial.* J Clin Oncol, 2013. **31**(32): p. 4085-91.
10. Stupp, R., et al., *Radiotherapy plus concomitant and adjuvant temozolomide for glioblastoma.* N Engl J Med, 2005. **352**(10): p. 987-96.
11. Chinot, O.L., et al., *Bevacizumab plus radiotherapy-temozolomide for newly diagnosed glioblastoma.* N Engl J Med, 2014. **370**(8): p. 709-22.
12. Stupp, R., et al., *Effect of Tumor-Treating Fields Plus Maintenance Temozolomide vs Maintenance Temozolomide Alone on Survival in Patients With Glioblastoma: A Randomized Clinical Trial.* JAMA, 2017. **318**(23): p. 2306-2316.
13. Lee, J.H., et al., *Human glioblastoma arises from subventricular zone cells with low-level driver mutations.* Nature, 2018. **560**(7717): p. 243-247.
14. Alcantara Llaguno, S., et al., *Cell-of-origin susceptibility to glioblastoma formation declines with neural lineage restriction.* Nat Neurosci, 2019. **22**(4): p. 545-555.
15. Rice, T., et al., *Understanding inherited genetic risk of adult glioma - a review.* Neurooncol Pract, 2016. **3**(1): p. 10-16.
16. Melin, B.S., et al., *Genome-wide association study of glioma subtypes identifies specific differences in genetic susceptibility to glioblastoma and non-glioblastoma tumors.* Nat Genet, 2017. **49**(5): p. 789-794.
17. Wang, L.E., et al., *Polymorphisms of DNA repair genes and risk of glioma.* Cancer Res, 2004. **64**(16): p. 5560-3.
18. Pearce, M.S., et al., *Radiation exposure from CT scans in childhood and subsequent risk of leukaemia and brain tumours: a retrospective cohort study.* Lancet, 2012. **380**(9840): p. 499-505.

19. Weller, M., et al., *European Association for Neuro-Oncology (EANO) guideline on the diagnosis and treatment of adult astrocytic and oligodendroglial gliomas.* The Lancet Oncology, 2017. **18**(6): p. e315-e329.
20. M, I.J.-K., et al., *Prevalence of symptoms in glioma patients throughout the disease trajectory: a systematic review.* J Neurooncol, 2018. **140**(3): p. 485-496.
21. Folstein, M.F., S.E. Folstein, and P.R. McHugh, *"Mini-mental state". A practical method for grading the cognitive state of patients for the clinician.* J Psychiatr Res, 1975. **12**(3): p. 189-98.
22. Orr, S.T. and J. Aisner, *Performance status assessment among oncology patients: a review.* Cancer Treat Rep, 1986. **70**(12): p. 1423-9.
23. Weller, M., et al., *EANO guidelines on the diagnosis and treatment of diffuse gliomas of adulthood.* Nat Rev Clin Oncol, 2021. **18**(3): p. 170-186.
24. Ellingson, B.M., et al., *Consensus recommendations for a standardized Brain Tumor Imaging Protocol in clinical trials.* Neuro Oncol, 2015. **17**(9): p. 1188-98.
25. Wesseling, P., et al., *Quantitative analysis of microvascular changes in diffuse astrocytic neoplasms with increasing grade of malignancy.* Human Pathology, 1998. **29**(4): p. 352-358.
26. Schmainda, K.M., *Diffusion-weighted MRI as a biomarker for treatment response in glioma.* CNS oncology, 2012. **1**(2): p. 169-180.
27. Albert, N.L., et al., *Response Assessment in Neuro-Oncology working group and European Association for Neuro-Oncology recommendations for the clinical use of PET imaging in gliomas.* Neuro Oncol, 2016. **18**(9): p. 1199-208.
28. Law, I., et al., *Joint EANM/EANO/RANO practice guidelines/SNMMI procedure standards for imaging of gliomas using PET with radiolabelled amino acids and [(18)F]FDG: version 1.0.* Eur J Nucl Med Mol Imaging, 2019. **46**(3): p. 540-557.
29. Omuro, A.M., et al., *Pitfalls in the diagnosis of brain tumours.* Lancet Neurol, 2006. **5**(11): p. 937-48.
30. Louis, D.N., et al., *The 2007 WHO classification of tumours of the central nervous system.* Acta neuropathologica, 2007. **114**(2): p. 97-109.
31. van den Bent, M.J., *Interobserver variation of the histopathological diagnosis in clinical trials on glioma: a clinician's perspective.* Acta neuropathologica, 2010. **120**(3): p. 297-304.
32. Cohen, A.L., S.L. Holmen, and H. Colman, *IDH1 and IDH2 mutations in gliomas.* Curr Neurol Neurosci Rep, 2013. **13**(5): p. 345.
33. Noushmehr, H., et al., *Identification of a CpG island methylator phenotype that defines a distinct subgroup of glioma.* Cancer Cell, 2010. **17**(5): p. 510-22.
34. Jenkins, R.B., et al., *A t(1;19)(q10;p10) Mediates the Combined Deletions of 1p and 19q and Predicts a Better Prognosis of Patients with Oligodendroglioma.* Cancer Research, 2006. **66**(20): p. 9852.
35. Pekmezci, M., et al., *Adult infiltrating gliomas with WHO 2016 integrated diagnosis: additional prognostic roles of ATRX and TERT.* Acta neuropathologica, 2017. **133**(6): p. 1001-1016.

36. Hegi, M.E., et al., *MGMT Gene Silencing and Benefit from Temozolomide in Glioblastoma.* New England Journal of Medicine, 2005. **352**(10): p. 997-1003.
37. Weller, M., et al., *MGMT Promoter Methylation Is a Strong Prognostic Biomarker for Benefit from Dose-Intensified Temozolomide Rechallenge in Progressive Glioblastoma: The DIRECTOR Trial.* Clin Cancer Res, 2015. **21**(9): p. 2057-64.
38. Stupp, R., et al., *Effects of radiotherapy with concomitant and adjuvant temozolomide versus radiotherapy alone on survival in glioblastoma in a randomised phase III study: 5-year analysis of the EORTC-NCIC trial.* The Lancet Oncology, 2009. **10**(5): p. 459-466.
39. Capper, D., et al., *DNA methylation-based classification of central nervous system tumours.* Nature, 2018. **555**(7697): p. 469-474.
40. Schwartzentruber, J., et al., *Driver mutations in histone H3.3 and chromatin remodelling genes in paediatric glioblastoma.* Nature, 2012. **482**(7384): p. 226-31.
41. Louis, D.N., et al., *Announcing cIMPACT-NOW: the Consortium to Inform Molecular and Practical Approaches to CNS Tumor Taxonomy.* Acta Neuropathol, 2017. **133**(1): p. 1-3.
42. Ellison, D.W., et al., *cIMPACT-NOW update 4: diffuse gliomas characterized by MYB, MYBL1, or FGFR1 alterations or BRAF(V600E) mutation.* Acta Neuropathol, 2019. **137**(4): p. 683-687.
43. Verhaak, R.G., et al., *Integrated genomic analysis identifies clinically relevant subtypes of glioblastoma characterized by abnormalities in PDGFRA, IDH1, EGFR, and NF1.* Cancer Cell, 2010. **17**(1): p. 98-110.
44. Brennan, C.W., et al., *The somatic genomic landscape of glioblastoma.* Cell, 2013. **155**(2): p. 462-77.
45. Phillips, H.S., et al., *Molecular subclasses of high-grade glioma predict prognosis, delineate a pattern of disease progression, and resemble stages in neurogenesis.* Cancer Cell, 2006. **9**(3): p. 157-73.
46. Vogelstein, B., et al., *Cancer genome landscapes.* Science, 2013. **339**(6127): p. 1546-58.
47. van den Bent, M.J., et al., *Adjuvant and concurrent temozolomide for 1p/19q non-co-deleted anaplastic glioma (CATNON; EORTC study 26053-22054): second interim analysis of a randomised, open-label, phase 3 study.* The Lancet Oncology, 2021. **22**(6): p. 813-823.
48. Stummer, W., et al., *Fluorescence-guided surgery with 5-aminolevulinic acid for resection of malignant glioma: a randomised controlled multicentre phase III trial.* The Lancet Oncology, 2006. **7**(5): p. 392-401.
49. Le Rhun, E., et al., *Molecular targeted therapy of glioblastoma.* Cancer Treat Rev, 2019. **80**: p. 101896.
50. Herrlinger, U., et al., *Lomustine-temozolomide combination therapy versus standard temozolomide therapy in patients with newly diagnosed glioblastoma with methylated MGMT promoter (CeTeG/NOA–09): a randomised, open-label, phase 3 trial.* The Lancet, 2019. **393**(10172): p. 678-688.
51. Wick, W., et al., *Lomustine and Bevacizumab in Progressive Glioblastoma.* N Engl J Med, 2017. **377**(20): p. 1954-1963.

52. Wolchok, J.D., et al., *Nivolumab plus ipilimumab in advanced melanoma.* N Engl J Med, 2013. **369**(2): p. 122-33.
53. Filley, A.C., M. Henriquez, and M. Dey, *Recurrent glioma clinical trial, CheckMate-143: the game is not over yet.* Oncotarget, 2017. **8**(53): p. 91779-91794.
54. Reardon, D.A., et al., *Effect of Nivolumab vs Bevacizumab in Patients With Recurrent Glioblastoma: The CheckMate 143 Phase 3 Randomized Clinical Trial.* JAMA Oncol, 2020. **6**(7): p. 1003-1010.
55. Aldape, K., et al., *Challenges to curing primary brain tumours.* Nat Rev Clin Oncol, 2019.
56. Weller, M., et al., *Vaccine-based immunotherapeutic approaches to gliomas and beyond.* Nat Rev Neurol, 2017. **13**(6): p. 363-374.
57. Hilf, N., et al., *Actively personalized vaccination trial for newly diagnosed glioblastoma.* Nature, 2019. **565**(7738): p. 240-245.
58. Quail, D.F. and J.A. Joyce, *Microenvironmental regulation of tumor progression and metastasis.* Nat Med, 2013. **19**(11): p. 1423-37.
59. Gallagher, B., et al., *Cancer incidence in New York State acquired immunodeficiency syndrome patients.* Am J Epidemiol, 2001. **154**(6): p. 544-56.
60. Grivennikov, S.I., F.R. Greten, and M. Karin, *Immunity, inflammation, and cancer.* Cell, 2010. **140**(6): p. 883-899.
61. Quail, D.F. and J.A. Joyce, *The Microenvironmental Landscape of Brain Tumors.* Cancer Cell, 2017. **31**(3): p. 326-341.
62. Kowal, J., M. Kornete, and J.A. Joyce, *Re-education of macrophages as a therapeutic strategy in cancer.* Immunotherapy, 2019. **11**(8): p. 677-689.
63. Hambardzumyan, D., D.H. Gutmann, and H. Kettenmann, *The role of microglia and macrophages in glioma maintenance and progression.* Nature Neuroscience, 2016. **19**(1): p. 20-27.
64. Murphy, K., Travers, P., Walport, M., & Janeway, *Janeway's immunobiology.* Garland Science, 2012.
65. Gentek, R., K. Molawi, and M.H. Sieweke, *Tissue macrophage identity and self-renewal.* Immunological Reviews, 2014. **262**(1): p. 56-73.
66. Kurahara, H., et al., *Significance of M2-polarized tumor-associated macrophage in pancreatic cancer.* J Surg Res, 2011. **167**(2): p. e211-9.
67. Coniglio, S.J., et al., *Microglial stimulation of glioblastoma invasion involves epidermal growth factor receptor (EGFR) and colony stimulating factor 1 receptor (CSF-1R) signaling.* Mol Med, 2012. **18**: p. 519-27.
68. Goswami, S., et al., *Macrophages Promote the Invasion of Breast Carcinoma Cells via a Colony-Stimulating Factor-1/Epidermal Growth Factor Paracrine Loop.* Cancer Research, 2005. **65**(12): p. 5278.
69. Louveau, A., et al., *Structural and functional features of central nervous system lymphatic vessels.* Nature, 2015. **523**(7560): p. 337-41.
70. Graeber, M.B., B.W. Scheithauer, and G.W. Kreutzberg, *Microglia in brain tumors.* Glia, 2002. **40**(2): p. 252-259.
71. Komohara, Y., et al., *Possible involvement of the M2 anti-inflammatory macrophage phenotype in growth of human gliomas.* J Pathol, 2008. **216**(1): p. 15-24.

72. Simmons, G.W., et al., *Neurofibromatosis-1 heterozygosity increases microglia in a spatially and temporally restricted pattern relevant to mouse optic glioma formation and growth.* J Neuropathol Exp Neurol, 2011. **70**(1): p. 51-62.
73. Parney, I.F., J.S. Waldron, and A.T. Parsa, *Flow cytometry and in vitro analysis of human glioma-associated macrophages. Laboratory investigation.* J Neurosurg, 2009. **110**(3): p. 572-82.
74. Mantovani, A., et al., *Macrophage polarization: tumor-associated macrophages as a paradigm for polarized M2 mononuclear phagocytes.* Trends Immunol, 2002. **23**(11): p. 549-55.
75. Zeiner, P.S., et al., *MIF Receptor CD74 is Restricted to Microglia/Macrophages, Associated with a M1-Polarized Immune Milieu and Prolonged Patient Survival in Gliomas.* Brain Pathology, 2015. **25**(4): p. 491-504.
76. Sica, A., et al., *Tumour-associated macrophages are a distinct M2 polarised population promoting tumour progression: Potential targets of anti-cancer therapy.* European Journal of Cancer, 2006. **42**(6): p. 717-727.
77. Pyonteck, S.M., et al., *CSF-1R inhibition alters macrophage polarization and blocks glioma progression.* Nat Med, 2013. **19**(10): p. 1264-72.
78. Szulzewsky, F., et al., *Glioma-associated microglia/macrophages display an expression profile different from M1 and M2 polarization and highly express Gpnmb and Spp1.* PLoS One, 2015. **10**(2): p. e0116644.
79. Zhou, W., et al., *Periostin secreted by glioblastoma stem cells recruits M2 tumour-associated macrophages and promotes malignant growth.* Nat Cell Biol, 2015. **17**(2): p. 170-82.
80. Hussain, S.F., et al., *The role of human glioma-infiltrating microglia/macrophages in mediating antitumor immune responses1.* Neuro-Oncology, 2006. **8**(3): p. 261-279.
81. Feng, X., et al., *Loss of CX3CR1 increases accumulation of inflammatory monocytes and promotes gliomagenesis.* Oncotarget; Vol 6, No 17, 2015.
82. van den Broek, T., J.A.M. Borghans, and F. van Wijk, *The full spectrum of human naive T cells.* Nature Reviews Immunology, 2018. **18**(6): p. 363-373.
83. Wherry, E.J., *T cell exhaustion.* Nat Immunol, 2011. **12**(6): p. 492-9.
84. Berghoff, A.S., et al., *Programmed death ligand 1 expression and tumor-infiltrating lymphocytes in glioblastoma.* Neuro Oncol, 2015. **17**(8): p. 1064-75.
85. Chitu, V., et al., *Emerging Roles for CSF-1 Receptor and its Ligands in the Nervous System.* Trends Neurosci, 2016. **39**(6): p. 378-393.
86. Wei, S., et al., *Functional overlap but differential expression of CSF-1 and IL-34 in their CSF-1 receptor-mediated regulation of myeloid cells.* J Leukoc Biol, 2010. **88**(3): p. 495-505.
87. Dagher, N.N., et al., *Colony-stimulating factor 1 receptor inhibition prevents microglial plaque association and improves cognition in 3xTg-AD mice.* Journal of Neuroinflammation, 2015. **12**(1): p. 139.
88. Ries, C.H., et al., *Targeting tumor-associated macrophages with anti-CSF-1R antibody reveals a strategy for cancer therapy.* Cancer Cell, 2014. **25**(6): p. 846-59.

89. Ries, C.H., et al., *CSF-1/CSF-1R targeting agents in clinical development for cancer therapy.* Curr Opin Pharmacol, 2015. **23**: p. 45-51.
90. Butowski, N., et al., *Orally administered colony stimulating factor 1 receptor inhibitor PLX3397 in recurrent glioblastoma: an Ivy Foundation Early Phase Clinical Trials Consortium phase II study.* Neuro Oncol, 2016. **18**(4): p. 557-64.
91. Boussiotis, V.A., *Molecular and Biochemical Aspects of the PD-1 Checkpoint Pathway.* N Engl J Med, 2016. **375**(18): p. 1767-1778.
92. Hodi, F.S., et al., *Improved survival with ipilimumab in patients with metastatic melanoma.* N Engl J Med, 2010. **363**(8): p. 711-23.
93. Power, T. *Bristol Myers Squibb Announces Update on Phase 3 CheckMate -548 Trial Evaluating Patients with Newly Diagnosed MGMT-Methylated Glioblastoma Multiforme*. 2020 [cited 2021 09.06.2021]; Available from: https://investors.bms.com/iframes/press-releases/press-release-details/2020/Bristol-Myers-Squibb-Announces-Update-on-Phase-3-CheckMate--548-Trial-Evaluating-Patients-with-Newly-Diagnosed-MGMT-Methylated-Glioblastoma-Multiforme/default.aspx.
94. Cloughesy, T.F., et al., *Neoadjuvant anti-PD-1 immunotherapy promotes a survival benefit with intratumoral and systemic immune responses in recurrent glioblastoma.* Nat Med, 2019. **25**(3): p. 477-486.
95. Stylli, S.S., et al., *Mouse models of glioma.* J Clin Neurosci, 2015. **22**(4): p. 619-26.
96. Oh, T., et al., *Immunocompetent murine models for the study of glioblastoma immunotherapy.* J Transl Med, 2014. **12**: p. 107.
97. Ausman, J.I., W.R. Shapiro, and D.P. Rall, *Studies on the chemotherapy of experimental brain tumors: development of an experimental model.* Cancer Res, 1970. **30**(9): p. 2394-400.
98. Sampson, J.H., et al., *Characterization of a spontaneous murine astrocytoma and abrogation of its tumorigenicity by cytokine secretion.* Neurosurgery, 1997. **41**(6): p. 1365-72; discussion 1372-3.
99. Lee, J., et al., *Tumor stem cells derived from glioblastomas cultured in bFGF and EGF more closely mirror the phenotype and genotype of primary tumors than do serum-cultured cell lines.* Cancer Cell, 2006. **9**(5): p. 391-403.
100. Patrizii, M., et al., *Utility of Glioblastoma Patient-Derived Orthotopic Xenografts in Drug Discovery and Personalized Therapy.* Frontiers in oncology, 2018. **8**: p. 23-23.
101. von Werder, A., et al., *Production of avian retroviruses and tissue-specific somatic retroviral gene transfer in vivo using the RCAS/TVA system.* Nat Protoc, 2012. **7**(6): p. 1167-83.
102. Hambardzumyan, D., et al., *Modeling Adult Gliomas Using RCAS/t-va Technology.* Translational Oncology, 2009. **2**(2): p. 89-IN6.
103. Tchougounova, E., et al., *Loss of Arf causes tumor progression of PDGFB-induced oligodendroglioma.* Oncogene, 2007. **26**(43): p. 6289-96.
104. Serrano, M., et al., *Role of the INK4a locus in tumor suppression and cell mortality.* Cell, 1996. **85**(1): p. 27-37.
105. Dai, C., et al., *PDGF autocrine stimulation dedifferentiates cultured astrocytes and induces oligodendrogliomas and oligoastrocytomas from*

neural progenitors and astrocytes in vivo. Genes Dev, 2001. **15**(15): p. 1913-25.
106. Wainwright, D.A., et al., *Durable Therapeutic Efficacy Utilizing Combinatorial Blockade against IDO, CTLA-4, and PD-L1 in Mice with Brain Tumors.* Clinical Cancer Research, 2014. **20**(20): p. 5290-5301.
107. Cannarile, M.A., et al., *Colony-stimulating factor 1 receptor (CSF1R) inhibitors in cancer therapy.* J Immunother Cancer, 2017. **5**(1): p. 53.
108. Przystal, J.M., et al., *Targeting CSF1R Alone or in Combination with PD1 in Experimental Glioma.* Cancers, 2021. **13**(10).
109. Richard D.Serano, C.N.P.a.D.D.B., *Tumorigenic cell culture lines from a spontaneous VM/Dk murine astrocytoma (SMA).* Acta Neuropathol, 1980: p. 51-53.
110. Huse, J.T. and E.C. Holland, *Genetically engineered mouse models of brain cancer and the promise of preclinical testing.* Brain Pathol, 2009. **19**(1): p. 132-43.
111. Giard, D.J., et al., *In vitro cultivation of human tumors: establishment of cell lines derived from a series of solid tumors.* J Natl Cancer Inst, 1973. **51**(5): p. 1417-23.
112. Himly, M., et al., *The DF-1 Chicken Fibroblast Cell Line: Transformation Induced by Diverse Oncogenes and Cell Death Resulting from Infection by Avian Leukosis Viruses.* Virology, 1998. **248**(2): p. 295-304.
113. Ausman, J.I., W.R. Shapiro, and D.P. Rall, *Studies on the Chemotherapy of Experimental Brain Tumors: Development of an Experimental Model.* 1970. **30**(9): p. 2394-2400.
114. Diserens, A.C., et al., *Characterization of an established human malignant glioma cell line: LN-18.* Acta Neuropathol, 1981. **53**(1): p. 21-8.
115. Studer, A., et al., *Characterization of four human malignant glioma cell lines.* 1985. **66**(3): p. 208-217.
116. Klein, R., et al., *WPRE-mediated enhancement of gene expression is promoter and cell line specific.* Gene, 2006. **372**: p. 153-61.
117. Rahman, M., et al., *Analysis of immunobiologic markers in primary and recurrent glioblastoma.* J Neurooncol, 2018.
118. Ek, S., et al., *From gene expression analysis to tissue microarrays: a rational approach to identify therapeutic and diagnostic targets in lymphoid malignancies.* Mol Cell Proteomics, 2006. **5**(6): p. 1072-81.
119. Martin-Moreno, A.M., et al., *CSF1R Protein Expression in Reactive Lymphoid Tissues and Lymphoma: Its Relevance in Classical Hodgkin Lymphoma.* PLoS One, 2015. **10**(6): p. e0125203.
120. Tuominen, V.J., et al., *ImmunoRatio: a publicly available web application for quantitative image analysis of estrogen receptor (ER), progesterone receptor (PR), and Ki-67.* 2010. **12**(4): p. R56.
121. Meyerholz, D.K. and A.P. Beck, *Principles and approaches for reproducible scoring of tissue stains in research.* Lab Invest, 2018. **98**(7): p. 844-855.
122. Remmele, W. and H.E. Stegner, *[Recommendation for uniform definition of an immunoreactive score (IRS) for immunohistochemical estrogen receptor detection (ER-ICA) in breast cancer tissue].* Pathologe, 1987. **8**(3): p. 138-40.

123. Langford, D.J., et al., *Coding of facial expressions of pain in the laboratory mouse.* Nat Methods, 2010. **7**(6): p. 447-9.
124. Gage, G.J., D.R. Kipke, and W. Shain, *Whole Animal Perfusion Fixation for Rodents.* Journal of Visualized Experiments, 2012(65).
125. la Fougere, C., et al., *Molecular imaging of gliomas with PET: Opportunities and limitations.* Neuro-Oncology, 2011. **13**(8): p. 806-819.
126. Holzgreve, A., et al., *Monitoring of Tumor Growth with [(18)F]-FET PET in a Mouse Model of Glioblastoma: SUV Measurements and Volumetric Approaches.* Front Neurosci, 2016. **10**: p. 260.
127. Mannheim, J.G., et al., *Quantification accuracy and partial volume effect in dependence of the attenuation correction of a state-of-the-art small animal PET scanner.* Phys Med Biol, 2012. **57**(12): p. 3981-93.
128. Heimberger, A.B., et al., *Bone marrow-derived dendritic cells pulsed with tumor homogenate induce immunity against syngeneic intracerebral glioma.* Journal of Neuroimmunology, 2000. **103**(1): p. 16-25.
129. Bos, P.D., et al., *Transient regulatory T cell ablation deters oncogene-driven breast cancer and enhances radiotherapy.* J Exp Med, 2013. **210**(11): p. 2435-66.
130. Eng, L.F., *Glial fibrillary acidic protein (GFAP): the major protein of glial intermediate filaments in differentiated astrocytes.* Journal of Neuroimmunology, 1985. **8**: p. 203-214.
131. Chen, Z., et al., *Cellular and Molecular Identity of Tumor-Associated Macrophages in Glioblastoma.* Cancer Res, 2017. **77**(9): p. 2266-2278.
132. DeNardo, D.G., et al., *Leukocyte complexity predicts breast cancer survival and functionally regulates response to chemotherapy.* Cancer Discov, 2011. **1**(1): p. 54-67.
133. Fujimoto, M., et al., *CD19 regulates B lymphocyte responses to transmembrane signals.* Seminars in Immunology, 1998. **10**(4): p. 267-277.
134. Tedder, T.F. and P. Engel, *CD20: a regulator of cell-cycle progression of B lymphocytes.* Immunology Today, 1994. **15**(9): p. 450-454.
135. Nicholson, D.W., et al., *Identification and inhibition of the ICE/CED-3 protease necessary for mammalian apoptosis.* Nature, 1995. **376**(6535): p. 37-43.
136. Hambardzumyan, D., et al., *Genetic modeling of gliomas in mice: new tools to tackle old problems.* Glia, 2011. **59**(8): p. 1155-68.
137. Zhu, Y., et al., *CSF1/CSF1R blockade reprograms tumor-infiltrating macrophages and improves response to T-cell checkpoint immunotherapy in pancreatic cancer models.* Cancer Res, 2014. **74**(18): p. 5057-69.
138. De, I., et al., *CSF1 Overexpression Promotes High-Grade Glioma Formation without Impacting the Polarization Status of Glioma-Associated Microglia and Macrophages.* Cancer Res, 2016. **76**(9): p. 2552-60.
139. Uhlen, M., et al., *A pathology atlas of the human cancer transcriptome.* Science, 2017. **357**(6352).
140. Hudson, A.L., et al., *Glioblastoma Recurrence Correlates With Increased APE1 and Polarization Toward an Immuno-Suppressive Microenvironment.* Front Oncol, 2018. **8**: p. 314.

141. Barthel, F.P., et al., *Longitudinal molecular trajectories of diffuse glioma in adults.* Nature, 2019. **576**(7785): p. 112-120.
142. Quail, D.F., et al., *The tumor microenvironment underlies acquired resistance to CSF-1R inhibition in gliomas.* Science, 2016. **352**(6288): p. aad3018.
143. Zhao, J., et al., *Immune and genomic correlates of response to anti-PD-1 immunotherapy in glioblastoma.* Nat Med, 2019. **25**(3): p. 462-469.
144. Kobayashi, T., et al., *Prognostic significance of the immunohistochemical staining of cleaved caspase-3, an activated form of caspase-3, in gliomas.* Clin Cancer Res, 2007. **13**(13): p. 3868-74.
145. Shen, X., et al., *Glioma-induced inhibition of caspase-3 in microglia promotes a tumor-supportive phenotype.* Nat Immunol, 2016. **17**(11): p. 1282-1290.
146. Neubert, N.J., et al., *T cell-induced CSF1 promotes melanoma resistance to PD1 blockade.* Sci Transl Med, 2018. **10**(436).
147. Wu, A., et al., *Combination anti-CXCR4 and anti-PD-1 immunotherapy provides survival benefit in glioblastoma through immune cell modulation of tumor microenvironment.* J Neurooncol, 2019. **143**(2): p. 241-249.
148. Schonholzer, M.T., et al., *Real-time sensing of MAPK signaling in medulloblastoma cells reveals cellular evasion mechanism counteracting dasatinib blockade of ERK activation during invasion.* Neoplasia, 2020. **22**(10): p. 470-483.
149. Yan, D., et al., *Inhibition of colony stimulating factor-1 receptor abrogates microenvironment-mediated therapeutic resistance in gliomas.* Oncogene, 2017. **36**(43): p. 6049-6058.
150. Martinez-Lage, M., et al., *Immune landscapes associated with different glioblastoma molecular subtypes.* Acta Neuropathol Commun, 2019. **7**(1): p. 203.
151. Shih, A.H. and E.C. Holland, *Platelet-derived growth factor (PDGF) and glial tumorigenesis.* Cancer Lett, 2006. **232**(2): p. 139-47.
152. Pudelko, L., et al., *An orthotopic glioblastoma animal model suitable for high-throughput screenings.* Neuro Oncol, 2018. **20**(11): p. 1475-1484.
153. Ladomersky, E., et al., *IDO1 Inhibition Synergizes with Radiation and PD-1 Blockade to Durably Increase Survival Against Advanced Glioblastoma.* Clin Cancer Res, 2018. **24**(11): p. 2559-2573.
154. Haanen, J., et al., *Management of toxicities from immunotherapy: ESMO Clinical Practice Guidelines for diagnosis, treatment and follow-up.* Ann Oncol, 2017. **28**(suppl_4): p. iv119-iv142.
155. D'Angelo, S.P., et al., *Efficacy and Safety of Nivolumab Alone or in Combination With Ipilimumab in Patients With Mucosal Melanoma: A Pooled Analysis.* Journal of clinical oncology : official journal of the American Society of Clinical Oncology, 2017. **35**(2): p. 226-235.
156. Konno, T., et al., *Diagnostic criteria for adult-onset leukoencephalopathy with axonal spheroids and pigmented glia due to CSF1R mutation.* Eur J Neurol, 2018. **25**(1): p. 142-147.

7 Declaration of personal contribution

The work was supervised by Prof. Dr. med. Dr. rer. nat. Ghazaleh Tabatabai, Department of Neurology & Neuro-Oncology at the Hertie Institute for Clinical Brain Research in the research group “Laboratory for Clinical and Experimental Neurooncology”.

The entire study was designed by Prof. Dr. med. Dr. rer. nat. Ghazaleh Tabatabai, the animal experiments were designed by Dr. Susanne Beck and Dr. Justyna Przystal.

All clinical data from the patient cohort of chapter 3.1 were collected from the electronic database of the University Hospital Tübingen by Dr. med. Marilin Koch, Nataliya Korinetska und Hulda Ewald.
Construction of the Tissue microarray (TMA) (Methodology 2.2.2.) has been performed by the candidate with the support of Prof. Dr. med. Jens Schittenhelm (Department of Neuropathology).
Automated CSF1R staining of human tissue samples (as described in 2.2.2.2 and 3.1) was performed in the department of neuropathology and performed by their medical technicians.
Formal analysis, investigation and data curation of chapter 3.1 have been performed by the candidate with the support of Prof. Dr. med. Jens Schittenhelm (Department of Neuropathology).

The *in vivo* experiment described in 3.2.1 (Methodology 2.2.4.) was performed by Dr. Justyna Przystal and Denis Canjuga. The immunohistochemical analysis of post-treatment tissues as described in 3.2.2, 3.3.2 and 3.3.4 (Methodology 2.2.8-9) were performed by the candidate upon training of Heike Pfrommer and Dr. Justyna Przystal.

In vivo experiments of sections 3.3.1., 3.3.2 and 3.3.5 were performed by the candidate and supported by Dr. Justyna Przystal, Denis Canjuga and Bianca Walter.
The MRI sequences described in. 2.2.7. were designed by the scientific collaborators of the translational neuroimaging group of the Werner Siemens Imaging Center Dr. Salvador Castaneda Vega and Kristin Patzwald. Data

acquisition of the MRI and PET scans as shown in 3.3.3 were performed by the candidate together with Dr. Justyna Przystal, Dr. Salvador Castaneda Vega and Kristin Patzwald. The MRI volumetry data shown in 3.3.3 were acquired by the candidate upon training by Kristin Patzwald and Dr. Salvador Castaneda.
Formal analysis of 3.3.1, 3.3.2, 3.3.4 and 3.3.5 and visualisation were executed by the candidate.
Data curation and formal analysis of chapter 3.4 were performed by the candidate after training and support by Dr. Justyna Przystal and Denis Canjuga.

All shown graphs, figures and tables were prepared independently by the candidate.

The statistical and methodological analysis were performed by the candidate.

I assure that I have written the thesis independently under the supervision of Prof. Dr. med. Dr. rer. nat. Ghazaleh Tabatabai and Dr. rer. nat. Susanne Beck and I have not used any sources other than those indicated by me.

Tübingen,

[Signature candidate]

8 Publications

Parts of this MD thesis were published in the following publication:

Przystal, J.M.*; Becker, H.*; Canjuga, D.; Tsiami, F.; Anderle, N.;Keller, A.-L.; Pohl, A.; Ries, C.H.;Schmittnaegel, M.; Korinetska, N.; ; Koch, M.; Schittenhelm, J.; Tatagiba, M.; Schmees, C.; Beck, S.C.; Tabatabai, G. Targeting CSF1R Alone or in Combination with PD1 in Experimental Glioma. *Cancers* **2021**,*13*, 2400. https://doi.org/10.3390/cancers13102400

* contributed equally to this work

Data already published in the above-mentioned publication has been cited accordingly.

9 Acknowledgement

At this point I would like to thank Dr. Justyna Przystal for her excellent introduction to the methodology, her scientific enthusiasm, her advice and loyal support.

Furthermore, I would like to thank Heike Pfrommer and Sarah Hendel for their excellent technical assistance, as well as all the other lab members for the good cooperation.

I would like to thank Kristin Patzwald, Prof. Dr. med. Jens Schittenhelm and Dr. Salvador Castaneda Vega for the trustful scientific cooperation and the lively scientific exchange.

I would like to thank Dr. rer. nat. Susanne Beck for her valuable helpful corrections of the manuscript.

I thank particularly Stephanie Klein, Martin Schippert, Anne Griesshammer and Bianca Walter for the extremely pleasant atmosphere inside the laboratory, the friendship that developed, the many fruitful, scientific discussions and the tireless corrections within the writing process.

I would especially like to thank my doctoral supervisor Prof. Dr. med. Dr. rer. nat. Ghazaleh Tabatabai for the dedicated supervision, professional help, great trust and scientific support within the process of the doctoral thesis.

I would also like to thank Georg Schweizer for the endless and fruitful statistical and scientific discussions. Moreover, I thank my girlfriend, Karola Schiele for the faithful support during the 2017/2018 lab period and during the writing process.

Lastly, I would like to thank my parents and my uncle who paved my academic path, supported me tirelessly, and faithfully accompanied me along my journey.